

TRANSPARENT LUMINESCENT SOLAR CONCENTRATORS

By

Yimu Zhao

A THESIS

Submitted to  
Michigan State University  
in partial fulfillment of the requirements  
for the degree of

Chemical Engineering- Doctor of Philosophy

2015

## ABSTRACT

### TRANSPARENT LUMINESCENT SOLAR CONCENTRATORS

By

Yimu Zhao

Integrating solar-harvesting systems into the built environment is a transformative route to capturing large areas of solar energy, lowering effective solar cell installation costs, and improving building efficiency. Indeed, the idea of luminescent solar concentrators (LSC), which were first introduced in the 1970s to reduce solar cell costs, are now regaining attention as low-cost solar harvesting systems to deploy around the building envelope. However, the visible absorption and emission of these LSCs result in highly colored systems that hamper their widespread adoptability in many applications, including windows. Here, we introduce the concept of transparent luminescent solar concentrators (TLSC) that can selectively harvest ultraviolet (UV) and near-infrared (NIR) without impacting visible light, and which create an entirely new paradigm for power-producing transparent surfaces that can be deployed in windows, displays, and beyond. In the first configuration, we have designed systems composed of novel metal halide phosphorescent luminophore blends; these nanoclusters enable selective harvesting of UV photons with absorption cutoff positioned at the edge of visible spectrum (430nm) and massive-downconverted emission in the near-infrared (800nm) with very high quantum yields for luminescence. In the second configuration, we have developed transparent luminescent solar concentrators employing fluorescent organic salts with both efficient NIR absorption and emission. We describe the photophysical properties and

electronic performance of both classes of devices, the impact of ligand-host control, and architecture optimization. These TLSCs present new opportunities for clear solar-harvesting surfaces and windows that can translate into improved building energy efficiency, autonomous mobile electronics, and lower cost solar harvesting systems.

## ACKNOWLEDGEMENTS

First and foremost I would like to thank my advisor, Dr. Richard Lunt. I cannot express my appreciation for your guidance, encouragement and support. You have witnessed and guided my growth over the course of this thesis. I could not have asked for a more perfect advisor. I also am appreciative to my thesis committee members Dr. Pengpeng Zhang, Dr. Ilsoon Lee, and Dr. Scott Barton for taking the time to contribute to this work.

I owe thanks to the MOE members who filled my PhD life with wonderful memories. Chris, you helped me in so many ways, in research, and in adapting to US life. I am convinced that you have a great sense of humor, even though I sometimes miss the punchline. Peggy, our group is more like a big family because of your devotion. Also, I owe thanks to Paddy, Pei, Yunhua, Dhanashree, Lily, Kevin, John, Brian, Juan, Lucas, Tyler, Jorge. I wish everyone great success and the best of luck in the future.

Also, I am thankful to my collaborators, Dr. Baker, Dr. Levine, Dr. Hogan, and their students. I am also thankful to Brian Rook in the Composite Materials & Structures Center, who helped me many times. I am especially grateful to my great friends at MSU: Hao, Xinting, Yan, Peng, Yang, Yi, Miao, Catlin, Dena, Oishi, Chetan, Jing, Saisi, Anna. I will never forget all the fun we have had – all the picnics, camping, festival celebrations, cards, and I will never forget how we made it through these four years.

I am eternally indebted to my parents. Your persistent encouragement, support and confidence in me always keeps me going, no matter when you are in the US or China, no matter when things go up or down. I am proud to be your pride always.

Finally, I would like to thank Mr. G. Chen. Because of you, I have a deeper love for this world.

## TABLE OF CONTENTS

LIST OF TABLES.....	viii
LIST OF FIGURES.....	ix
<b>Chapter 1 Introduction to Organic and Excitonic Semiconductors.....</b>	<b>1</b>
1.1 Organic and excitonic materials.....	1
1.2 Organic and excitonic photovoltaics.....	3
1.3 Luminescent materials.....	6
1.3.1 Organic dyes.....	11
1.3.2 Nanoclusters and quantum dots.....	12
1.3.3 Rare earth ions.....	14
<b>Chapter 2 Introduction to Luminescent Solar Concentrators.....</b>	<b>16</b>
2.1 Overview of luminescent solar concentrators.....	16
2.2 Luminophores.....	20
2.3 Waveguide and hosts.....	20
2.4 Overall LSC efficiency.....	23
2.4.1 Solar spectrum absorption efficiency.....	24
2.4.2 Solar cell efficiency.....	24
2.4.3 Reabsorption efficiency.....	26
<b>Chapter 3 Transparent photovoltaics.....</b>	<b>28</b>
3.1 Transparent solar cells.....	28
3.2 Transparent Luminescent solar concentrator for solar windows.....	29
3.3 Theoretical and practical limits of transparent luminescent solar concentrators.....	33
<b>Chapter 4 Experimental Techniques.....</b>	<b>37</b>
4.1 Photoluminescent emission and excitation testing.....	37
4.2 Quantum yield measurement.....	39
4.3 Optical absorption, reflection and transmission.....	42
4.4 Electrical, J-V and EQE measurements.....	45
4.5 LSC simulations.....	48
<b>Chapter 5 UV-absorbing Transparent Luminescent Solar Concentrators... ..</b>	<b>52</b>
5.1 Introduction.....	52
5.2 Experimental Section.....	53
5.2.1 Nanocrystal cluster preparation.....	53

5.2.2 Module fabrication: .....	54
5.3 Results.....	55
5.4 Discussion.....	63
5.4.1 Nanocluster photophysics.....	63
5.4.2 LSC design.....	65
5.4.3 Understanding blend configuration via XPS.....	66
5.5 Conclusion.....	66
<b>Chapter 6 NIR-absorbing Transparent Luminescent Solar Concentrator.....</b>	<b>68</b>
6.1 Introduction.....	68
6.2 Experimental Section .....	69
6.2.1 Organic salt solution preparation: .....	69
6.2.2 Module fabrication: .....	70
6.2.3 Electronic Structure Calculations: .....	70
6.3 Results.....	71
6.4 Discussion.....	78
6.4.1 Luminophore photophysics.....	78
6.4.2 LSC design.....	79
6.4.3 TLSC lifetime measurement.....	83
6.5 Demo .....	85
6.6 Flexible transparent LSCs.....	86
6.7 Conclusion.....	89
<b>Chapter 7 Transparent Luminescent Solar Concentrators Cost.....</b>	<b>90</b>
7.1 TLSC Manufacturing cost.....	92
7.2 Module cost.....	93
<b>Chapter 8 Conclusions and Future Outlooks.....</b>	<b>96</b>
8.1 Future outlook.....	96
8.1.1 Singlet Fission Hosts for UV TLSCs.....	96
8.1.2 Molecular design for NIR TLSCs.....	98
8.1.3 Micro LSC Arrays for NIR TLSCs:.....	100
8.1.4 Transparent mirror design for photon management in TLSCs.....	101
APPENDIX.....	103
BIBLIOGRAPHY.....	107

## LIST OF TABLES

<b>Table 1.1</b> Luminescence categories based on energy source .....	7
<b>Table 1.2</b> Absorption, emission and quantum yield for common chromophores.....	11
<b>Table 1.3</b> Absorption, emission and quantum yield for common QDs.....	14
<b>Table 2.1</b> Efficiency of highest performance of LSC .....	19
<b>Table 2.2</b> Refractive index for common materials.....	22
<b>Table 7.1</b> Estimated manufacturing and materials cost.....	93
<b>Table A1</b> Quantum yield and absorption of organic luminescent materials in solutions.....	104
<b>Table A2</b> Quantum yield and absorption for luminescent materials in films.....	106

## LIST OF FIGURES

**Figure 1.1** Structural diagram of several organic compounds, (top from left to right) di-indenoperylene (DIP), carbon nanotube,  $C_{60}$ , (bottom from left to right) ClAlPc, naphthalene through pentacene, Ru-complex .....2

**Figure 1.2** Schematic illustration of a bilayer heterojunctions at open circuit voltage. Excitons are created and diffuse to the donor/ acceptor interface where the excitons are dissociated. The charge carriers are then transported to the electrodes to generate power. The work functions for cathode and anode are  $\Phi_C$  and  $\Phi_A$ , respectively.....4

**Figure 1.3** Current density ( $J$ ) –voltage ( $V$ ) characteristics of a GaAs solar cell. The red point is the operating point. The FF is defined by the ratio of  $A_1/A_2$  where  $A_1$  is maximized along the  $J$ - $V$  curve.....5

**Figure 1.4** Simplified schematic of spins in the ground and excited states .....8

**Figure 1.5** Jablonski diagram outlining the excitation and emission processes for an organic or excitonic molecule 1) excitation to the first excited state; 2) excitation to a higher excited state; 3) and 4) vibrational relaxation; 5) non-radiative decay to the ground state; 6) fluorescent emission; 7) intersystem crossing; and 8) phosphorescent emission..8

**Figure 1.6** Normalized absorption and emission spectra for a fluorescent emitter (up) and phosphorescent emitter (bottom). The difference between the absorption and emission peak is Stokes shift. In the case of the phosphorescent emitter the Stokes shift is alternatively referred to as the down-conversion shift.....10

**Figure 2.1** Photograph of focusing-optics concentrators<sup>[56]</sup> a) parabolic troughs b) heliostatic arrays c) sterling dishes, and d) Fresnel reflectors .....17

**Figure 2.2** Schematic of a luminescent solar concentrator composed of luminescent dyes, waveguide, and attached PVs. PVs are typically mounted around every edge, but have been omitted from the front and back for schematic clarity. The component efficiencies shown in the configuration are 1) solar spectrum absorption efficiency 2) luminophore photoluminescence efficiency (quantum yield efficiency) 3) waveguide efficiency 4) re-absorption efficiency 5) solar cell quantum efficiency.....18

**Figure 2.3** Photograph of typical colorful luminescent solar concentrators highlighting the waveguided emission that is brightly focused at the edge. (b) Example of a traditional LSC in front a window, highlighting the difficulty in installing these systems in a variety of applications such as windows. ....19

**Figure 2.4** Absorption coefficients of standard glass, quartz, BF33 glass, low iron glass, polycarbonate (PC) and poly(methyl methacrylate) (PMMA) <sup>[71]</sup> as a function of wavelength.....23

**Figure 2.5** Photos of cut Si cell (left) and GaAs cell (right) for attaching to the edge of the LSC waveguide.....25

**Figure 2.6** Plot of the AM1.5G Solar Cell Efficiency as a function of bandgap (black), and efficiency normalized by the AM1.5 absorption efficiency (gold). Highest reported efficiencies are highlighted in red squares. ....26

**Figure 3.1** Overlap of the AM1.5G solar flux and the photonic response of the eye shows that about 1/3 of the photon flux is in the visible part of the spectrum with the remaining 2/3 of the flux in the NIR.....30

**Figure 3.2** Diagram of the point of installation for building glasses with transparent luminescent solar concentrators .....33

**Figure 3.3** Transparent PV theoretical efficiency limits as a function of bandgap and level of visible transparency (VT). Note that these limits are the same for transparent LSCs with ideal absorption/emission profiles with no spectral overlap.....33

**Figure 3.4** Representative absorption and emission characteristics of TLSC emitters. The Stokes shift ( $S$ ) and emission width ( $W$ ), two key emitter parameters, are highlighted. ....34

**Figure 3.5** TLSC practical efficiency limits with no ideal absorption/emission profiles with no spectral overlap as a function of the a) emission width ( $W$ ) with  $S = 0$  or b) Stokes shift ( $S$ ) with  $W = 0$ . Note that the decrease in efficiency stems from a lower theoretical voltage and FF from the PV cell mounted around the edge. However, the situation in b) has a distinct advantage in practice since it will suppress reabsorption losses in non-ideal absorption emission overlap configurations. That is, narrow emitters will always provide greater flexibility for larger Stokes shifts and minimized reabsorption losses. ....35

<b>Figure 4.1</b> Schematic of spectrofluorometer system.....	38
<b>Figure 4.2</b> Images of the solid film (left) and solution (right) sample holder for photoluminescent excitation and emission measurements. Red glow from a chromophore solution can be seen with green excitation at 550 nm. ....	39
<b>Figure 4.3</b> Photo of an integrating sphere for quantum yield measurement .....	41
<b>Figure 4.4</b> Quantum yield data for a 9,10-Diphenylanthracene (DPA) film. DPA is dissolved in toluene and spin-coated as film. The background glass sample (blue) and DPA film sample (red) spectra are plotted. (inset) The emission peaks for the two films. ....	42
<b>Figure 4.5</b> Schematic of processes of absorption, reflection, scattering, and transmission which occur when incident light passes through a sample with a thickness of $L$ (left); Visualization of the transmission, absorption and reflection from a rhodamine solution illuminated with a green laser (right) – note that the exponential absorption profile can be seen in the solution as. ....	43
<b>Figure 4.6</b> Photos of transmission measurement of liquid sample in cuvette (left) and film samples on glass (right).....	45
<b>Figure 4.7</b> Configuration of $JV$ testing for a TLSC system. An additional mask is used to block the edge of the cells from direction illumination. ....	46
<b>Figure 4.8</b> Photo of EQE measurement a) monowavelength signal illuminating on the surface or the test sample b) the test fixture connected to the Keithley picoameter for current readings and c) the Keithley sourcemeter and channel switcher for testing multiple devices. ....	47
<b>Figure 4.9</b> Correction for EQE measurement at distance of $d$ to the edge when one PV cell is attached. $L$ is the plate width and $g$ is geometric factor. The measured EQE is corrected by the geometric factor. ....	48
<b>Figure 5.1</b> Quantum yield of core material MH ( $\text{Mo}_6\text{Cl}_{12}$ ) with different cations (K, $\text{H}_2\text{O}$ , TBA) in solvents acetone (ACE) or acetonitrile (ACN).....	54

**Figure 5.2** (a) Schematic of the transparent luminescent solar concentrator and (b)  $M_6X_{12} \cdot L_2$  nanocluster-blend structure (dark green atom = M, light green atom = X); note that the salt compounds can be represented in (b) by replacing L with A-X or L-A-X....55

**Figure 5.3** (a) Normalized absorption (solid blue line) and emission (dotted red line) spectra of the UV absorbing luminophores overlaid with the measured EQE of the edge-mounted Si PVs (grey line). (b) Photograph of the LSC system incorporating the massive-Stokes shift UV nanoclusters under intense UV illumination where only the tail-end of red NIR emission can barely be seen except around the edge. Note that some blue/violet light can be seen through the LSC that originates from tail lamp emission in the range of 410-450nm. (inset) Comparison of the transparent luminescent concentrator (“TLSC“, left) with a typical semi-transparent solar concentrator (“LSC“, right) highlighting the need for both absorption and emission outside the visible spectrum.....56

**Figure 5.4** Measured quantum yield (QY) of  $K_2Mo_6Cl_{14}$  and  $(TBA)_2Mo_6Cl_{14}$  in acetonitrile as a function of concentration; solid lines are fits to Equation. 1. (inset) QY of the TBA film as a function of time under shelf-life conditions.....58

**Figure 5.5** External quantum efficiency (EQE) of the LSC system as a function of wavelength; (inset) measured EQE at 325nm as a function of geometric gain.....59

**Figure 5.6** Current density as a function of voltage for the fully assembled LSC systems with two of the luminophores. ....60

**Figure 5.7** Light intensity dependence of the  $V_{oc}$ ,  $FF$  and power efficiency of the Si cell .....61

**Figure 5.8** Calculation of the overall LSC system efficiency as a function of plate size and luminophore concentration, without (solid lines) and with (dotted lines) the intensity dependence of the Si PV. Note that the solid lines are calculated using the 1-sun Si PV parameters and that the plate length of 0.2m roughly translates to a luminescence equivalent intensity of 1sun around the edges. The system efficiency is impacted by the luminophore concentration accounting for the solar absorption efficiency, reabsorption loss, and the quantum yield. Improving the quantum yield to 100% would result in a peak system efficiency of up to 1.3-1.5%. ....62

**Figure 5.9** Comparison of transparent UV-absorbing luminescent solar concentrators with traditional color LSCs.....63

<b>Figure 6.1</b> (a) Schematic of the transparent luminescent solar concentrator (b) Photograph of the transparent LSC system incorporating CY luminophore in front of a picture of beach scenery.....	72
<b>Figure 6.2</b> CY and HITC molecular cation structures (top); the natural excited-state transition orbital pairs for HITC (left) and CY (right). The hole orbitals are shown on the top of the excited electron orbitals.....	73
<b>Figure 6.3</b> (a) Normalized absorption (circle symbols) and emission (square symbols) spectra of the NIR-absorbing luminophores CY (blue line) and HITCI (black line) films. (b) Measured quantum yield (QY) and absorption of CY (blue line) and HITCI (black line) solutions in dichloromethane as a function of concentration; solid lines are fits to model for the QY <sup>[72]</sup> and the Beer-Lambert law for the absorption.....	74
<b>Figure 6.4</b> (a) Light intensity dependence of the <i>V<sub>oc</sub></i> , <i>FF</i> , power efficiency and responsivity of the CY TLSC device. (b) Current density as a function of voltage for the fully assembled TLSC systems with two of the luminophores.....	75
<b>Figure 6.5</b> (a) External quantum efficiency (EQE) of the CY TLSC system as a function of wavelength measured from 0.02m to 0.07m, with 1cm increments. (b) Calculated EQE as a function of CY LSC length in the range of 0.02m to 0.08m. Measured EQE (circle symbols) are also shown here. (inset) Calculated and measured EQE as a function of CY LSC length over a larger plate range.....	76
<b>Figure 6.6</b> Calculation of the CY TLSC optical efficiency as a function of LSC length with a function of simulated Stokes shift. Stokes shift are 10nm (black, triangle), 20nm (black, square), 30nm (black, sphere), 50nm (gray, triangle), 80nm (gray, square), 130nm (gray, sphere). For reference, CY and HITCI have Stokes shifts of 20nm, and 30nm, respectively.....	77
<b>Figure 6.7</b> Lifetime test: absorption of CY7 acid films under different conditions as a function of time. Film 1 is CY7 acid PMMA film and Film 2 is CY7 acid fluoroshield film. ‘AO’ refers to the addition of an antioxidant DACBO (1,4-Diazabicyclo[2.2.2]octane) .....	84
<b>Figure 6.8</b> Lifetime test: quantum yield of CY7 acid film under different conditions as a function of time. Films are same as shown in figure 6.7.....	85
<b>Figure 6.9</b> Photograph of a NIR-absorbing TLSC demo. ....	86

**Figure 6.10** Flexible transparent luminescent solar concentrators on flexible plastic substrates. ....87

**Figure 6.11** (a) Performance metrics ( $V_{oc}$ ,  $FF$ , efficiency and responsivity) of the TLSC system as a function of illumination intensity. (b)  $J$ - $V$  curve of the sample at different incident intensities. (c)  $EQE$  as a function of wavelength measured at distance of 5, 10, 15, 20, 25 mm from the GaAs cell. (d) Transmission of the overall system. ....88

**Figure 7.1** Overall calculated LSC system efficiency for the UV only concentrator utilizing the spectral properties of Fig. 4, Si PVs, low-iron substrate with index 1.7, and quantum yields of a) 40% and b) 80% as a function of luminophore concentration embedded in a 5 mm thin host. Due to the massive Stoke shifts, the LSC performance remains high even for sheets as large as 10ft.....91

**Figure 7.2** Overall calculated LSC system efficiency for a) the NIR-only concentrator, and b) combined with spatially segmented 50 $\mu$ m Si solar cells utilizing the spectral properties, low-iron substrate with index 1.7, and quantum yields of a) 40% and b) 80% as a function of luminophore concentration embedded in a 50 $\mu$ m thin host. Note that with the transparent NIR luminophore embedded in the segmented PVs, the overall system efficiency can be more than triple that of the segmented PVs alone (grey line) for the same level of transparency and only utilizing a sliver of the NIR (675-800nm).....91

**Figure 7.3** Projection for the module cost in \$/WP of fabricating transparent LSCs on window surfaces a), b) for the UV luminophore and c), d) for the NIR CY luminophore using their respective spectral properties. Estimates are for a substrate index of  $n = 1.7$ , a commercially-available Si PV module efficiency of 18% under AM1.5G, and quantum yields of a), c) 0.4 and b, d) 0.8 and modest Stokes shift < 50nm.....95

**Figure 8.1** Vertical excitation energies of the lowest singlet ( $S_1$ ) and triplet ( $T_1$ ) excited states of three candidates for singlet fission. (b) Schematic of the singlet fission-energy transfer process .....97

**Figure 8.2** IR 780 in dimethylformamide (DMF) reacted with 1,4 benzenedithiol .....99

**Figure 8.3** Examples of candidates for molecular design for NIR TLSCs .....99

**Figure 8.4** New chemical variants with shifted absorption spectrum and modified Stokes shifts after reaction for 10min.....100

**Figure 8.5** (left) Measured and simulated reflection curves for two *transparent mirrors* designed to accept short-wave NIR and trap longer-wave NIR emission (shown schematically, middle). (right) Schematic for the ideal mirror configuration for the NIR and UV LSCs used to eliminate waveguiding losses..... 102

## Chapter 1

### Introduction to Organic and Excitonic Semiconductors

The goal of this chapter is to introduce readers to the field of organic and excitonic semiconductors. The underlying principles of the basic properties of organic and excitonic materials and solar cells will be discussed. Then the photophysics and categories of luminescent materials will be introduced.

#### 1.1 Organic and excitonic materials

Organic materials generally refer to compounds composed of carbon and hydrogen. (examples are shown in Figure 1.1). While many carbon-containing compounds, such as  $C_{60}$ , carbon nanotubes, simple carbon oxides, are not strictly organic molecules because they lack C-H bonds, they nonetheless act like organic small molecules. Organic compounds consist of both intramolecular covalent bonding and intermolecular molecular bonding. An important subsection of molecular compounds, not limited to organic compounds, is called conjugated small molecule compounds. The highly conjugated  $\pi$ - $\pi$  electron system enables the molecules to have desirable electronic excitonic properties. The delocalization of the  $\pi$ - $\pi$  electron systems result in electronic excitation energies in the range of several eV, which is of great interest when considered for applications in semiconductors, solar cells, and light generation.

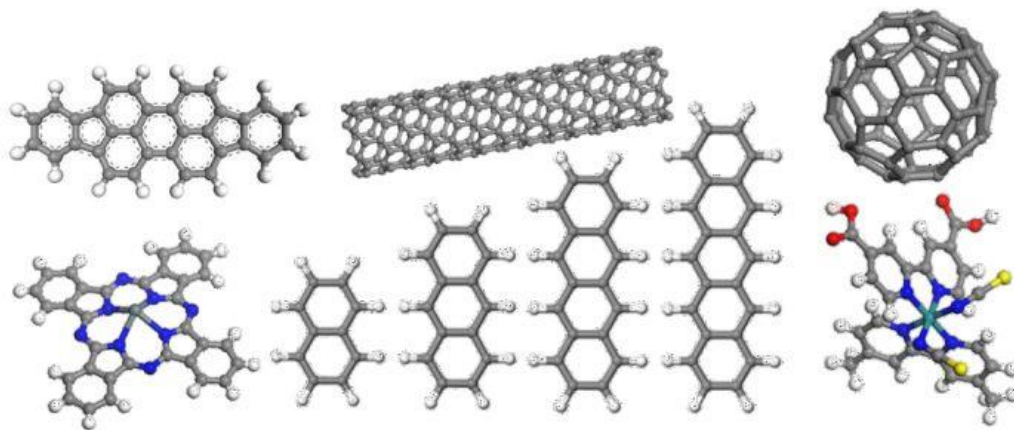


**Figure 1.1** Structural diagram of several organic compounds, (top from left to right) diindenoperylene (DIP), carbon nanotube, C<sub>60</sub>, (bottom from left to right) ClAlPc, naphthalene through pentacene, Ru-complex

These  $\pi$  electrons, which are delocalized above and below the atom planes, create “localized cloud of electrons”, and impart many of the optical and electrical semiconductor characteristics. Organic materials have nearly infinite tunability of the optical/electrical properties by functional group and chemical substitution. The existence of excitonic states is one of the most defining characteristic of conjugated molecule compounds. An exciton is defined as a bond state of an electron and a hole which are attracted to each other by the electrostatic Coulomb force. The radius of an exciton is defined as the average distance between the electron and the bound hole.

In addition, a lack of necessity for lattice-matching characteristic of inorganic film growth enables greater convenience and low cost processability. Low temperature and large area deposition on light-weight flexible substrates such as metal foils, paper, and plastics have recently been realized making these materials excellent candidates for a range of low cost electronics.<sup>[1-4]</sup> Organic and excitonic semiconductors have already been deployed in a variety of applications such as transistors, sensors, solar cells, organic light emitting diodes (OLEDs), lasers, and circuits.

## 1.2 Organic and excitonic photovoltaics

Solar energy has gained tremendous attention in the past few decades as solar energy has been shown to be one of a few alternative energy sources capable of offsetting the current worldwide energy consumption. Solar cells convert various wavelengths of absorbed photon flux to electrical power.

The first practical photovoltaic device was demonstrated in the 1950s. From the 1980s, research on silicon solar cells increased the efficiency of photovoltaics substantially. In 1985, silicon photovoltaics reached a milestone efficiency of 20%. Over the next decade, the efficiency continued increasing promoted by the power supply market and now sits around 25% at the lab scale and 17% in commercially available modules. <sup>[5]</sup>

In contrast, the first efficient organic solar cell above 1% was demonstrated by Tang in the 1980s.<sup>[6]</sup> An efficient organic solar cell incorporates a bilayer structure composed of a donor layer and an acceptor layer shown in Figure 1.2. The working principle of an organic and excitonic cell is as follows. An incident photon is absorbed by either the donor layer or the acceptor layer and a tightly bound exciton is produced. The potential difference between contact layers provides a weak driving force to separate the exciton. If a heterojunction with adequate energy level offset is introduced, it can then enhance the driving force to dissociate exciton that diffuse to the heterojunction interface. If the exciton dissociates before it recombines, free carries (electrons and holes) are produced and move to electrodes where they are collected to generate current.

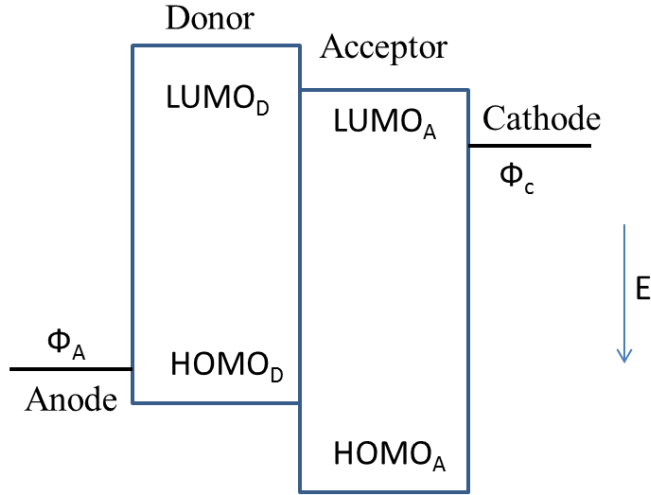


**Figure 1.2** Schematic illustration of a bilayer heterojunctions at open circuit voltage. Excitons are created and diffuse to the donor/ acceptor interface where the excitons are dissociated. The charge carriers are then transported to the electrodes to generate power. The work functions for cathode and anode are  $\Phi_C$  and  $\Phi_A$ , respectively.

The quantum conversion efficiency, defined as the ratio between the number of generated electrons to number of incident photons, is composed of the constituent mechanisms as:

$$\eta_{EQE} = \eta_A \eta_{ED} \eta_{CT} \eta_{DS} \eta_{CC} \quad (1.1)$$

Here,  $\eta_{EQE}$  is the quantum conversion efficiency,  $\eta_A$  is the absorption efficiency,  $\eta_{ED}$  is the exciton diffusion efficiency,  $\eta_{CT}$  is the charge-transfer efficiency at the interface,  $\eta_{DS}$  is the charge dissociation efficiency (i.e. dissociation prior to geminate recombination)

$\eta_{CC}$  is the charge collection efficiency (i.e. collection prior to bimolecular recombination).

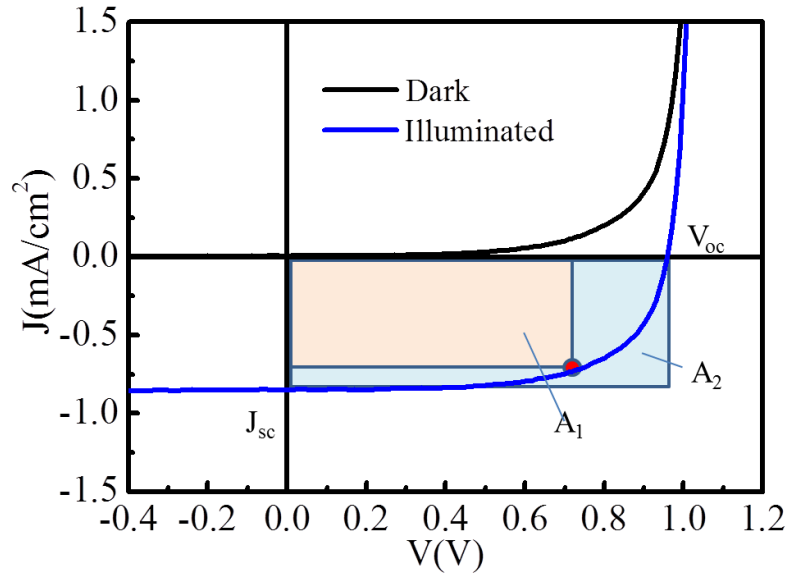


**Figure 1.3** Current density ( $J$ ) –voltage ( $V$ ) characteristics of a GaAs solar cell. The red point is the operating point. The FF is defined by the ratio of  $A_1/A_2$  where  $A_1$  is maximized along the  $J$ - $V$  curve.

The curve showing the relationship between current density through an electronic device and voltage across the terminal is called current density ( $J$ ) – voltage ( $V$ ) curve, which is key in the defining the output power generation of a solar cell. It is the superposition of a diode in the dark with the light-generated current density. The light shifts the  $J$ - $V$  curve down into the fourth quadrant where output power is extracted from the diode. Figure 1.3 shows a typical  $J$ - $V$  curve for a solar cell. The energy conversion efficiency for a solar cell is defined as the fraction of output electricity to the incident power, which can be calculated with Equation 1.2

$$P = \frac{V_{oc} J_{sc} FF}{P_0} \quad (1.2)$$

where  $P_0$  is the input power,  $V_{oc}$  is the open circuit voltage,  $J_{sc}$  is the short circuit current, and  $FF$  is the fill factor. Here,  $FF$  is defined as:

$$FF(P_0) = \frac{V_{mp}(P_0) \cdot J_{mp}(P_0)}{V_{oc}(P_0) \cdot J_{sc}(P_0)} \quad (1.3)$$

$V_{mp}(P_0)$  and  $J_{mp}(P_0)$  are the voltage and current density where the output power is maximum. The relationship between short circuit current ( $J_{sc}$ ) and external quantum efficiency ( $EQE$ ) is

$$J_{sc} = q \int S(\lambda) \cdot EQE(\lambda) d\lambda \quad (1.4)$$

where  $S(\lambda)$  is the photon flux. The power efficiency of a solar cell is then proportional to the area under the  $JV$  curve in the fourth quadrant.

### 1.3 Luminescent materials

Excitonic materials by their nature are good photon emitters. The term luminescence describes those processes that involve the release of a photon from an excited molecule. Input energy from different physical and chemical energy sources result in a transition from the ground state to excited states. Table 1.1 shows various sources of energy and the corresponding luminescence terminology.

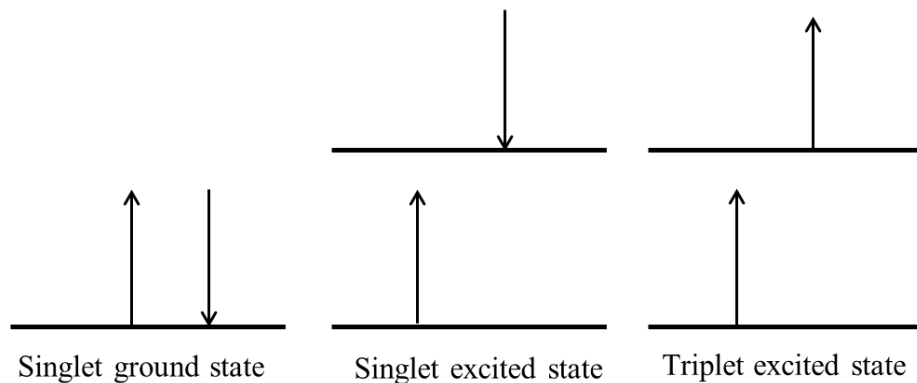
**Table 1.1** Luminescence categories defined based on energy source.

Source of energy	Luminescence terminology
Electrical	Electroluminescence, Galvanoluminescence
Chemical	Chemiluminescence, Bioluminescence, Electrochemiluminescence
Light	Photoluminescence, Fluorescence, Phosphorescence
Thermal	Thermoluminescence, Pyroluminescence
Mechanical	Triboluminescence, Mechanoluminescence,

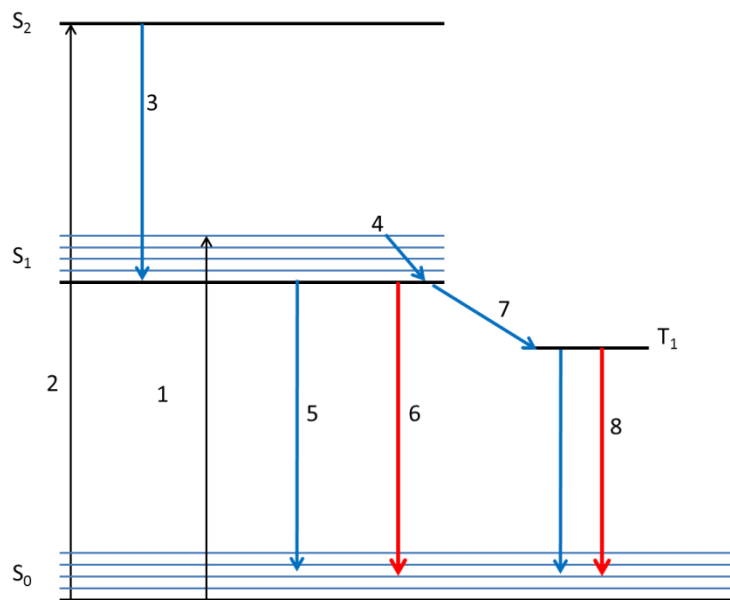
For species excited by absorbance of a photon, fluorescence and phosphorescence are the two forms of luminescence. In general, fluorescence is a fast emission process that occurs at the nanosecond time scale, while phosphorescence occurs at longer time scales from microseconds up to hours or even days. The differences between these two forms of luminescence, often tied to differences in spin states, will be discussed in greater detail throughout this thesis.

An electron can have a spin quantum number of  $1/2$  or  $-1/2$ . A singlet state is an excited state in which all electrons in the molecule are spin-paired (up and down), so the total spin for the system is  $S_s = 0$ . In contrast, triplet states have one set of electron spins which is unpaired, so  $S_s = 1$ . The spin-angular momentum vector  $L$  associated with these electrons and systems can be calculated as  $L=2 S_s + 1$ . For a singlet state,  $L=2(0)+1=1$  so only one singlet state exists. For a triplet state,  $L=2(1)+1=3$  so three triplet states exist. Figure 1.4 shows the simplified spin configuration for singlet and triplet states. Photons

released from excited singlet state result in fluorescence emission while photons from excited triplet state result in phosphorescence emission.



**Figure 1.4** Simplified schematic of spins in the ground and excited states



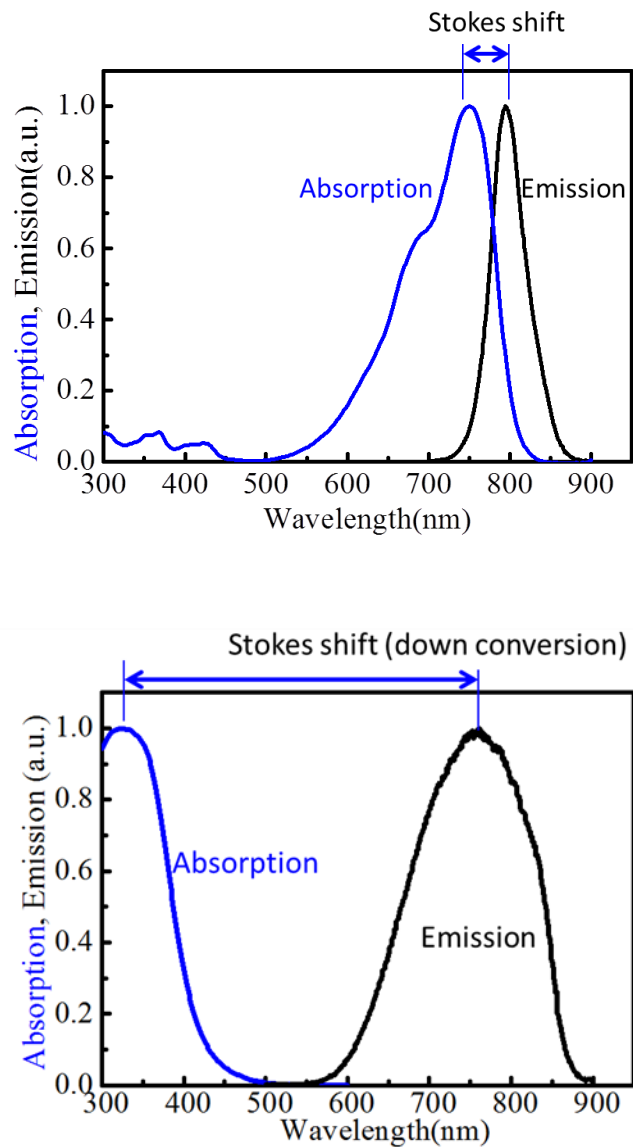
**Figure 1.5** Jablonski diagram outlining the excitation and emission processes for an organic or excitonic molecule 1) excitation to the first excited state; 2) excitation to a higher excited state; 3) and 4) vibrational relaxation; 5) non-radiative decay to the ground state; 6) fluorescent emission; 7) intersystem crossing; and 8) phosphorescent emission

Figure 1.5 diagrams the major processes that can occur during excitation and emission from an organic semiconductor. The ground state ( $S_0$ ) can be excited to a first electronic

excited state  $S_1$  with the absorption of a photon, or an even higher energy excited state  $S_2$  if the photon energy is large enough. In all cases, the excited state rapidly decays to lowest vibrational level of  $S_1$  through relaxation. This excited state may then further relax to ground state by nonradiative decay, releasing extra energy as heat or phonons or, alternatively, the excitation energy is re-emitted as a photon (fluorescence). In addition, an intersystem crossing process may occur that transfers the excited state from the  $S_1$  to the triplet,  $T_1$ . The  $T_1$  state can decay to the ground state  $S_0$  by emitting a photon (phosphorescence) or can relax to ground state by a non-radiative decay. Because the transitions between the singlet ground state and excited triplets states are spin-forbidden, phosphorescence is typically not observed. However, there are several mechanisms that can make this spin-forbidden process weakly allowed such as spin-orbit coupling and symmetry. Indeed, the discovery of efficiency phosphorescent emitters has played an important role in the commercial success of organic light emitting diodes.

Thus, the key characteristics that define these systems are the spectral distribution of the emission (the emission spectrum), the excitation (the excitation spectrum; or simply as absorption spectrum) and the ratio of the radiative and the nonradiative rates of return to the ground state (quantum yield efficiency). The difference between absorption and emission spectral maxima is defined as Stokes shift, and is another key parameter. The Stokes shift may vary from a few nanometers to hundreds of nanometers depending on the materials. Because triplet levels are (almost) always lower in energy than singlet energies due to the electron repulsion interactions from electron exchange, phosphorescent materials typically have substantially larger Stokes shift than fluorescent

materials. Figure 1.6 shows an example of absorption and fluorescent emission spectra and Stokes shift for a fluorescent and a phosphorescent emitter, respectively.



**Figure 1.6.** Normalized absorption and emission spectra for a fluorescent emitter (up) and phosphorescent emitter (bottom). The difference between the absorption and emission peak is Stokes shift. In the case of the phosphorescent emitter the Stokes shift is alternatively referred to as the down-conversion shift.

### 1.3.1 Organic dyes

Organic dyes of greatest interest are highly  $\pi$  conjugated molecules. By engineering the conjugation, the properties of the materials can be varied over a large spectral range. For example, increasing conjugation typically reduces the bandgap of organic molecules.

Organic dyes have been studied as luminophores because of their high quantum yield that stems from their excitonic nature, good solubility, and absorption efficiency. Several representative dyes investigated previously for LSCs include: bipyridines,<sup>[7]</sup> naphthalimides,<sup>[8-10]</sup> dicarbocyanine iodide,<sup>[11]</sup> dicyanomethylenes,<sup>[11-14]</sup> coumarins<sup>[15-17]</sup> and perylenebisimides,<sup>[8-10, 15, 18-21]</sup> rhodamines,<sup>[8, 11, 13, 22, 23]</sup> sulforhodamines,<sup>[11, 24]</sup> etc. Many properties of these common chromophores and luminophores are highlighted in Table 1.2. While the quantum yields of many visible chromophores are close to 1, the quantum yields of emitters in the infrared and near-infrared are typically much lower (<50%), representing an important materials challenge moving forward.

**Table 1.2** Absorption, emission and quantum yield for common visible chromophores.

Dye	Absorption $\lambda_{\max}$ (nm)	Emission $\lambda_{\max}$ (nm)	Quantum yield (%)	Reference
Rhodamine 6G	530	550	95	[23]
Rhodamine 101	563	588	96	[23]
Lumogen F Blue 650	377	411	>80	[15]
Lumogen F Red 305	578	613	98	[15]
Lumogen F Yellow 083	476	490	91	[15]

**Table 1.2 (cont'd)**

Lumogen F Orange 240	524	539	99	[15]
CRS040	440	506	98	[16]
PBI 4	520	580	96	[21]
F205	527	535	99	[25]
Perylene D3	577	674	70	[25]
DBT	570	670	12	[26]
DCJTb	472	505	44	[27]
NPD	350	445	29	[28]
Anthracene	350	410	29	[29]
Irppy <sub>3</sub>	300	512	97	[28, 30]
Alq <sub>3</sub>	260	520	20	[30]

### 1.3.2 Nanoclusters and quantum dots

Nanoscale materials exhibit optical and electric properties that differ significantly from their bulk counterparts. In terminology, nanoparticles, nanocrystals and quantum dots all refer to nanoscale crystalline ensembles of bulk semiconductors. In contrast, nanoclusters are an inorganic molecular species, exactly defined in chemical composition and structure at the nanometer scale, analogous to organic molecules without organic bonding.

Quantum confinement is a key characteristic of nanomaterials. In a more general form, a confined system is one where a particle surface defines the quantum potential well barrier. Quantum confinement effects arise when the particle size is comparable to the de Broglie wavelength of the confined particle. Consequently, nanomaterials have discrete

energy levels and exhibit a variety of optical and electrical properties which are tunable through particle size, surface structure, and elemental constituents.

Quantum dots are widely investigated as luminescent dyes in a variety of applications as sensors, lasers, and LEDs.<sup>[31-33]</sup> The sizes of the quantum dots determine optical behavior of the dot — both the absorption and emission spectra can be tuned as a result of size variations. Particle size of the dots can be manipulated by varying the reaction conditions,<sup>[34-36]</sup> but some size distribution is always present. As a result, the bandgap will decrease and the photoluminescence spectra are red-shifted.<sup>[37]</sup> There is a quantitative relationship between the red-shift and the spread of the quantum dot sizes, providing an additional strategy to minimize the re-absorption losses.<sup>[15]</sup> Another strategy that has recently emerged with QDs is the synthesis of core/shell structures that afford greater tunability and protection. The core/shell quantum dots also can allow for spectral separation that confines absorption and emission processes to different parts of the heterostructure resulting in large Stokes shift. The increase in the Stokes shift for the recently demonstrated core/shell QDs can help to reduce re-adsorption of photons, which greatly avoids the surface loss and increases the efficiency.<sup>[38, 39]</sup> However, QDs are quite sensitive to oxygen and light when they are kept outside a solid matrix.<sup>[35, 36]</sup> Many properties of common QDs are highlighted in Table 1.3.

**Table 1.3** Absorption, emission and quantum yield for QDs from the literature.

Dye	Absorption $\lambda_{\max}$ (nm)	Emission $\lambda_{\max}$ (nm)	Quantum yield (%)	Reference
CdSe	560	570	27	[40]
PbS	750	880	30	[41]
CdSe/CdS	<500	650	86	[38]
Mn <sup>+</sup> doped ZnSe/ZnS	400	600	37	[39]
CdSe/ZnTe	600	550-1000	30	[42, 43]
CdTe/CdSe	540	560	82	[44]
CdSe/ ZnS	480	488-560	50	[41]
Ag <sub>2</sub> S	785	1058	-	[45]
CuInS <sub>2</sub> / CdS	400-700	780	86	[46]
Cd <sub>x</sub> Cu <sub>1-x</sub> Se	400-620	800	27	[47]

### 1.3.3 Rare earth ions

Rare earth ions are a group of chemical elements in the periodic table, most notably the lanthanides as well as scandium and yttrium. Good photostability and large Stokes shift make rare earth ions candidate dyes for LSCs. However, absorption spectra are often notably discreet with sharp and narrow absorption peaks.

Neodymium (Nd<sup>3+</sup>) was the earliest rare earth ion<sup>[48]</sup> used in LSCs but the efficiency was low.<sup>[49]</sup> It exhibits sharp peak absorption around 580nm, but also absorbs at longer wavelengths. Emitted photons have wavelength of both 880nm and 1060nm. To increase the efficiency of neodymium-doped LSCs, ytterbium(Yb<sup>3+</sup>) is usually co-doped

with  $\text{Nd}^{3+}$ . In this way, energy absorbed by  $\text{Nd}^{3+}$  can be transferred to the  $\text{Yb}^{3+}$ , the emission energy of which is higher than the bandgap.

Rare earth organic complexes are composed of a ligand as an antenna and an emitting lanthanide ion. These complexes often feature large Stokes shift and avoid self-absorption losses but have limited absorption ranges making it difficult to harvest photons over a large spectral range. The luminescence process in organolanthanide complex occurs as follows: light is absorbed by a properly selected ligand. Intra-energy will be transferred from the singlet to the triplet states by inter-system crossing. Then the energy transfer will be from triplet state to the excited state of the  $\text{Ln}^{3+}$  ion.  $\text{Tb}^{3+}$  based organic complexes have a maximum emission efficiency around 500nm, which match the spectrum of amorphous Si solar cell,<sup>[50, 51]</sup> while NIR-emitting metal-organic  $\text{Yb}^{3+}$  or  $\text{Nd}^{3+}$  complexes are more suitable for c-Si solar cells.<sup>[52-55]</sup> However, the wide utilization of rare earth elements ultimately been limited by issues associated with overall quantum yield, abundance, and cost.

## Chapter 2

### Introduction to Luminescent Solar Concentrators

In this chapter, the principles underlying the electrical and optical properties of luminescent solar concentrators (LSC) will be reviewed. Specifically, the operational mechanisms of traditional luminescent solar concentrators will be described. Component efficiencies of the LSC operating process will be outlined in detail.

#### 2.1 Overview of luminescent solar concentrators

There are generally two categories of concentrators being widely developed, i) focusing-optics concentrators (often thermal concentrators) and ii) luminescent concentrators. A geometric focusing solar concentrator takes advantage of reflective or refractive surface to reflect, redirect, or focus incident radiation onto solar cells or energy-harvesting systems including parabolic troughs, heliostatic arrays, sterling dishes, and Fresnel reflectors.<sup>[56]</sup> This approach may work well in some configurations, but it suffers from two shortcomings. One is the cost for robust elements are often more expensive than the solar cells themselves. The other is that they often require solar tracking to harvest the direct components of the solar spectrum most effectively, which is often very cost prohibitive. Second, the use of tracking systems often prevents their incorporation into the building environment as they are typically bulky, heavy, and difficult to integrate seamlessly.

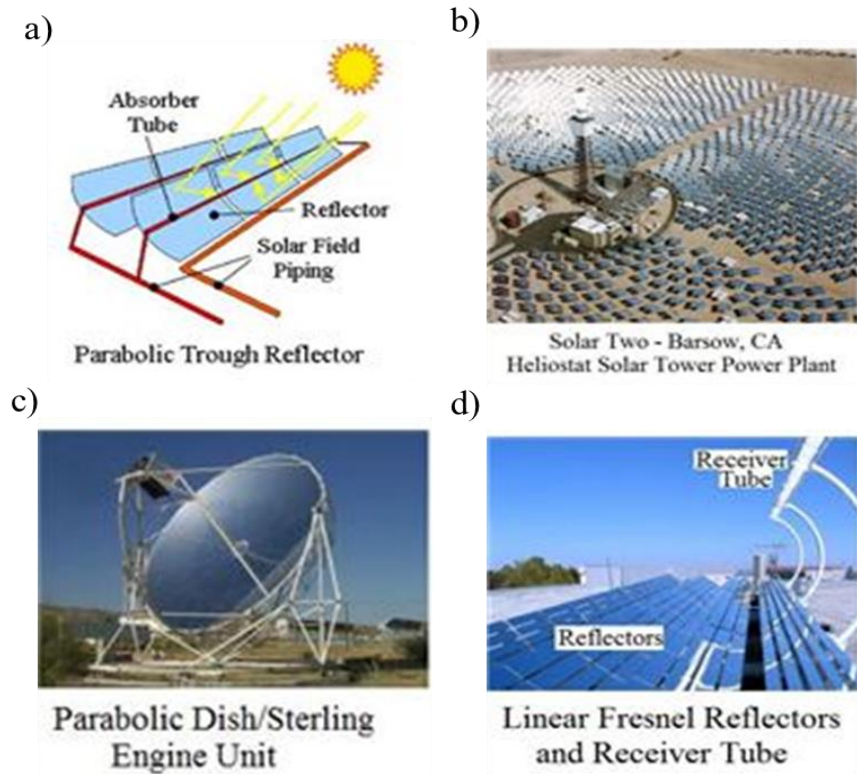


**Figure 2.1** Photograph of focusing-optics concentrators<sup>[56]</sup> a) parabolic troughs b) heliostatic arrays c) sterling dishes, and d) Fresnel reflectors

The luminescent concentrator, on the other hand, is a good alternative for its simplicity, ease of integration, and low cost. The basic LSC design allows sunlight to be absorbed by chromophores embedded in an inexpensive plastic or glass waveguide. The absorbed light is re-emitted at longer wavelength and a fraction of the emission light is trapped in waveguide by total internal reflection. Small PV cells are attached at the edge of the waveguide to collect the light and convert it to electricity, thus only requiring a small area of the expensive PV material.

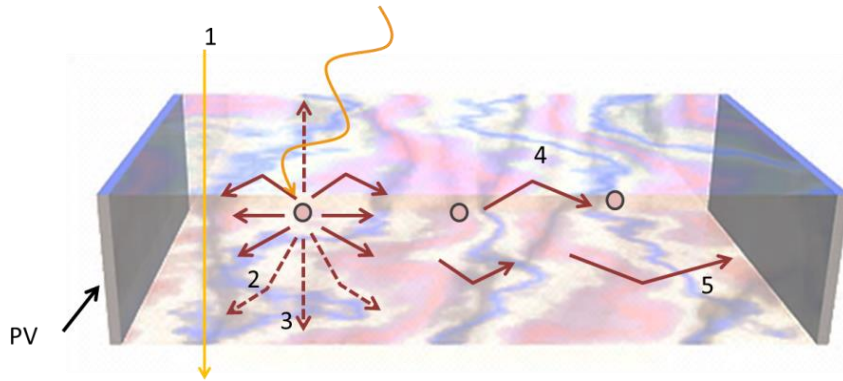


**Figure 2.2** Schematic of a luminescent solar concentrator composed of luminescent dyes, waveguide, and attached PVs. PVs are typically mounted around every edge, but have been omitted from the front and back for schematic clarity. The component efficiencies shown in the configuration are 1) solar spectrum absorption efficiency 2) luminophore photoluminescence efficiency (quantum yield efficiency) 3) waveguide efficiency 4) re-absorption efficiency 5) solar cell quantum efficiency

The concept of luminescent solar concentrators (LSCs) has existed for over 30 years, and with recent advances in phosphorescent and fluorescent luminophores efficiencies, the power conversion efficiency for LSC modules have increased to 7.1% using multi-dye systems with GaAs photovoltaics.<sup>[57]</sup> Although optical funneling limits the realistic overall system conversion efficiency of LSCs to less than 20%,<sup>[58]</sup> it can dramatically reduce the area of expensive solar cells needed, driving down the overall module cost.<sup>[15, 59-62]</sup> A review of the highest efficiency LSCs performance metrics are shown in Table 2.1. Note that metrics are for strongly colored (or black) LSCs, which absorb and emit in visible spectrum.



**Figure 2.3** Photograph of typical colorful luminescent solar concentrators highlighting the waveguided emission that is brightly focused at the edge. (b) Example of a traditional LSC in front a window, highlighting the difficulty in installing these systems in a variety of applications such as windows.

**Table 2.1** Efficiency of highest performance LSCs from the literature.

Dye	Cell	LSC size (m x m)	Efficiency (%)	Reference
Red305, CRS040	GaAs	0.05 x 0.05	7.1	[57]
BA241, BA856	GaInP	0.05 x 0.05	6.7	[63]
Rubrene, DCJTB	CdTe	0.1 x 0.1	4.7	[64]
CdSe/CdS/CdZnS/ZnS	Si	0.05 x 0.03	2.8	[65]
CdSe/CdS	GaAs	1.4 x 1.4	4.5	[66]
Red305, perylene perinone	Si	0.05 x 0.05	4.5	[67]
SrB <sub>4</sub> O <sub>7</sub>	Si	0.05 x 0.05	2.5	[67]
EuTT	Si	0.1 x 0.1	0.28	[68]

## 2.2 Luminophores

Luminophores in LSC systems are the molecules which absorb and emit photons. Here, we specifically distinguish between the terms “chromophore” and “luminophore” – chromophore has historically implied the absorption or emission of light in the generation of color whereas a luminophore does not necessarily impart color. A luminophore is regarded as effective if it meets following requirements<sup>[69]</sup> for LSC applications: 1) it should have broad spectral absorption, which means it can make maximum use of the incoming light of interest or key wavelengths of particular interest; 2) the quantum yields for luminescence should be high (as close to 1 as possible); 3) the Stokes shift should be large enough so that the overlap of the absorption and emission is small or negligible; and 4) the luminescence wavelength is well-matched to the solar cell spectral response.

Based on the requirements above, a variety of luminophores are widely being explored for LSC applications. Generally, effective luminophores fall into several categories: 1) organic dyes 2) quantum dots, 3) nanoclusters, and 4) rare earth ions, which are described above.

## 2.3 Waveguide and Hosts

The host is the matrix that surrounds the luminophore and is critical for 1) creating light trapping of the luminescent emission; 2) physically separating molecules to increase quantum yields; 3) interacting directly and electronically with the molecules to increase or decrease quantum yields through various interactions; 4) and encapsulate the chromophore to act as a barrier to air, moisture, and increase longevity. Because host-

guest interactions are difficult to predict *a-priori*, we necessarily must screen a wide range to optimize for all system components. A key criterion for host selection is the absorption coefficient at both the absorbing and emitting wavelengths of the luminophore. Because the host will transport the emitted photons over long distances (cm to m), even small absorption coefficients can act to absorb this energy. Shown in Figure 2.4 is a comparison of absorption coefficients for glass and several representative polymers. Poly (methyl methacrylate) (PMMA), for example, is a common host polymer material for LSC for its highly transparency and stable chemical properties.

The waveguide in LSCs is the key structural support that is also used to transport the optical energy over large areas. Waveguide efficiency indicates how much light can be transmitted within the waveguide by total internal reflection. According to the Snell's law, if photons arrive at the interface at an angle larger than the critical angle, there is total internal reflection and the photons are trapped within the waveguide. The critical angle is defined as

$$\theta_c = \sin^{-1}\left(\frac{1}{n}\right) \quad (2.1)$$

Here  $n$  is the refractive index of the waveguide (and the refractive index of air is 1). The refractive index for representative materials is shown in Table 2.2.

**Table 2.2** Refractive index for common materials<sup>[70]</sup>

Materials	Refractive index
Air	1.00
Water	1.33
Titanium Dioxide	2.61
Ethanol	1.36
Acrylic glass	1.49
Polycarbonate	1.60
PMMA	1.49
Crown glass	1.52
Flint glass	1.61

The waveguiding efficiency as a function of index can then be shown as <sup>[69]</sup>

$$\eta_{\text{wav}} = \sqrt{1 - 1/n^2} \quad (2.2)$$

If the refractive index for the substrate is around 1.5, which is typical for most industrial glasses, nearly 75% of emitted photons will be waveguided to the edge. However, the larger the refractive index, the more light will be reflected at the interface. Thus to optimize the product of the reflection and waveguiding efficiencies, the optimal index is around 1.8-2.2. Waveguide roughness and optical transparency also play an important role as waveguides are scaled to around  $\text{m}^2$  areas, where both can act as reabsorption or scattering losses. Absorption coefficients for glass, quartz are shown in figure 2.4 and the low absorption coefficients lead to low reabsorption losses, which have significant effect when scaled up to larger area.

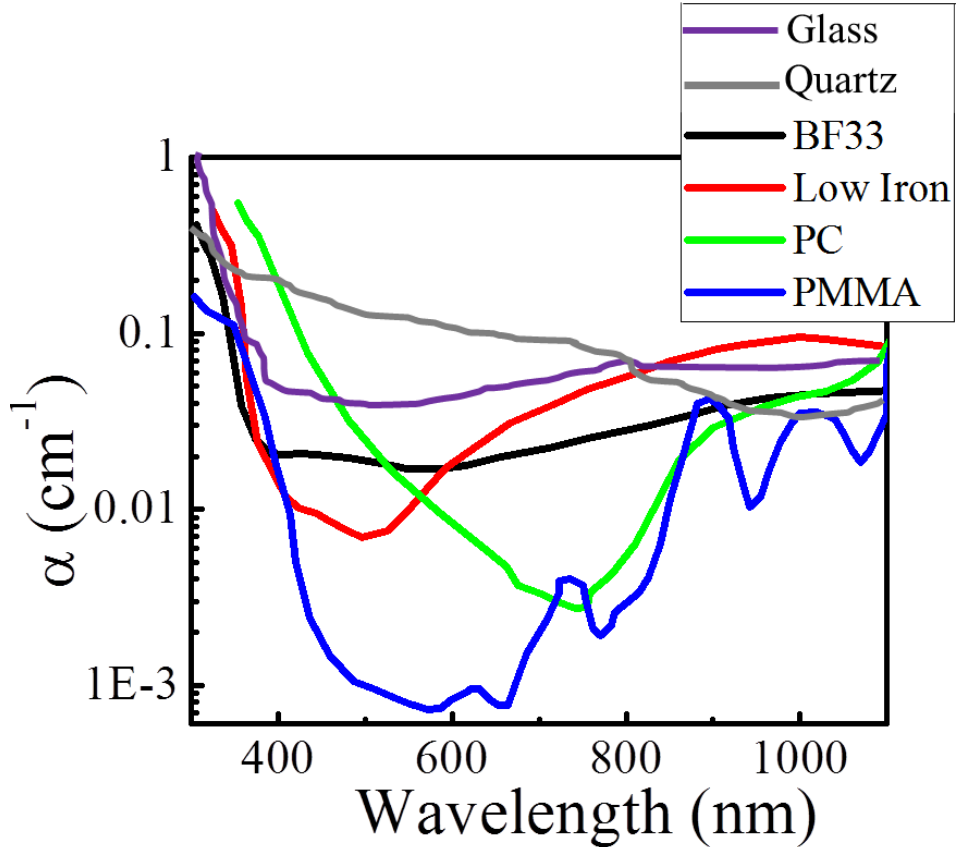


**Figure 2.4** Absorption coefficients of standard glass, quartz, BF33 glass, low iron glass, polycarbonate (PC) and poly(methyl methacrylate) (PMMA) <sup>[71]</sup> as a function of wavelength.

## 2.4 Overall LSC efficiency

The performance of the LSCs can be understood by the component efficiencies: 1) solar spectrum absorption 2) luminophore photoluminescence efficiency 3) waveguide (trapping) efficiency 4) solar cell quantum efficiency and 5) transport (re-absorption) efficiency. These processes are highlighted in the overall system LSC system efficiency as: <sup>[9]</sup>

$$\eta_{LSC} = \eta_{PV}^* \cdot (1 - R) \cdot \eta_{ABS} \eta_{PL} \eta_{trap} \eta_{RAE} \quad (2.3)$$

where  $R$  is the fraction of front face reflection,  $\eta_{abs}$  is the solar spectrum absorption efficiency of the luminophore,  $\eta_{PL}$  is the luminescence efficiency of the luminophore,  $\eta_{trap}$  is the waveguiding efficiency of the light,  $\eta_{PV}^*$  is the PV quantum efficiency (reported for AM1.5G) normalized by the solar spectrum absorption efficiency and the quantum efficiency at the luminophore wavelength, and  $\eta_{RAE}$  is the efficiency of transporting photons without reabsorption loss.<sup>[10]</sup> The luminescence efficiency and reabsorption efficiency are the most important parameters, especially for large area devices.

#### **2.4.1 Solar spectrum absorption efficiency**

For LSCs using down-converting luminophore dyes, the absorption efficiency is necessarily equal to, or less than, the absorption efficiency of the attached PVs. For reference, Si solar cells have 50.3% absorption efficiency for the solar spectrum. To maximize the absorption efficiency, it is important for the sheet to absorb as much of the incident light as possible, while also matching the emission with the absorption range of the mounted solar cells.

#### **2.4.2 Solar cell efficiency**

A range of solar cells can be utilized in the fabrication of LSC devices. By selecting a PV with quantum efficiency cutoff that closely matches the spectral emission of the luminophore, it is possible to minimize thermal losses (that is voltage). However, cost and availability will ultimately drive the cell design.

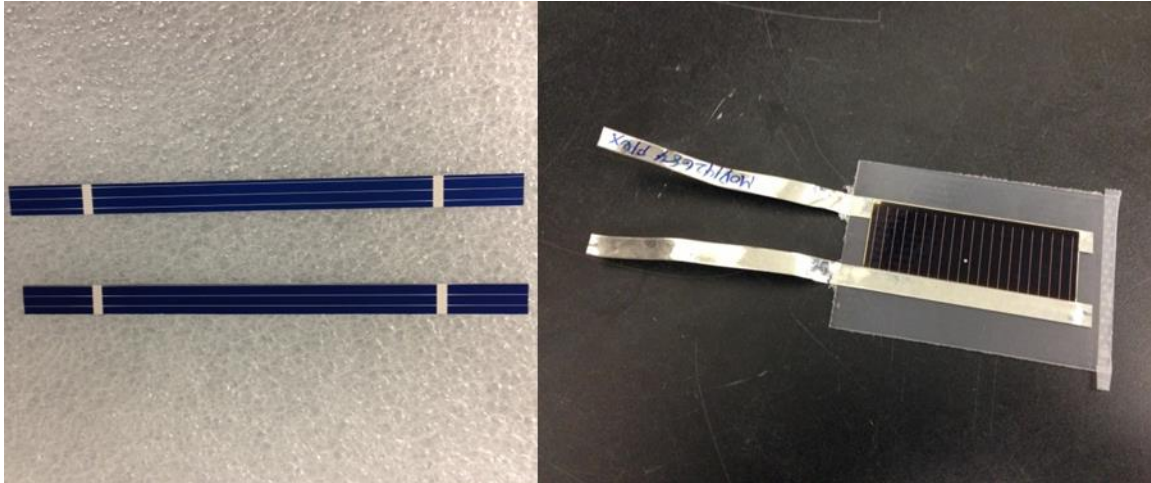


**Figure 2.5** Photos of cut Si cell (left) and GaAs cell (right) for attaching to the edge of the LSC waveguide.

Solar cells attached to the edge have quantum efficiency describing how many photons at a specific wavelength will be converted to electrons. The best Si cells have a quantum efficiency as high as around 85% in the range of 600-1100 nm. The best GaAs cells have quantum efficiency close to 95% at wavelengths  $< 900$  nm. Beyond the quantum efficiency, additional PV losses stem from the intrinsic thermodynamically-limited shape of the current-voltage curve. As the solar cell band gap decreases, voltage and fill-factor losses generally increase. Due to the monochromatic emission nature of the LSC, only single junction PVs can be considered around each individual LSC, defining the upper bound for the solar cell efficiency to that of the single-junction defined by Shockley-Quiesser. Figure 2.6 shows the solar cell efficiency normalized by the absorption efficiency for LSC uses.

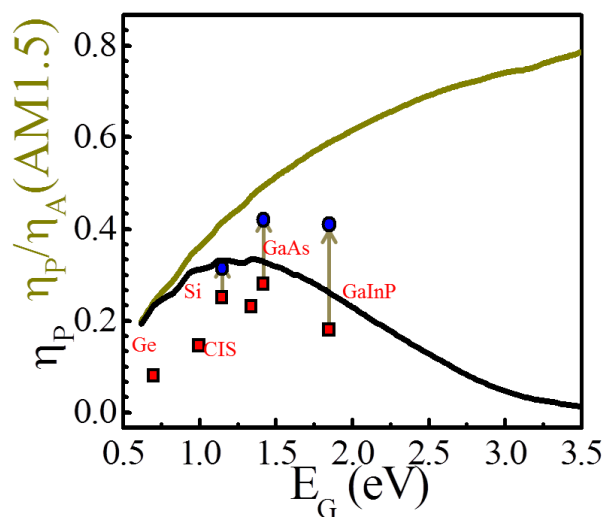


**Figure 2.6** Plot of the AM1.5G Solar Cell Efficiency as a function of bandgap (black), and efficiency normalized by the AM1.5 absorption efficiency (gold). Highest reported efficiencies are highlighted in red squares.

### 2.4.3 Reabsorption efficiency

It has long been recognized that LSCs are most limited by reabsorption losses, particularly for larger plate sizes. Indeed, much of the research with LSCs has focused on the reduction of these reabsorption losses. Reabsorption efficiency describes the probability that an emitted photon will be transmitted to solar cells without being reabsorbed by another luminophore. These losses are critically dependent on the quantum yield of the dye, the overlap (or Stokes shift) of the dye emission-absorption, and the overall waveguide dimensions. Although reemission may occur after reabsorption (particularly for high QY luminophores), this still leads to energy loss because the emitted light is radiated in random directions and a small fraction will leave the waveguide after each event. It has been shown theoretically, that low QY massive Stokes-shift materials can be outperform fluorophores with unity quantum yields over

large LSC dimensions. That is, even for luminophore with 100% quantum yield, reabsorption losses can become dominant for luminophores with small Stokes shift in large waveguides since each absorption/emission event leads to a reduction of photon flux through cone emission from the front of the waveguide that effectively act as scattering events.

Reabsorption losses introduced by the luminophore have been reduced in previous work through 1) increasing Stokes shifts with organic phosphors,<sup>[72]</sup> 2) integrating multiple-dye optimizations to artificially increase the Stokes shift<sup>[73]</sup> or 3) resonance shifting,<sup>[74, 75]</sup> applicable only to neat-film dye layers less than several microns thick. However, the clearest paths to fully maximize the large-area scaling of these devices is through embedded collectors or incorporation of high-quantum-yield massive-Stokes-shift-lumophores (MSSL) where the former is beneficial for greater power output at the expense of poorer cost scaling and the latter is the most effective means to the realization of low-cost scaling.

## Chapter 3

### Transparent photovoltaics

In this chapter, we turn to the concept of transparent solar cells. We then introduce the idea of a clear, transparent luminescent solar concentrator and contrast this with recently demonstrated transparent organic solar cells. This will be followed by a discussion about application of transparent luminescent solar concentrators in a range of applications including as solar windows and the theoretical efficiency limits for transparent luminescent solar concentrator (TLSC) are described.

#### 3.1 Transparent solar cells

Transparent solar cells are a transformative new approach to deploy solar harvesting surfaces seamlessly around buildings, mobile electronics, and automobiles to generate power without knowing they are there. These systems can be achieved by selectively harvesting the UV or NIR parts of the solar spectrum, the parts we cannot see with our eyes. They can convert any surface into an electricity generating surfaces while maintaining the underlying aesthetic and design freedom. Previous efforts in constructing transparent or semi-transparent power-producing surface have focused on 1) optically-thin photovoltaics that have significant tinting or limited transmission,<sup>[11, 12]</sup> or have an inherent tradeoff between efficiency and transparency, 2) LSCs incorporating colored chromophores that have either absorption or emission in the visible spectrum, again creating significant tinting,<sup>[13, 14]</sup> or 3) focusing-optics systems using direct-light only that requires bulky solar tracking or optics.<sup>[15, 16]</sup> These approaches have been severely limited in their potential for window and display applications due to aesthetic properties,

bulkiness, or considerably limited transparency. They suffer from an inherent tradeoff between power conversion efficiency and visible transparency, since both parameters cannot be simultaneously optimized. Architectural adoption is impeded further with typical PVs that have non-uniform absorption within the visible spectrum, resulting in poor color rendering index, CRI (high colored tinting), and poor natural lighting quality. Recently, selectively absorbing near-infrared photovoltaics (PV) with high transparency have been fabricated by exploiting the excitonic character of molecular and organic semiconductors with efficiencies in the range of 2-4% over small areas ( $\text{mm}^2\text{-cm}^2$ ).<sup>[17-19]</sup> While these transparent photovoltaics offer the highest possible combination of transparency and efficiency, they also have strict defect tolerances, challenges with partial shading, and a different set of challenges to scale-up. In contrast, visibly transparent, UV/NIR-selective LSCs avoid aesthetic tradeoffs (low visible transmittance or CRI) that hinder architectural adoption and provide a clear route to large area scaling.

### **3.2 Transparent luminescent solar concentrator for solar windows**

According to the U.S. Energy information Administration (EIA), the buildings sector consumes nearly half (47.6%) of total energy produced in the Unit States. About 75% of all the electricity produced is consumed by operating buildings. While more than half the generated electricity is lost in distribution, it is critical to design sustainable and energy-efficient buildings or exploit existing infrastructure to reduce cost for renewable energy. Accordingly, many participants in the built environment are looking for solutions to curb energy demand and generate renewable energy on-site. Solar energy offers a viable solution to our growing energy need, but adoption has been slow due to cost and difficulties with seamless integration.

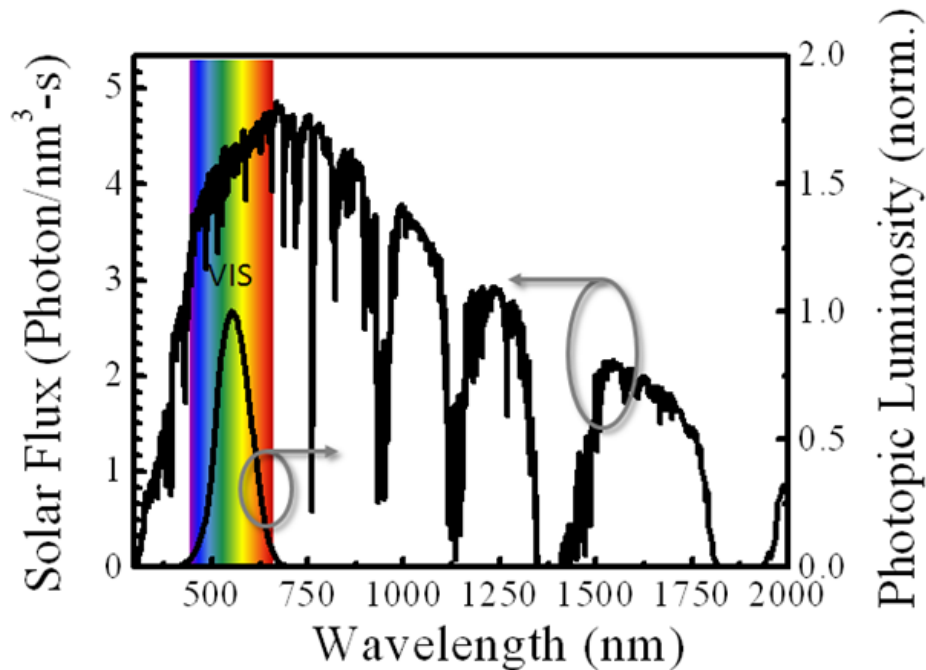


**Figure 3.1** Overlap of the AM1.5G solar flux and the photonic response of the eye shows that about 1/3 of the photon flux is in the visible part of the spectrum with the remaining 2/3 of the flux in the NIR

Roughly 20% of all building electricity in the U.S. is used for lighting. Incentivizing solar window adoption can encourage architects to utilize more window space, increasing natural lighting, and reducing lighting costs. Reproducing the solar spectrum is the goal of most artificial lighting applications. For example, despite significant enhancements in power efficiency, fluorescent bulbs have failed to eliminate incandescent bulbs in large part due to their reduced color rendering quality that has created social barriers to implementation. In contrast, natural lighting through windows and skylights provides high quality light, reduces additional daytime lighting requirements and generates a pleasing ambience. For non-niche applications it is important to assure that transmitted light remains high color quality (as good as or better than, e.g. ceiling lighting) since it will offset some form of artificial lighting. Each solar window will impart a small modification to the spectrum transmitted. Thus, we utilize the color rendering index (CRI,

see Section 4.4) evaluation by convoluting the transmission spectra with the solar spectrum (e.g. AM1.5G). The color rendering framework is useful for defining the visible part of the spectrum that should be transmitted and the components that can be utilized for power generation.

There is significant interest in the solar field in creating three-dimensional structures, such as solar towers and obelisks to enhance solar collection.<sup>[76]</sup> These structures can collect substantially more flux than solar tracking units of an equivalent footprint. Likewise, buildings can act as excellent solar collectors, collecting sunlight effectively throughout the day on each face. When energy-scavenging devices are installed to the window can also help cool the buildings. A significant fraction (~15%) of building electricity is utilized for air-conditioning. Conversion of electricity to heat is highly efficient (nearly 100%), while cooling efficiencies are significantly lower. Solar windows can dramatically reduce unwanted solar heating from infrared flux by utilizing this energy for electricity generation and rejecting the rest from transparent, NIR-selective mirrors. In fact, many researchers and companies are exploring coating technologies to achieve IR-rejection functionality alone, even in colder climates.<sup>[77]</sup> It is an added benefit to utilizing this unwanted resource for electricity generation that could compliment or replace current low solar heat gain coefficient coating technologies. This hear-rejection functionally can enhance the effective LSC from direct power generation by 50-100%.

Integrating solar-harvesting systems into the building envelope is a transformative route to improving building efficiency, capturing large areas of solar energy, and lowering effective solar cell installation costs by piggybacking on the installation, framing, and maintenance of the existing building envelope. There has been

demonstrated interest in utilizing LSCs as architectural windows.<sup>[69, 78-82]</sup> However, the widespread adoption of such a pathway is typically hampered by difficulties associated with mounting traditional photovoltaic (PV) modules in non-standard configurations on and around buildings due to added structural cost, architectural impedance, and most importantly, aesthetics. To overcome these hurdles we have developed UV absorbing and NIR absorbing luminescent solar concentrators which are highly transparent in the visible spectrum and enable integration onto window and glazing systems in the building envelope without disrupting the visible components or require solar tracking. These transparent LSCs offer a different route to large area scaling with high defect tolerances compared to other transparent photovoltaic devices. These LSC systems present opportunities for non-tinted, highly transparent solar-scavenging windows that can translate into improved building energy efficiency and lower cost solar harvesting systems beyond the building skin including 1) energy scavenging electronics displays, 2) autonomous electrochromic-windows, 3) visible-blind detectors, and 4) coatings for improved UV response and protection of traditional solar installations. These LSCs can generate electricity from both direct and diffuse light, and enhance the low-light efficiency through solar concentration while maintaining window glass aesthetics and architectural design freedom. Successful commercialization of this technology will result in affordable net-zero-energy buildings which can be widespread throughout the build environment.

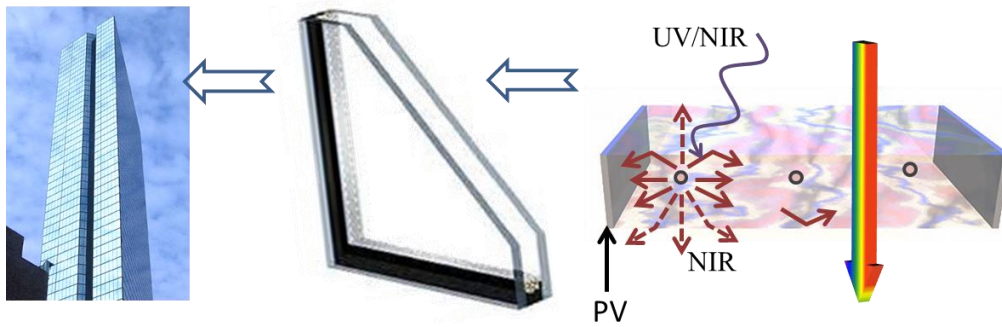


**Figure 3.2** Diagram of the point of installation for building glasses with transparent luminescent solar concentrators

### 3.3 Theoretical and Practical Limits of Transparent Luminescent Solar Concentrators

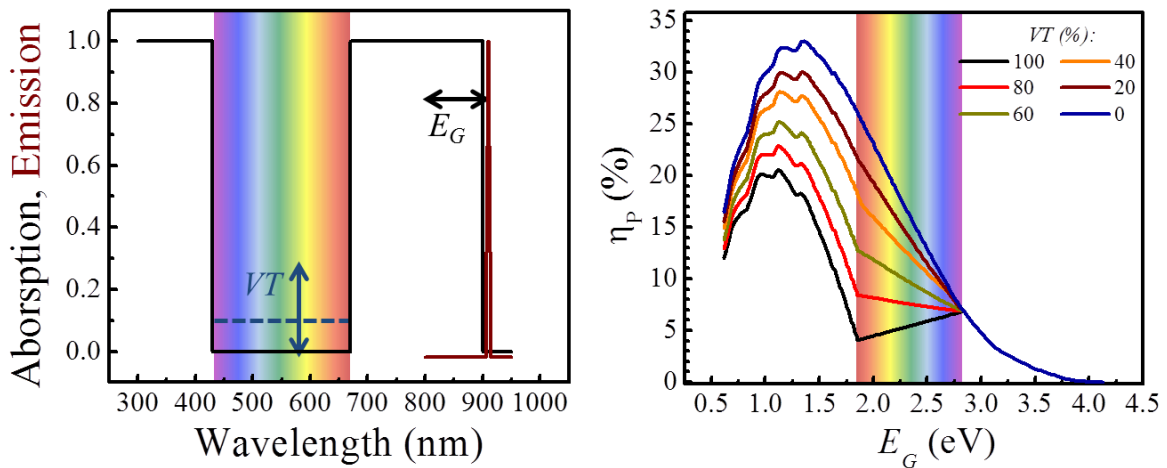


**Figure 3.3** Transparent PV theoretical efficiency limits as a function of bandgap and level of visible transparency (VT). Note that these limits are the same for transparent LSCs with ideal absorption/emission profiles with no spectral overlap.

The theoretical limits of transparent luminescent solar concentrators are fundamentally constrained by those of the transparent photovoltaic (see Figure 3.3).<sup>[83]</sup> Interestingly, without harvesting any visible light the theoretical efficiency limit for transparent devices (single junction) is over 20%. For reference, the single junction opaque limit is 33.1%. Using this as a starting point the limits of TLSC are derived as a function of key idealized

parameters outlined below (see Figure 3.4). It should be noted that the practical considerations of the performance of the TLSC is dependent on a greater number of parameters and subsystems and thus follows a linear progression in this analysis. We start from the most idealized case and analyze a number of cases as the idealized parameters are relaxed.

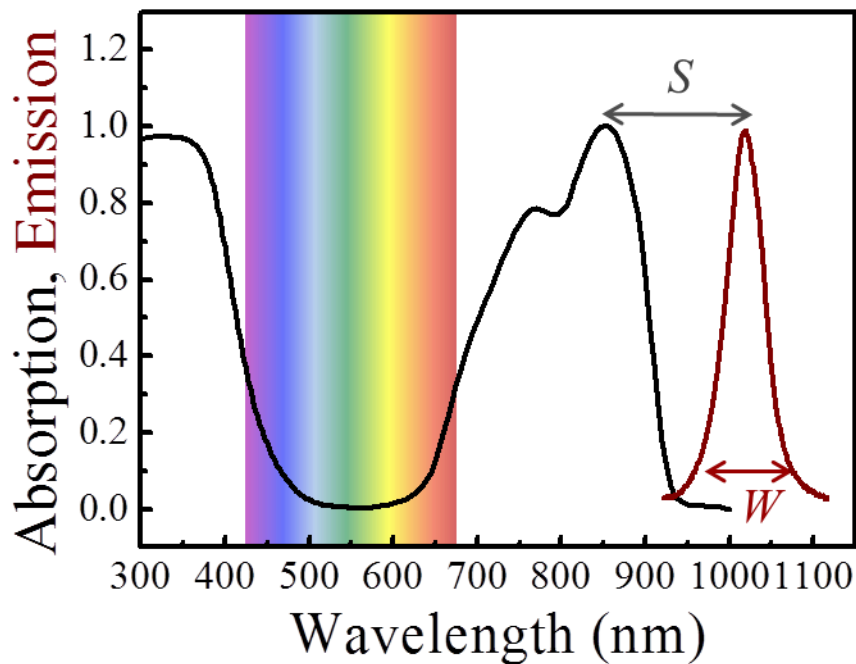


**Figure 3.4** Representative absorption and emission characteristics of TLSC emitters. The Stokes shift ( $S$ ) and emission width ( $W$ ), two key emitter parameters, are highlighted.

The ideal transparent solar concentrator requires the following conditions be met: 1) the PL efficiency is 100%; 2) the PV mounted around the edge has an efficiency and quantum efficiency equal to the Shockley–Queisser limit; 3) there are no reflection losses into the luminescent absorber; 4) there are no waveguiding losses (perfect light trapping); 5) there is no overlap between the emission and absorption (no reabsorption losses); 5)

there is no intensity dependence to the edge mounted PV; and 6) the emission width ( $W$ ) is perfectly narrow. In this case, the efficiency limit is 20%, identical to TPVs.

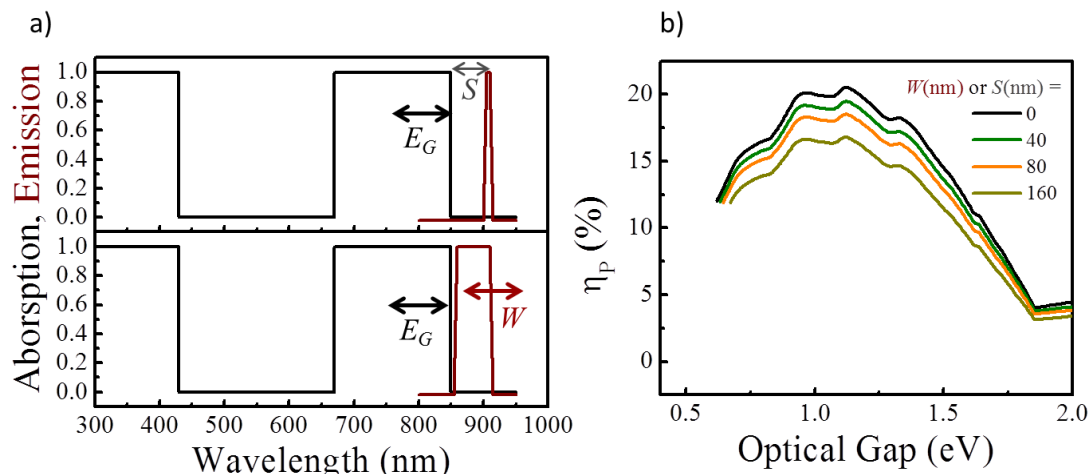


**Figure 3.5** TLSC practical efficiency limits with no ideal absorption/emission profiles with no spectral overlap as a function of the a) emission width ( $W$ ) with  $S = 0$  or b) Stokes shift ( $S$ ) with  $W = 0$ . Note that the decrease in efficiency stems from a lower theoretical voltage and FF from the PV cell mounted around the edge. However, the situation in b) has a distinct advantage in practice since it will suppress reabsorption losses in non-ideal absorption emission overlap configurations. That is, narrow emitters will always provide greater flexibility for larger Stokes shifts and minimized reabsorption losses.

The ideal case is extended to luminophores with a finite emission width ( $W$ ) as a function of  $S$ . This is one of the first key areas of loss as it confines the solar spectral range that can be harvested for a given PV bandgap and dictates the “voltage loss” required in selecting a particular PV cell. For example, given a particular molecule emitter with a defined absorption, the smaller the  $W$ , the higher voltage PV can be selected. A range of emission widths have been demonstrated for organic molecules (50-100nm),<sup>[84]</sup> nanoclusters (50-300nm),<sup>[72, 85]</sup> J-aggregates (10-20nm),<sup>[86]</sup> nanocrystals (10nm),<sup>[87]</sup> and carbon nanotubes (10nm)<sup>[88]</sup> suggesting that such losses can, in fact, be minimized. Nonetheless, for the most efficient emitters, this value of  $W$  is typically around 100nm.

For practical efficiency limits we consider the case where: 1) the PV quantum efficiency is 90% (typical for GaAs and Si) with a 1-sun photovoltage that is 90% of the SQ limit;<sup>[89]</sup> 2) the waveguiding efficiency is 85% ( $n = 1.7$ ); 3)  $W = 80\text{nm}$  and  $S = 80\text{nm}$ , and 4) the emitter is 100% with no reabsorption losses. This results in a practical efficiency limit of 11.6% for an emitter bandgap of 1.12eV. The practical efficiency limits track surprisingly close to that for transparent photovoltaics which was estimated to be 11%, also with a bandgap of 1.12eV.<sup>[83]</sup>

Moving forward, it then becomes a materials development challenge to create emitters with high quantum yield, optimal bandgap and wavelength selectivity, and a combination of both narrow emission and moderate Stokes shifts. Provided these properties are met, highly efficient and exceptionally low cost transparent solar harvesting systems can be developed and deployed.

## **Chapter 4**

### **Experimental Techniques**

In this chapter, key experimental techniques utilized to measure chemical, optical, and electrical properties of materials and devices are discussed. We begin with a discussion of luminescence spectroscopy, and luminescence quantum yield measurements. We then describe optical absorption, reflection and transmission measurements, followed by electrical solar cell testing and quantum efficiency measurements. Finally, simulation methods are described and discussed.

#### **4.1 Photoluminescent emission and excitation testing**

Photoluminescent spectra are measured with a spectrofluorometer. The spectrofluorometer uses an optical excitation source to pump a thin film or solution sample while recording the intensity and wavelength of photons emitted from the sample. Emission intensity of a particular wavelength (as selected by the output monochromator) is detected for emission scans. For excitation scans, the pump wavelength is scanned through a range, with the emission wavelength of the output monochromator fixed at one specific emission wavelength. As with the emission scan, a background scan is performed for each sample over the same wavelength range.

Filters are used to help reduce the influence of the background and prevent false signals (e.g. wavelength doubling) in the monochromators. There are two types of filters commonly utilized in these experiments, short pass and long pass filters. They are

typically fabricated with absorptive molecules or multilayers of dielectric films. Long pass filters enable any wavelength longer than wavelength cutoff to be transmitted, as the name implies, while short pass filters enable any wavelength shorter than the cutoff wavelength to be transmitted. Filters can be placed both excited side and emitted side and their selection is important in the design of the experiments. Example test fixtures for both solution and solid films are shown in Fig 4.2

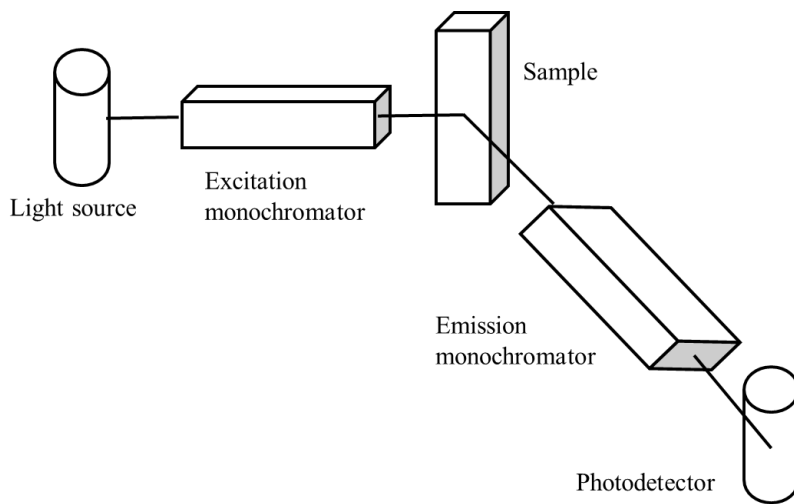


**Figure 4.1** Schematic of spectrofluorometer system

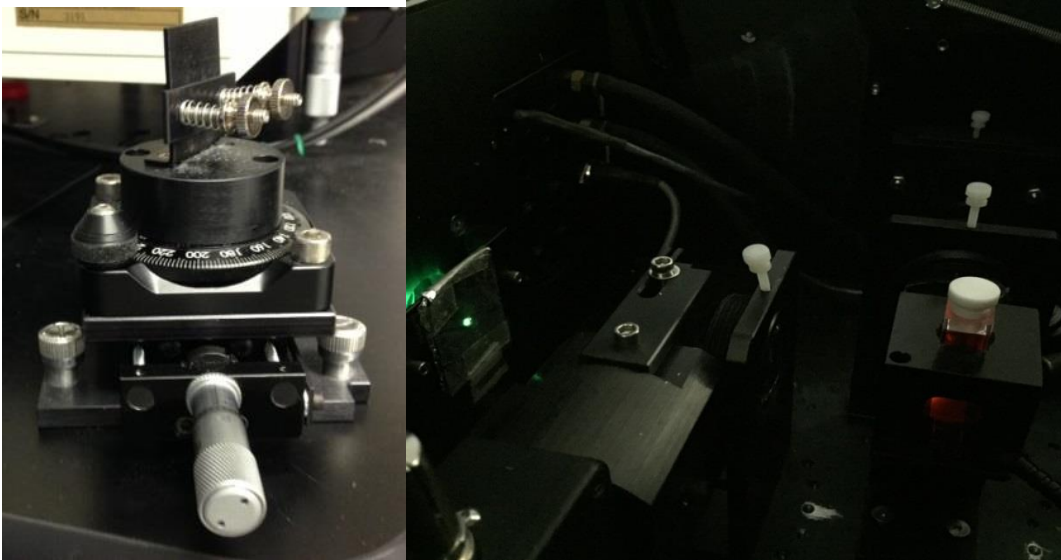


**Figure 4.2** Images of the solid film (left) and solution (right) sample holder for photoluminescent excitation and emission measurements. Red glow from a chromophore solution can be seen with green excitation at 550 nm.

#### 4.2 Quantum yield measurement

Photoluminescence quantum yield (QY) can be measured in a variety of ways: using reference dyes of known quantum yield and index, by concentration curves, or in integrating spheres.<sup>[90-94]</sup> The most reliable method is the use of integrating sphere which does not require any other reference dye samples (which can easily be contaminated or diminished performance) and can be made with two simple scans and minimal error bars. In an integrating sphere, all light from the luminescent sample including waveguided and forward emitted/reflected light is uniformly redistributed throughout the sphere by a reflective coating with nearly 100% reflectivity. (Gamma Scientific) Because of this uniform redistribution, the excitation or luminescence emission can be detected at any point of the sphere, typically as a small exit aperture directed toward the output monochromator. Two scans are performed for each sample over the full wavelength range and with the same configuration; the first scan is performed with a reference

substrate or cuvette without dye to measure the total excitation intensity. The second scan is performed for the desired sample. The reference or background scan is then generally subtracted from the sample scan around the luminescence region of the spectra. By recording the change in the excitation intensity with a blank and the sample under test, the quantum yield is calculated as:<sup>[28]</sup>

$$QY = \frac{\nu_{em}(\lambda_{em}) \int \frac{\lambda}{hc} I_{em} d\lambda}{\nu_L(\lambda_L) \int \frac{\lambda}{hc} [I_B^L - I_F^L] d\lambda} \quad (4.1)$$

where  $I_{em}$  is the luminescent intensity from the film,  $I_B^L$  is the excitation intensity from a bare substrate,  $I_F^L$  is the excitation intensity from the tested film,  $\nu_{em}$  is the calibration factor (for spectrometer, integrating sphere and fiber coupling) at the wavelength range of the emission, and  $\nu_L$  is the calibration factor at the wavelength range of the excitation light.

To measure the quantum yield, an integrating sphere is loaded directly in the spectrofluorometer to ensure that all light illuminating the sample is collected (overall wavelengths and emission angles). The testing procedure is similar to the procedure for emission spectra except that the emission range must include the excitation wavelength.

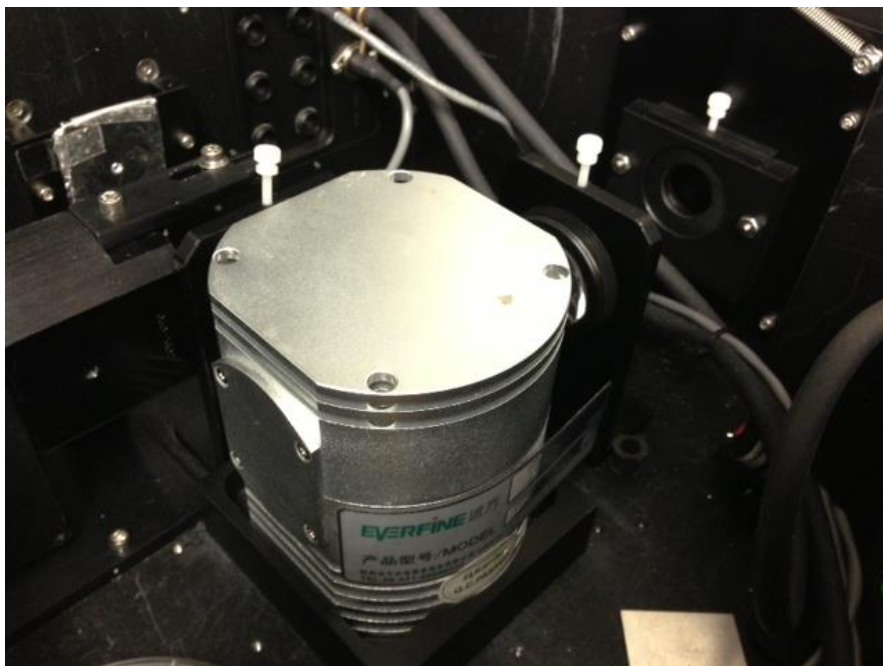


**Figure 4.3** Photo of an integrating sphere for quantum yield measurement

Figure 4.4 shows an example of quantum yield measurement data for a diphenylanthracene (DPA) film. The quantum yield can be calculated by dividing the difference of the absorption and emission peak for the two films, respectively.

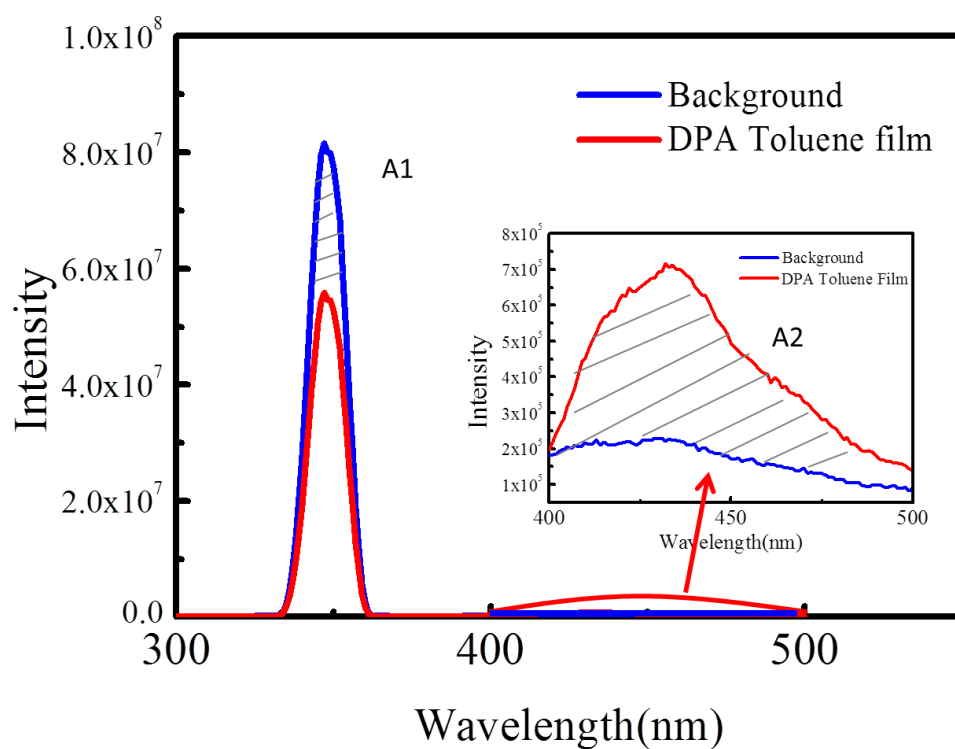


**Figure 4.4** Quantum yield data for a 9,10-Diphenylanthracene (DPA) film. DPA is dissolved in toluene and spin-coated as film. The background glass sample (blue) and DPA film sample (red) spectra are plotted. (inset) The emission peaks for the two films.

### 4.3 Optical absorption, reflection and transmission

When photons are incident on the surface of the materials, they can be absorbed, reflected, scattered, or transmitted.

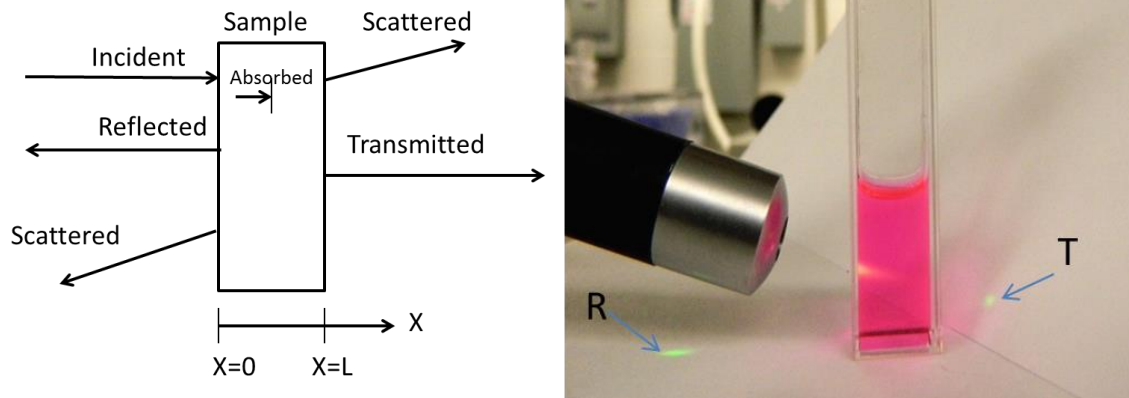


**Figure 4.5** Schematic of processes of absorption, reflection, scattering, and transmission which occur when incident light passes through a sample with a thickness of  $L$  (left); Visualization of the transmission, absorption and reflection from a rhodamine solution illuminated with a green laser (right) – note that the exponential absorption profile can be seen in the solution as.

Figure 4.5 shows absorption, transmission, scattering processes that can occur at a sample surface. The light enters the sample at  $X=0$  is

$$I(0) = I_0(1 - R) \quad (4.2)$$

$I_0$  is the total incident light intensity and  $R$  is the fraction of the light reflected at the front surface. For unpolarized light at normal incident to a flat surface (with one surface), the fraction of light reflected is given by:

$$R = (n - 1)^2 / (n + 1)^2 \quad (4.3)$$

where  $n$  is the refractive index of materials, while the  $n$  for air is 1.

The light intensity, which is a measure of the flux of photons in the optical beam, decreases through the sample as the photons are absorbed. Assuming there is a uniform probability of absorption throughout the sample, the intensity reaching distance  $X$  into the sample is described simply by the Beer-Lambert equation:

$$I_i(\lambda) = I_0(\lambda) \cdot e^{-\alpha L} \quad (4.4)$$

where  $\alpha$  is the optical absorption coefficient and is linearly related to the concentration of the sample and a strong function of wavelength. Transmission,  $T$ , is then defined as:

$$T(\lambda) = \frac{I_t(\lambda)}{I_0(\lambda)} \quad (4.5)$$

The relationship between absorption ( $A$ ), transmission ( $T$ ) and reflection ( $R$ ) is then related by the population (or energy) balance as:

$$A + T + R = 1 \quad (4.6)$$

In many experiments, a reference sample is typically utilized in dual beam spectrometers to correct for reflections and simplify the measurement or calculation of the absorption or absorption coefficient (for solution sample, a pure solvent sample is as controls and for films substrate film is the control sample). However, because of the complexity of accounting for reflections in thin samples, reference samples should generally not be utilized with samples with thin films. In this case it is better to directly measure  $R$  and  $T$  independently with different test fixtures. Nonetheless, it is also important to note that when measuring  $T$  for devices, it is often the overall transmission that is of greatest concern, and reference samples are not utilized for such absolute measurements.

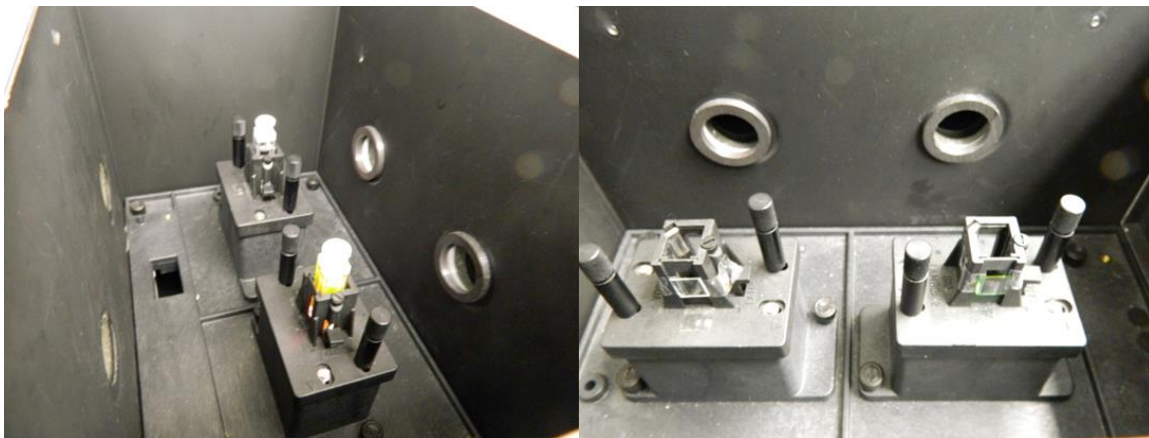


**Figure 4.6** Photos of transmission measurement of liquid sample in cuvette (left) and film samples on glass (right)

#### **4.4 Electrical, $J$ - $V$ and EQE measurements**

Current density versus voltage ( $J$ - $V$ ) measurements were obtained under simulated AM1.5G solar illumination corrected for solar spectrum mismatch.<sup>[95]</sup> Light from a xenon arc lamp is collimated and simulated as AM1.5G solar spectrum. The illumination area, with a diameter of 2.5 cm, uniformly covers a masked region of the sample, but limits the overall LSC test size. A range of neutral density filters positioned between the light source and the sample enabled measurement of different illumination intensity. The  $J$ - $V$  curve of the LSC device or module is measured with a Keithley sourcemeter.

Figure 4.7 shows device set for  $J$ - $V$  testing. Two cells were mounted on orthogonal edges and connected in parallel. The remaining two edges were covered with enhanced specular reflector (Vikuiti, 3M).

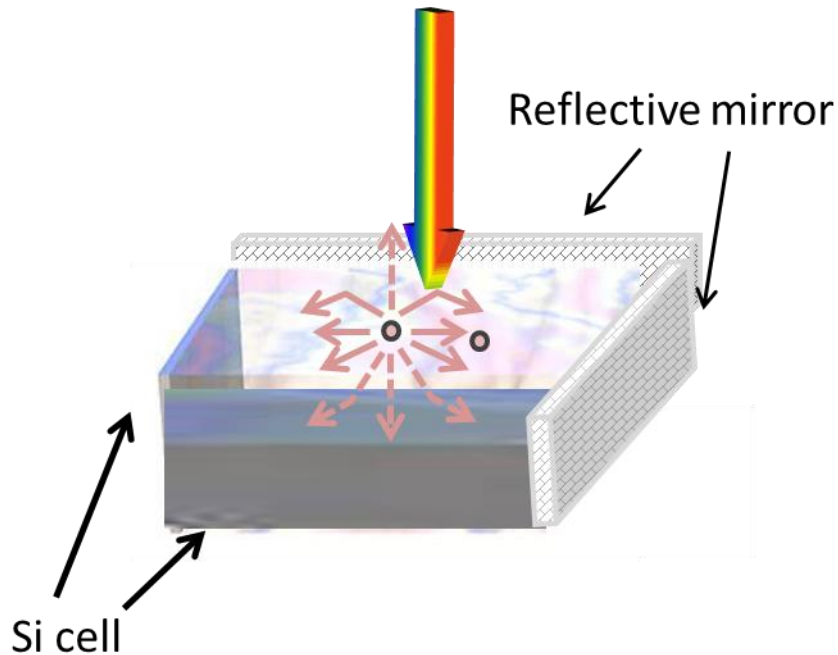


**Figure 4.7** Configuration of *JV* testing for a TLSC system. An additional mask is used to block the edge of the cells from direction illumination.

External quantum efficiency (*EQE*) is an important characteristic of all solar cells that describes the efficiency of electron generation at each wavelength in the solar spectrum. The external quantum efficiency is measured as follows. The light from a xenon lamp is directed through a filter wheel chopped at 75Hz, into a monochromator to produce monochromatic beam that is fiber coupled to a sample. The monochromatic light illuminates a small area of the sample (under filling) and the generated current is detected with a lockin amplifier.

When testing the EQE for an LSC device, only one solar cell was mounted around the edge. The remaining 3 edges were blocked with black electrical tape to eliminate edge reflections and simplify the geometric configuration for the EQE measurements.. To avoid any direct illumination of the solar cell, a thin mask was used to define the active area around the LSC edges and shield the edge-mounted PVs. Due to the illumination

area of the solar simulator (67005 Xe arc lamp, Newport) plate lengths for power efficiency measurements were limited to  $< 0.05\text{m}$  and for EQE measurements  $< 0.2\text{m}$ .

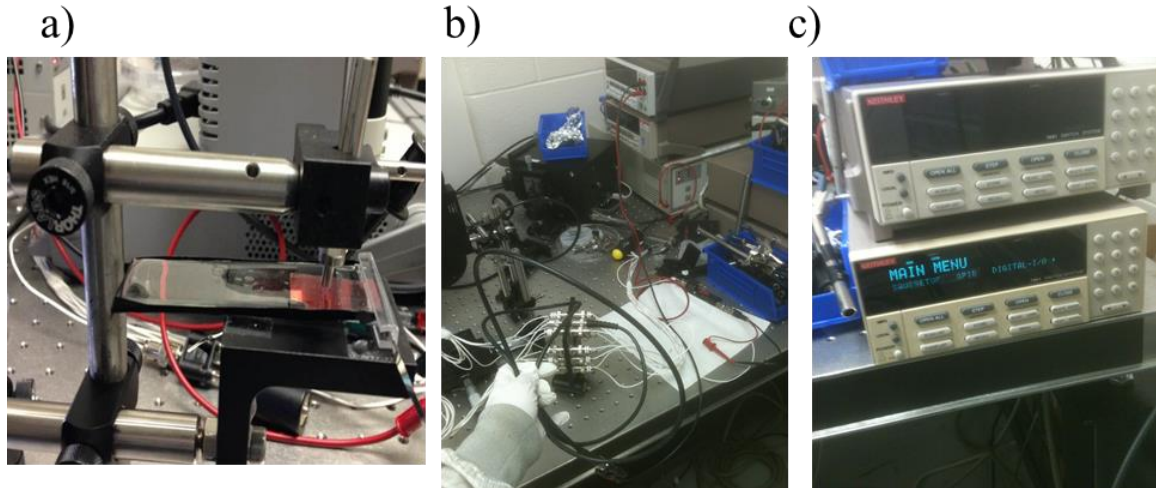
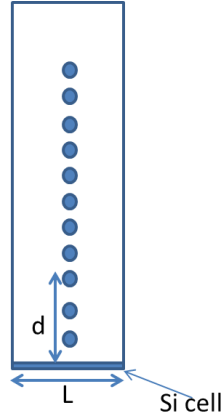


**Figure 4.8** Photo of EQE measurement a) monowavelength signal illuminating on the surface of the test sample b) the test fixture connected to the Keithley picoameter for current readings and c) the Keithley sourcemeter and channel switcher for testing multiple devices.

To predict scalability, reabsorption losses, etc, EQE measurements were obtained by directing a monochromatic excitation beam from a fiber perpendicular to the LSC at various distances ( $d$ ) from a single edge-mounted PV. The measured EQE was then corrected by the factor,  $g = \pi / \tan^{-1}(L/2d)$ ,<sup>[12]</sup> due to the different angle subtended by the solar cell at each spot distance, where  $g$  is the geometric collection correction for collecting photons only on one edge of the concentrator (the rest of the edges are blackened),  $d$  is the distance from the illumination spot on the LSC and  $L$  is the length of the collection edge of the LSC. The EQE was measured utilizing a Newport calibrated Si detector.<sup>[12]</sup>



Correction:  
 $g = \pi / \tan^{-1}(L/2d)$

**Figure 4.9** Correction for EQE measurement at distance of  $d$  to the edge when one PV cell is attached.  $L$  is the plate width and  $g$  is geometric factor. The measured EQE is corrected by the geometric factor.

#### 4.5 LSC simulations

As discussed in previous chapters, the efficiency an LSC system is comprised of component efficiencies defined by equation 2.3. Here we derive the reabsorption losses as a function of key parameters to simulate the scalability of a range of LSC devices. First, a collection efficiency  $Q$  is introduced to calculate the limit of reabsorption losses along the whole waveguide.  $Q$ , defined as the fraction of the absorbed solar photons that are transported to the PV, can be calculated as the sum of the collection efficiency of each absorption/emission event,  $Q_i$ , where  $i$  is the remission event number. <sup>[96]</sup>

$$Q = Q_1 + Q_2 + Q_3 + \dots \quad (4.7)$$

Each time a photon is reabsorbed prior to reaching the PV, it is still possible for the next remitted photon to reach the PV provided there is a high PL efficiency and the emitted photon is not emitted with the angle range of the escape cone. If the photon is emitted

within this escape cone it can be lost out of the front or back of the LSC.  $\eta_{RA}$  is then defined as the probability that luminescence outside the critical cone will be re-absorbed before it reaches the PV on the edge, and  $\eta_{RA}'$  is the probability of reabsorption for photons emitted within the critical cone.  $Q$  can be written as an infinite series as:

$$Q = \eta_{trap}(1-\eta_{RA})\eta_{PL} + \eta_{trap}(1-\eta_{RA})[\eta_{RA}'(1-\eta_{trap}) + \eta_{trap}\eta_{RA}]\eta_{PL}^2 + \eta_{trap}(1-\eta_{RA})[\eta_{RA}'(1-\eta_{trap}) + \eta_{trap}\eta_{RA}]^2\eta_{PL}^3 + \dots \quad (4.8)$$

Because 4.12 is a convergent series, it can be written more succinctly as:

$$Q = \frac{(1-\eta_{RA})\eta_{trap}\eta_{PL}}{1-\eta_{PL}[\eta_{RA}'(1-\eta_{trap}) + \eta_{trap}\eta_{RA}]} \quad (4.9)$$

Here we assume  $\eta_{RA}' = 0$  (there is no self-absorption in the critical cone) since we focus on thin films of luminophores. In this case,

$$Q = \frac{(1-\eta_{RA})\eta_{trap}\eta_{PL}}{1-\eta_{RA}\eta_{PL}\eta_{trap}} = \eta_{RAE}\eta_{trap}\eta_{PL} \quad (4.10)$$

where  $\eta_{RAE}$  is the total reabsorption efficiency in the waveguide:

$$\eta_{RAE} = \frac{1-\eta_{RA}}{1-\eta_{RA}\eta_{PL}\eta_{trap}} \quad (4.11)$$

Again, the energy conversion efficiency of the LSC is:

$$\eta_{LSC} = \eta_{PV}^* \cdot (1-R) \cdot \eta_{ABS}\eta_{PL}\eta_{trap}\eta_{RAE} \quad (4.12)$$

With each reabsorption-emission event, the efficiency will be impacted if both the quantum yield and waveguiding efficiencies are  $< 100\%$ . Unless reflectors can be

attached to the front and back side of the waveguide to reflect escaped emission light back to the waveguide, the waveguide efficiency will also impact the total reabsorption efficiency. Because of the light dependence of  $\eta_{PV}^*$  this correction is dependent on the geometrical gain of the collector, where the incident photon flux on the LSC is related to the photon flux around the edge as  $I = \left(\eta_{LSC} / \eta_{PV}^*\right) \cdot G \cdot 1sun$ .

Appreciating that the path length for reabsorption events depends on the emission angle within the waveguide, the attenuation along the photon trajectory is then modified from  $exp(-\varepsilon \cdot L)$  to  $exp(-\varepsilon \cdot (L \pm y) / \sin(\theta) \sin(\phi))$  where  $\varepsilon$  is the molar absorptivity,  $L$  is the plate length,  $\theta$  is azimuth relative to the normal of the LSC plane, and  $\phi$  is the normal rotation coordinate,  $y$  is distance along the plate direction parallel to  $L$ . The reabsorption efficiency  $\eta_{RA}$  can then be obtained by integrating the probability of arrival along all paths outside of the escape cone from a fixed volume element around the plate length, and over all emission wavelengths weighted by the normalized luminescence spectrum of the luminophore.

$$\eta_{RA} = \frac{\int_0^{\infty} PL(\lambda) d\lambda \int_0^L dy \int_0^{\pi} d\phi \int_{\theta_{crit}}^{\pi/2} \sin(\theta) d\theta \left\{ \exp\left[-\frac{\varepsilon(\lambda) \cdot C(L-y)}{\sin(\theta) \sin(\phi)}\right] + \exp\left[-\frac{\varepsilon(\lambda) \cdot C(L+y)}{\sin(\theta) \sin(\phi)}\right] \right\}}{\int_0^{\infty} d\lambda \int_{\theta_{crit}}^{\pi/2} d\phi \int_{-\pi/4}^{\pi/4} \sin(\theta) PL(\lambda) d\theta} \quad (4.13)$$

where  $C$  is the concentration, and the luminescence spectrum,  $PL(\lambda)$ , is the normalized luminescence spectrum. The two exponential terms result from the fact that the light is guided in both directions along the length with  $y = 0$  defined in the center of the

waveguide. The integral over  $y$  can be obtained analytically, and rearranging the order of integration considering variable dependencies  $\eta_{RA}$  is:

$$\eta_{RA} = \frac{\int_0^{\infty} PL(\lambda) d\lambda \int_{\theta_{crit}}^{\pi/2} \sin(\theta) d\theta \cdot \int_{-\pi/4}^{\pi/4} d\phi \cdot \left( 1 - \exp\left[-\varepsilon(\lambda)C \frac{L}{2 \sin(\theta) \cos(\phi)}\right] \right)}{\int_0^{\infty} d\lambda \int_{\theta_{crit}}^{\pi/2} d\theta \int_{-\pi/4}^{\pi/4} \sin(\theta) PL(\lambda) d\phi} \quad (4.14)$$

Finally, accounting for the fractional time each photon spends in a compound waveguide ( $t$ ) with a thin luminophore film ( $t_0$ ), gives:

$$\eta_{RA} = \frac{\int_0^{\infty} d\lambda \int_{\theta_{crit}}^{\pi/2} d\theta \int_{-\pi/4}^{\pi/4} \sin(\theta) PL(\lambda) \left( 1 - \exp\left[-\varepsilon(\lambda)C \frac{Lt}{2t_0 \sin(\theta) \cos(\phi)}\right] \right) d\phi}{\int_0^{\infty} d\lambda \int_{\theta_{crit}}^{\pi/2} d\theta \int_{-\pi/4}^{\pi/4} \sin(\theta) PL(\lambda) d\phi} \quad (4.15)$$

The results of numerically integrating this equation as a function of luminophore parameters and LSC plate sizes are described in Chapter 5.

## Chapter 5

### UV-Absorbing Transparent Luminescent Solar Concentrators

#### 5.1 Introduction

Transparent luminescent solar concentrator can be enabled by selectively harvesting in different spectral ranges: in the UV or NIR. Despite the lower overall fraction of the solar spectrum in the UV (~6% photons, ~10% energy), there is significant potential in harvesting the UV in a transparent luminescent solar concentrator (TLSC) configuration up to 4% system energy conversion efficiency. In this chapter, we demonstrate a TLSC employing novel nanocluster-polymer blends that allow for selective ultraviolet light harvesting that results in a high degree of visible light transmittance demonstrating this pathway as a viable route to the production of transparent LSCs.

To efficiently capture and transform UV light around the visible spectrum, we focus on massive Stoke's shift (MSS) hexanuclear metal halide clusters of the form  $M_6(II)X_{12}$ . While the parent compounds of  $M = Mo$  and  $W$ , and  $X = Cl, Br, I$  etc. have been known for some time, their use has been limited to photophysical studies and oxygen sensors with quantum yields typically less than 20%.<sup>[95]</sup> These materials are highly stable, highly luminescent, US abundant, and non-toxic. Here, we have synthesized nanocluster complex-host blends with quantum yields  $> 75\%$  and anticipate reaching near-unity quantum yields through further chemical and ligand modifications. Luminophore-ligand-host pairing is shown to increase the solid-state quantum yields (over solution) through polar interactions, while also encapsulating the nanoclusters. We subsequently exploit the massive Stokes shift (~400nm), near-infrared emission, and perfect UV-VIS

absorption cutoff to 1) reduce nearly all reabsorption losses in the LSC configuration, 2) maintain a high degree of visible transparency and 3) eliminate visible glow. The TLSC demonstrated here based on inorganic nanocluster luminophores provides an alternative strategy for transparent solar harvesting systems over very large areas.

## 5.2 Experimental section

### 5.2.1 Nanocluster preparation

Metal(II) halide clusters were modified from the parent salt compounds through ligand exchange reactions. The parent cluster was synthesized through reduction of commercially available  $M(V)X_5$ , following previously outlined procedures<sup>[97-99]</sup> or purchased directly in the form of  $M(II)X_2$ . For Mo-based clusters, the parent compound was then purified by conversion to the HCl salt, which was returned to  $M_6(II)X_{12}$  via heat-treatment at  $> 200\text{ }^\circ\text{C}$  under vacuum. For  $K_2M_6X_{14}$ , a 5mg/mL solution of KCl in 6M HCl was added to a stirred solution of 2mg/mL of  $Mo_6Cl_{12}$  in 6M HCl at a volume ratio of 1:6. The resulting solution was concentrated by boiling in a hotplate with stirring in an inert atmosphere. The solution was slowly cooled below room temperature resulting in yellow needles. The TBA salt was prepared by adding tetrabutylammonium chloride to a solution of 2mg/mL of  $Mo_6Cl_{12}$  in 6M HCl which precipitated solid needles. Ligand exchange was carried out in a Soxhlet extractor with the parent compound for several days. Variations of M, X, and L in  $M_6X_{12}\cdot L_2$ ,  $A_2M_6X_{14}$  and  $A_2M_6X_{14}\cdot L_2$  including M = Mo and X = Cl, and L = Cl, H<sub>2</sub>O (hydrate), acetonitrile (ACN), and A = K, and tetrabutylammonium (TBA) were characterized, where ammonium salts can be readily anchored to polymer chain backbones. Solutions for optical

characterization were prepared by directly dissolving each compound in acetonitrile at various concentrations up to 4mg/ml.

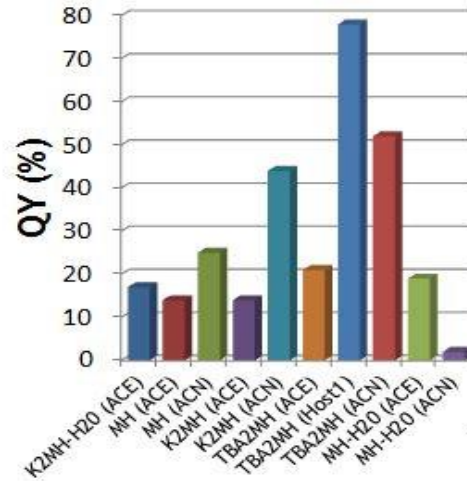


**Figure 5.1** Quantum yield of core material MH ( $\text{Mo}_6\text{Cl}_{12}$ ) with different cations (K,  $\text{H}_2\text{O}$ , TBA) in solvents acetone (ACE) or acetonitrile (ACN)

### 5.2.2 Module fabrication:

To fabricate modules, a 4mg/ml  $\text{A}_2\text{M}_6\text{X}_{14}$  acetonitrile solution was mixed with a 30mg/ml Poly-(ethyl methacrylate) (PEMA) acetonitrile solution (Sigma-Aldrich) and (poly)-butyl methacrylate-*co*-methyl methacrylate (PBMMA) (Sigma-Aldrich) at a volume ratio of 1:2:1, yielding the target dye concentration of 1mg/mL in the polymer composite film. This mixture was drop cast on 2.5cm x 2.5cm x 0.1cm substrates and allowed to dry for 2 hours for each layer under flowing nitrogen, and repeated 7 times, resulting in a layer thickness of approximately 200  $\mu\text{m}$ . On the mounted edge, a laser-cut, 2.5cm x 0.1cm Si cell (Narec Solar) with an efficiency of  $15 \pm 1\%$  @ 1 sun (see Figure 5.7) was attached using nearly-indexed matched epoxy. For the EQE measurements, the other

three edges were taped with black electrical tape to block edge reflection and simplify the geometric configuration. For the power efficiency measurements, two cells were edge-mounted on orthogonal edges and connected in parallel. The remaining two edges were covered with enhanced specular reflector (Vikuiti, 3M). A thin border area around the LSC edges was masked to avoid any direct illumination of the solar cell. Due to the illumination area of the solar simulator (67005 Xe arc lamp, Newport) plate lengths were limited to  $< 0.05\text{m}$ .

### 5.3 Results

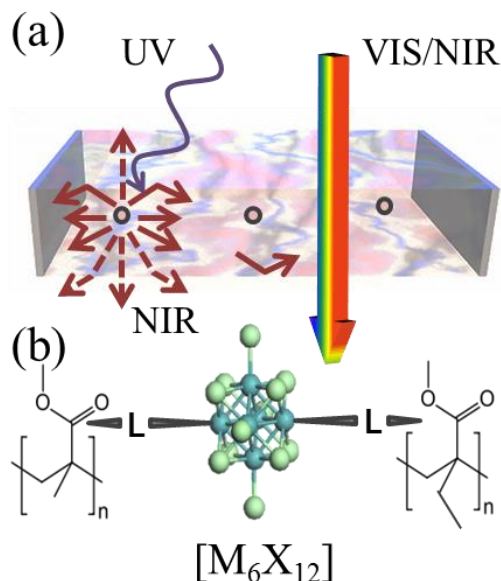


**Figure 5.2** (a) Schematic of the transparent luminescent solar concentrator and (b)  $M_6X_{12} \cdot L_2$  nanocluster-blend structure (dark green atom = M, light green atom = X); note that the salt compounds can be represented in (b) by replacing L with A-X or L-A-X.

Details of the hexanuclear nanocluster preparation are discussed in the Experimental section and the core cluster structure is shown in Figure 5.2(b). The absorption and emission spectra of the hexanuclear metal halide clusters are shown in Figure 5.3(a). The spectra show band absorption from 300-430nm with near perfect UV-VIS absorption

cutoff and broad near infrared (NIR) emission centered at 800nm that stems from highly efficient phosphorescent down conversion and emission. Nanocluster-ligand variations of  $M_6X_{12}$ ,  $M_6X_{12}\cdot L_2$  and  $A_2M_6X_{14}\cdot L_2$  exhibit nearly identical absorption-emission properties, where emission spectra can be tuned roughly 50-100nm with metal/halogen (M/X) substitution, and terminal cations/ligands (A/L) are found to primarily impact the overall non-radiative rates without impacting spectral shape.

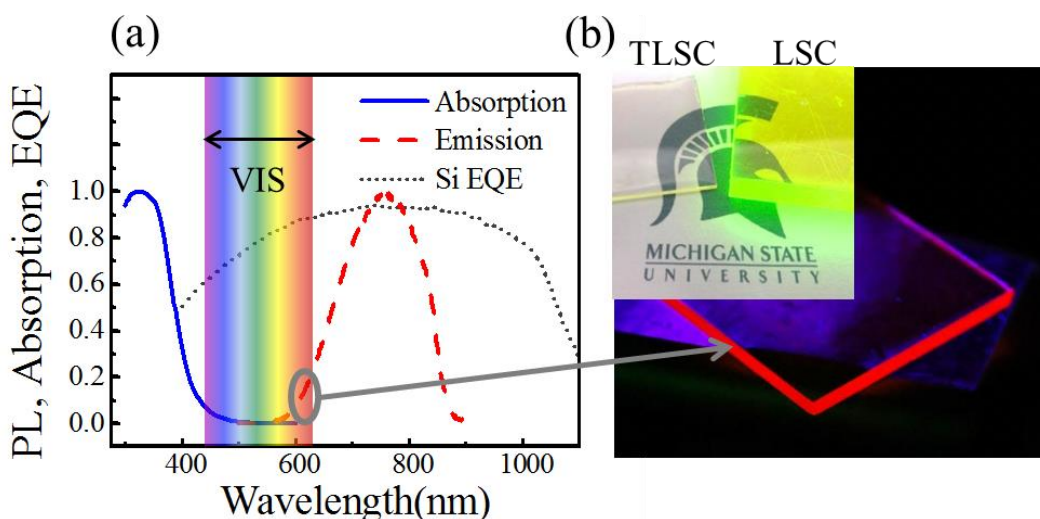


**Figure 5.3** (a) Normalized absorption (solid blue line) and emission (dotted red line) spectra of the UV absorbing luminophores overlaid with the measured EQE of the edge-mounted Si PVs (grey line). (b) Photograph of the LSC system incorporating the massive-Stokes shift UV nanoclusters under intense UV illumination where only the tail-end of red NIR emission can barely be seen except around the edge. Note that some blue/violet light can be seen through the LSC that originates from tail lamp emission in the range of 410-450nm. (inset) Comparison of the transparent luminescent concentrator (“TLSC“, left) with a typical semi-transparent solar concentrator (“LSC“, right) highlighting the need for both absorption and emission outside the visible spectrum.

To understand the photophysical behavior of these nanoclusters, we explore the luminescence quantum yield (QY) dependence on the concentration. The measured QY of hexanuclear metal halide clusters with different cations/ligands in both acetonitrile solutions and blended in (poly)-butyl methacrylate-*co*-methyl methacrylate (PBMMMA) /

(poly)-ethyl methacrylate (PEMA) solid-film composites are shown in Figure 4.3 as a function of nanocluster concentration for  $K_2Mo_6Cl_{14}$  and  $(TBA)_2Mo_6Cl_{14}$ . We fit the QY data of Figure 5.4 with the model:

$$QY = \frac{k_R}{k_R + k_{nR}} = \frac{k_R}{k_R + k_{nR0} + aC} = \frac{1}{1 + \frac{k_{nR0}}{k_R} + \frac{aC}{k_R}} \quad (5.3)$$

where  $k_R$  is the rate for luminescence (phosphorescence),  $k_{nR0}$  is the intrinsic non-radiative rate for isolated clusters,  $C$  is molar concentration, and  $a$  is concentration quenching scaling constant. For  $K_2Mo_6Cl_{14}$ ,  $k_{nR0}/k_R = 0.1$ ,  $a/k_R = 4.4\text{ml/mg}$ , while for  $(TBA)_2Mo_6Cl_{14}$   $k_{nR0}/k_R = 0.1$ ,  $a/k_R = 0.4\text{ml/mg}$ .

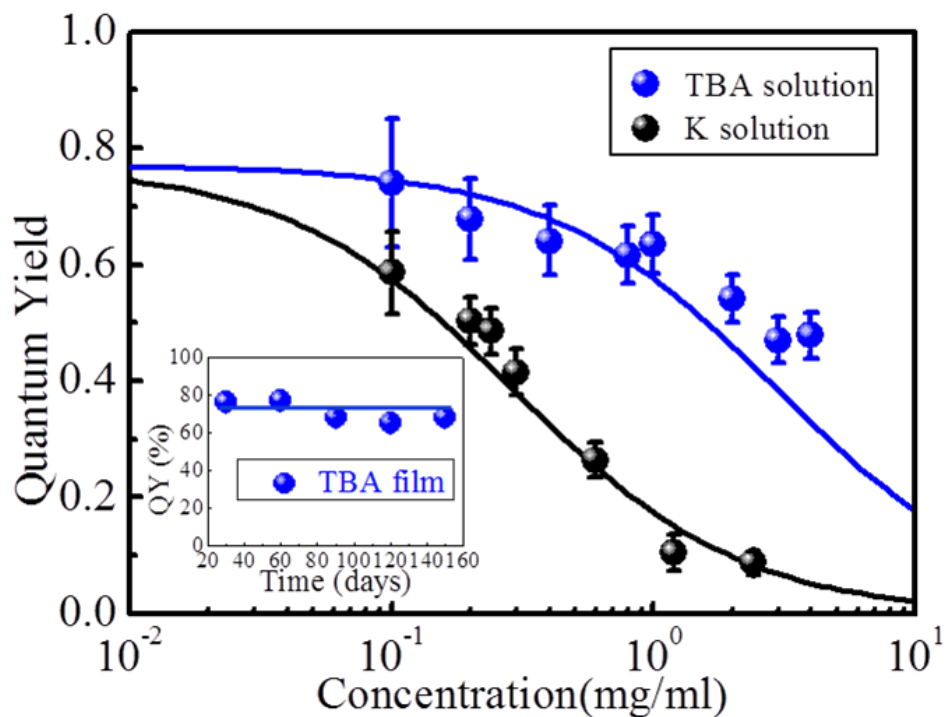


**Figure 5.4** Measured quantum yield (QY) of  $K_2Mo_6Cl_{14}$  and  $(TBA)_2Mo_6Cl_{14}$  in acetonitrile as a function of concentration; solid lines are fits to Equation. 1. (inset) QY of the TBA film as a function of time under shelf-life conditions.

Initial shelf-life testing also indicate that the inorganic phosphorescent luminophore-blends are highly stable as shown in Figure 5.4, and as has been indicated elsewhere for analogous cluster-host systems used in oxygen sensors.<sup>[98]</sup> In Figure 5.3(b) we show the assembled transparent LSC with a single-edge mounted Si solar cell incorporating the TBA luminophore where the measured EQE of the attached Si solar cell is shown in Figure 5.3 for reference.

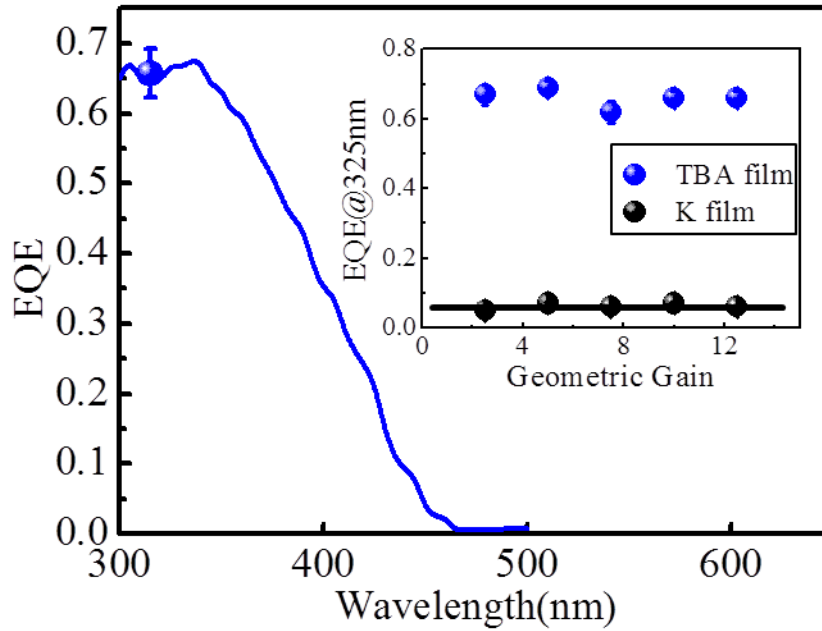


**Figure 5.5** External quantum efficiency (*EQE*) of the LSC system as a function of wavelength; (inset) measured *EQE* at 325nm as a function of geometric gain.

The spectrally resolved *EQE* of the overall LSC system is shown in Figure 5.5, which exhibits a cut-off at the edge of visible spectrum around 400-430nm, matching the absorption spectrum (see Figure 5.3(a)). The *EQE* at 325nm as a function of the geometric gain  $G$  (the ratio of the area of the concentrator and the attached solar cells) remains unchanged, within error.

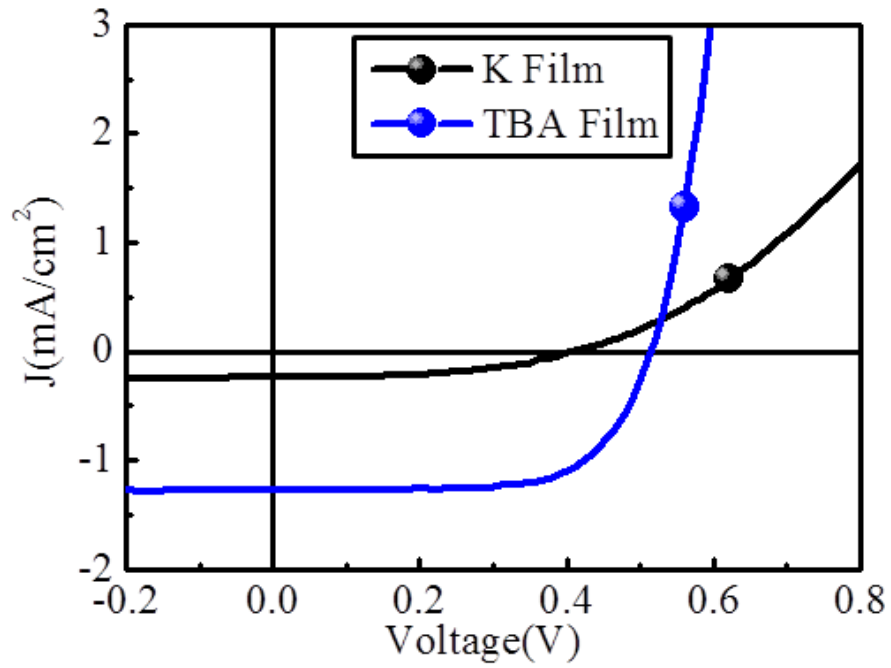


**Figure 5.6** Current density as a function of voltage for the fully assembled LSC systems with two of the luminophores.

Shown in Figure 5.6 is the current voltage characteristic of the 2.5cm x 2.5cm x 0.1cm LSC system for two edge mounted Si solar PVs (see Experimental section for details);

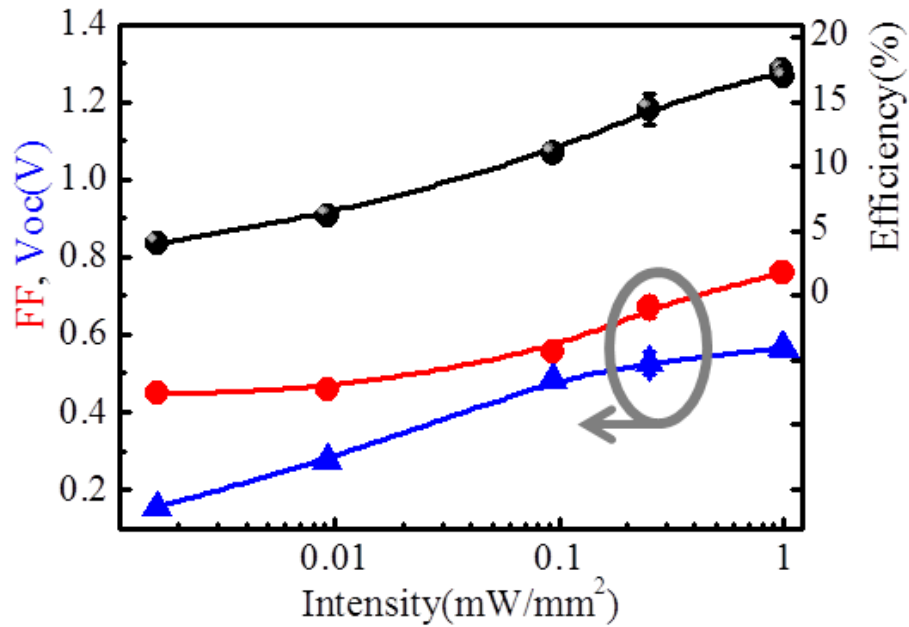


**Figure 5.7** Light intensity dependence of the  $V_{oc}$ ,  $FF$  and power efficiency of the Si cell.

the measured intensity dependence of the Si PVs is shown in Figure 5.7 and subsequently utilized in device-scaling modeling. The measured short circuit current density ( $J_{sc}$ ) of the overall system under  $1.0 \pm 0.1$  sun was  $1.3 \pm 0.1 \text{ mA/cm}^2$ , with an open circuit voltage ( $V_{oc}$ ) of  $0.52 \pm 0.01 \text{ V}$  and a fill factor of  $0.65 \pm 0.02$  leading to an efficiency  $0.44 \pm 0.05\%$  for the TBA luminophore. To confirm the measured photocurrent results, we integrate the product of the EQE and the AM1.5G solar spectrum resulting in a short circuit current density of  $1.5 \pm 0.1 \text{ mA/cm}^2$ . The corresponding average visible transmittance and color rendering index<sup>[83]</sup> for the LSC system is  $84\% \pm 1\%$  and 94, respectively, compared to  $90\% \pm 1\%$  and 100 for the glass substrate alone.

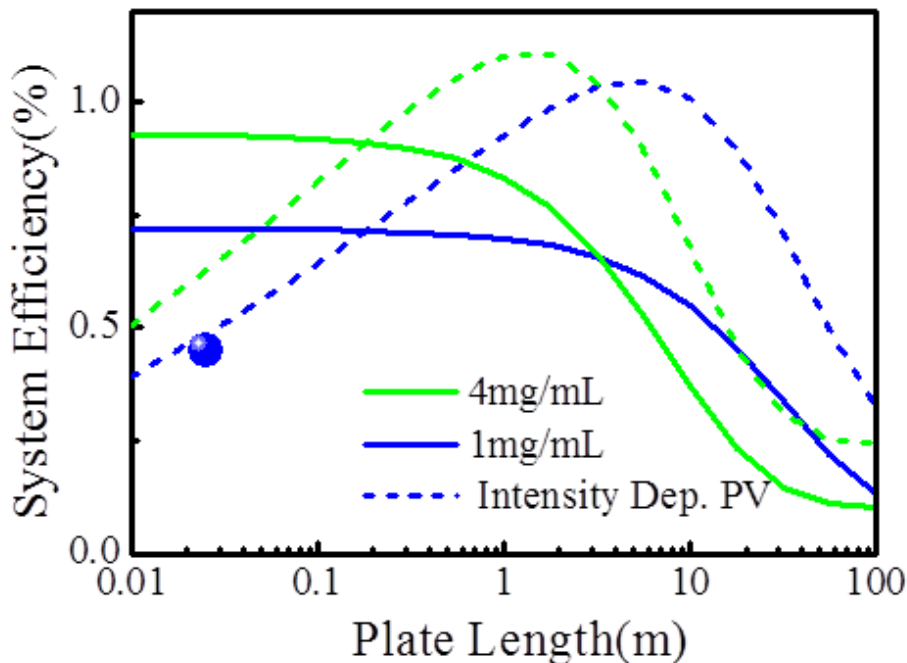


**Figure 5.8** Calculation of the overall LSC system efficiency as a function of plate size and luminophore concentration, without (solid lines) and with (dotted lines) the intensity dependence of the Si PV. Note that the solid lines are calculated using the 1-sun Si PV parameters and that the plate length of 0.2m roughly translates to a luminescence equivalent intensity of 1sun around the edges. The system efficiency is impacted by the luminophore concentration accounting for the solar absorption efficiency, reabsorption loss, and the quantum yield. Improving the quantum yield to 100% would result in a peak system efficiency of up to 1.3-1.5%.

In Figure 5.8 we show area-scaling calculations of the system efficiency as a function of square plate size. These simulations are, in part, validated by the EQE distance dependence shown in Figure 5.5. For the 2.5cm x 2.5cm x 0.1cm substrate, where  $G = 6$ , the light intensity that is absorbed by the Si cell is approximately equivalent in monochromatic intensity to 0.3 suns. In this case, the calculated efficiency is 0.5%, which is in good agreement to the measured value. For  $G > 250$ , the estimated efficiency of this TLSC system peaks at  $\sim 1.0\%$ . Due to the massive Stokes shift, the calculated LSC

performance remains high even for sheets as large as 1-10m<sup>2</sup>. Accounting for the intensity dependent Si PV performance, the efficiency is expected to increase slightly (with a constant optical efficiency) as the LSC size increases due to increased intensity concentration around the edges, while the optical efficiency starts to decrease for LSC sizes > 10 m<sup>2</sup> due to reabsorption losses.

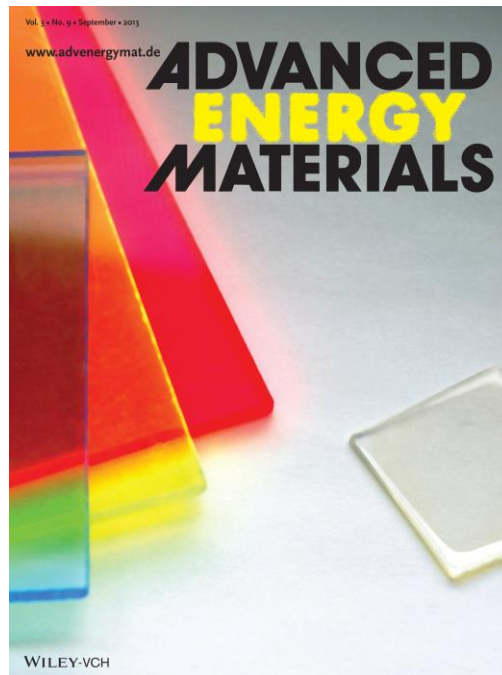


**Figure 5.9** Comparison of transparent UV-absorbing luminescent solar concentrators with traditional color LSCs.

## 5.4. Discussion

### 5.4.1 Nanocluster photophysics

The presence of a non-zero  $k_{nr0}$  from the fits in Figure 5.4 implies that individual nanoclusters have non-radiative modes that weakly compete with radiative rates. At higher concentrations, the quantum yield decreases with increasing concentration, suggesting that particle-particle interactions further lead to excited state (non-radiative)

quenching, common to many organic dye systems.<sup>[100]</sup> Therefore complete particle isolation is important to realize the full potential of these devices. The triplet excited state of organic compounds can also be efficiently deactivated by the presence of oxygen.<sup>[101-103]</sup> In our case, we tested the luminescent in absence of oxygen so quenching between luminophores is indeed the dominant mechanism. Accordingly, it becomes necessary to use thicker layers of lower concentration to maintain both high absorption efficiency and high quantum yield, following the Beer-Lambert law. Therefore, the balance between concentration and thickness on the overall absorption efficiency is linearly related and this relationship was utilized as a design criteria. For example, the critical concentration ( $C_C$ ) where the quantum yield starts to drop is  $C_C = 1.0\text{mg/mL}$  for the  $(\text{TBA})_2\text{Mo}_6\text{Cl}_{14}$  cluster in PBMA-PEMA blend, translating to a required blend thickness of  $200\ \mu\text{m}$  to maintain a high UV absorption efficiency.

In contrast to other luminescent systems, these are very high quantum yields for such large Stokes shift. Typical quantum yields (QY) for down-converting chromophores (with Stokes shift  $< 200\text{nm}$  and visible emission/absorption) now readily reach values approaching 100% for a variety of materials including organic phosphors, organic fluorophores, and colloidal quantum dots.<sup>[69, 104, 105]</sup> Up-converters or anti-Stokes materials still have notably low luminescent efficiencies  $< 5\%$ .<sup>[106]</sup> While a limited number of chromophores with massive Stokes shift have been demonstrated, the quantum yields of these materials have been notably limited at  $< 1\text{-}2\%$  or typically have emission centered in the visible part of the spectrum.<sup>[71, 107, 108]</sup>

## 5.4.2 LSC design

For the Si modules used here, the *monochromatic* efficiency translates to  $\eta_{PV}^* = 19\%$  under 1 sun equivalent illumination for the emission centered at 800nm. A range of other solar cells could be utilized to reduce additional thermal losses. For example, comparing the 1-sun solar cell parameters for several PV technologies,<sup>[109]</sup> we estimate the LSC system efficiency could be improved up to 1.3% with GaAs cell attached at the peak gain. Due to the monochromatic emission nature of the LSC, only single junction PVs can be considered around each individual LSC, limiting the overall system efficiency (without LSC stacking) to that below the Shockley-Queisser limit. However, cost and availability will ultimately drive the cell design. For example, GaAs cells could boost the efficiency for  $\eta_{LSC}$  over 30% compared to Si, particularly for the LSCs demonstrated here, but the estimated costs for these cells are more than double or triple that of Si.<sup>[109]</sup> Accordingly, we chose to couple lower-cost Si PVs with AM1.5G solar efficiency of 14-16% for our proof-of-principle demonstration, which can be further improved as cheaper, higher bandgap cells (GaAs, and GaInP) become available.

Re-absorption losses are critically dependent on the overlap of the emission and absorption spectrum and the overall dimension of the waveguide. It has long been recognized that LSCs are most limited by reabsorption losses, particularly for larger plate sizes. Indeed, much of the research with LSCs has focused on the reduction of these reabsorption losses through 1) increasing Stokes shifts with organic phosphors,<sup>[12]</sup> 2) multiple dye optimization to artificially increase the Stokes shift<sup>[12, 73, 110]</sup> or 3) resonance shifting limited to neat-film dye layers less than several microns thick.<sup>[111]</sup> The clearest

path to fully maximize the large-area scaling of these devices is through incorporation of high quantum-yield massive Stokes shift (MSS) luminophores.<sup>[68]</sup> With the use of the MSS luminophores developed here, there is essentially no overlap between the absorption and emission spectrum and therefore little reabsorption loss. Accordingly, these LSCs can be expanded to very large sizes ( $> 1\text{m} \times 1\text{m}$ ) provided the substrates are sufficiently transparent in the NIR.<sup>[71]</sup> This is highlighted in Figure 5.8, where at lower nanocluster concentrations the system (and optical) efficiencies only begin to drop off due to reabsorption losses for plate sizes  $> 10\text{m} \times 10\text{m}$ , which is larger than most typical windows. These results indicate a clear route to large-area TLSC scalability. Despite the low relative efficiency for these types of TLSCs (maximum efficiency of approximately 2%), the ability to maintain this efficiency to very large areas with high defect tolerances provides tremendous potential for window applications.

### **5.4.3 Understanding blend configuration via XPS**

There still remain questions about the precise nature of chemical interactions between luminophore and host that lead to quantum yield enhancements. X-ray Photoemission Spectroscopy (XPS) could be used to understand the nature of the chemical bonding that leads to enhanced/suppressed luminescence efficiency in these nanocluster and molecular systems. For example, we have already found that the nanocluster salts of tetra butyl ammonium coupled with particular hosts lead to enhanced QYs, where this could be due to polymer anchoring of the entire nanocluster salt to create better isolation or could act to detach the cation from the anionic nanocluster via anchoring of the cation. With XPS a narrow line width X-ray is used to probe a material's surface. By measuring the kinetic energy of photo-ejected core electrons the

atomic composition of the surface for all elements excluding H and He is determined. Because the sampling depth is limited to several monolayers on the surface, chemical information regarding the composition of a surface and how it may interact with various interfaces can be determined without the dilution by the bulk of a material as seen with many other forms of spectroscopy.

## 5.5 Conclusion

In conclusion, we have designed and fabricated novel transparent luminescent solar concentrators devices composed of phosphorescent metal halide nanoclusters with a power efficiency of  $0.44\% \pm 0.05\%$  (projected to reach  $1.0\%$  for  $G > 250$ ), system external quantum efficiency of  $60\%$ , and an average transmittance of  $84\% \pm 1\%$ , that are achieved through optimization of nanocluster-host interactions. The near perfect absorption cutoff at the edge of the visible spectrum ( $430\text{nm}$ ) and the massive Stokes shift to the near-infrared ( $800\text{nm}$ ) of these nanoclusters allows for efficient and selective harvesting of ultraviolet (UV) photons, improved reabsorption efficiency and non-tinted transparency in the visible spectrum. We show through both experiments and modeling that this architecture can exhibit a sustained power conversion of  $0.5\text{-}1.5\%$  over module areas  $> 1 \text{ m}^2$  with an upper efficiency limit of  $5\%$ . These novel concentrators present an entirely new paradigm for very large-area, non-tinted, and highly-adoptable solar windows that can translate into improved building efficiency, enhanced UV-barrier layers, and lower cost solar harvesting systems.

## Chapter 6

### NIR-absorbing Transparent Luminescent Solar Concentrators

#### 6.1 Introduction

In this chapter, we exploit the structured absorption of organic excitonic semiconductors to produce near-infrared (NIR) LSC architectures that selectively harvest NIR photons by waveguiding deeper-NIR luminophore emission to high efficiency segmented solar cells. These transparent NIR LSCs can eliminate the visual impact and minimize the amount of expensive solar materials required while extending the photon harvesting range into the NIR.

In the previous chapter, ultraviolet (UV) harvesting hexanuclear metal halide clusters with downconverted emission into the NIR were demonstrated for UV TLSCs.<sup>[72]</sup> The large phosphorescent Stokes shift and high quantum yield allowed for power conversion efficiency of  $> 0.5\%$  over large module area ( $\text{m}^2$ ) but these LSCs are ultimately limited to efficiencies up to 5% due to the limited UV fraction in the solar spectrum. To increase the overall potential of these systems, we look to selectively harvest NIR photons, where there is a substantially greater fraction of the solar photon flux ( $\sim 74\%$ ). NIR fluorescent dyes, especially phthalocyanines, cyanines, and squaraine dyes have been widely used in fluorescence microscopy, bioimaging, organic light emitting diodes and other light emission applications. However, the quantum efficiency has mostly been limited to  $< 40\%$  and most exhibit visible absorption.<sup>[112-116]</sup> Previous research on NIR-emitting LSCs employing inorganic compounds such as semiconducting quantum dots and nanocrystals as active materials typically have improved quantum yields<sup>[33, 41, 117-119]</sup> but also present

continuous band absorbance (with only minor excitonic features near the band edge). Accordingly, these systems all exhibit visible absorption or coloring despite emitting NIR.

In this chapter we demonstrate the first transparent NIR-absorbing luminescent solar concentrator with high transparency and minimal tinting. We focus on the development of luminophore blends of cyanine and cyanine salts and have synthesized cyanine salt-host blends with quantum yields of > 20%, combined with spectrally-selective NIR harvesting. We show the impact of Stokes shift on the ultimate performance and demonstrate transparent power conversion efficiencies > 0.8%. The near-infrared TLSCs based on organic salts provide an alternative strategy for transparent solar harvesting systems that can ultimately enhance the overall system efficiency of combined UV and NIR TLSCs.

## 6.2 Experimental section

### 6.2.1 Organic salt solution preparation:

1-(6-(2,5-dioxopyrrolidin-1-yloxy)-6-oxohexyl)-3,3-dimethyl-2-((E)-2-((E)-3-((E)-2-(1,3,3-trimethylindolin-2-ylidene)ethylidene)cyclohex-1-enyl)vinyl)-3H-indolium chloride (CY) (Lumiprobe) and 2-[7-(1,3-dihydro-1,3,3-trimethyl-2H-indol-2-ylidene)-1,3,5-heptatrienyl]-1,3,3-trimethyl-3H-indolium iodide (HITCI) (Exciton) were characterized as received without further purification. Solutions for optical characterization were prepared by directly dissolving each compound in dichloromethane at various concentrations up to 4mg/ml.

### 6.2.2 Module fabrication:

A 5mg/L CY dichloromethane solution was mixed with (poly)-butyl methacrylate-*co*-methyl methacrylate (PBMMMA) (Sigma-Aldrich) at a volume ratio of 1:1, yielding the target dye concentration (5mg/L) in the polymer composite film. This mixture was drop cast on 2cm x 2cm x 0.1cm (for efficiency measurements) or 7cm x 7cm x 0.1cm (for EQE measurements) glass substrates and allowed to dry for 2 hours for each layer, and repeated 3 times, resulting in a layer thickness of approximately 1mm. On the mounted edge, a laser-cut, 7cm x 0.1cm Si cell (Narec Solar) with an efficiency of  $15 \pm 1\%$  @ 1 sun was attached within a clip that fit around the edge of the waveguide and film.

### 6.2.3 Electronic structure calculations:

All DFT calculations, done in collaboration by the Levine group at MSU, were performed with the Q-Chem *ab initio* electronic structure package<sup>[120-122]</sup> while EOM-CCSD calculations were performed in GAMESS.<sup>[120, 121, 123-125]</sup> In order to assess the magnitude of the error in our CAM-B3LYP<sup>[126]</sup>/6-31G\* calculations of the vertical excitation energies of the cyanine dyes, a truncated model dye:  $(\text{CH}_3)_2\text{N}(\text{CH})_9\text{N}(\text{CH}_3)_2^+$  was evaluated. This dye contains the same 9-carbon polymethine chain terminated by tertiary amines as HITC<sup>+</sup> and CY<sup>+</sup>, but smaller dimethylamine groups replace the larger heterocycles to make more accurate quantum chemical calculations feasible. The vertical excitation energy of this model was calculated at the same TDDFT level of theory as applied to the larger dyes and with the more accurate equation-of-motion coupled cluster singles and doubles (EOM-CCSD) level of theory<sup>[127]</sup> with the cc-pVDZ basis set.<sup>[128]</sup> The computed vertical excitation energies at the TDDFT and EOM-CCSD levels of

theory are 3.09 and 2.40 eV, respectively. The difference, 0.69 eV, is subtracted from the TDDFT-computed vertical excitation energies of the larger dyes to estimate the more accurate EOM-CCSD excitation energies of these dyes. Note that the lowest excitation in the truncated cyanine has identical  $\pi \rightarrow \pi^*$  character to that predicted by TDDFT for the lowest excitations in HITC and CY.

### 6.3 Results

We focus on two promising cyanine derivatives: 2-[7-(1,3-dihydro-1,3,3-trimethyl-2H-indol-2-ylidene)-1,3,5-heptatrienyl]-1,3,3-trimethyl-3H-indolium (HITC) iodide (HITCI) and 1-(6-(2,5-dioxopyrrolidin-1-yloxy)-6-oxohexyl)-3,3-dimethyl-2-((E)-2-((E)-3-((E)-2-(1,3,3-trimethylindolin-2-ylidene)ethylidene)cyclohex-1-enyl)vinyl)-3H-indolium chloride (CY) and utilize these systems to explore the impact of the Stokes shift. The CY and HITCI molecular structures are shown in Figure 6.2. The absorption spectra peaks at  $742 \pm 1$  nm for CY and  $733 \pm 1$  nm for HITCI with little visible absorption, and NIR emission peaks at  $772 \pm 1$  nm and  $753 \pm 1$  nm for CY and HITCI, respectively. The Stokes shift, defined as the wavelength difference between the absorption and emission peaks, is  $30 \pm 2$  nm for CY and  $20 \pm 2$  nm for HITCI. The Stokes shift of the two materials helps demonstrate the difference in assembled LSCs performance and is also an important parameter to predict large-area scalability.<sup>[12]</sup>

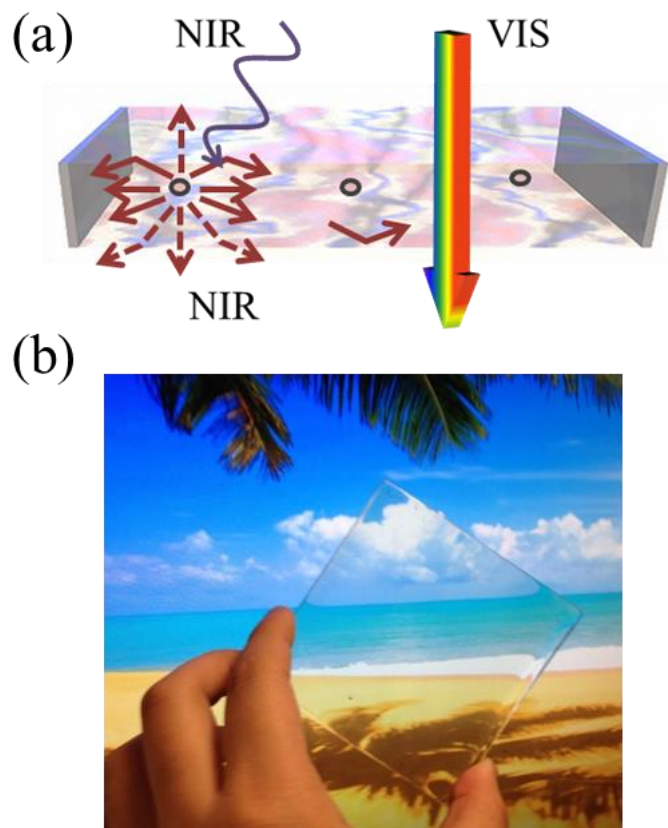


**Figure 6.1** (a) Schematic of the transparent luminescent solar concentrator (b) Photograph of the transparent LSC system incorporating CY luminophore in front of a picture of beach scenery.

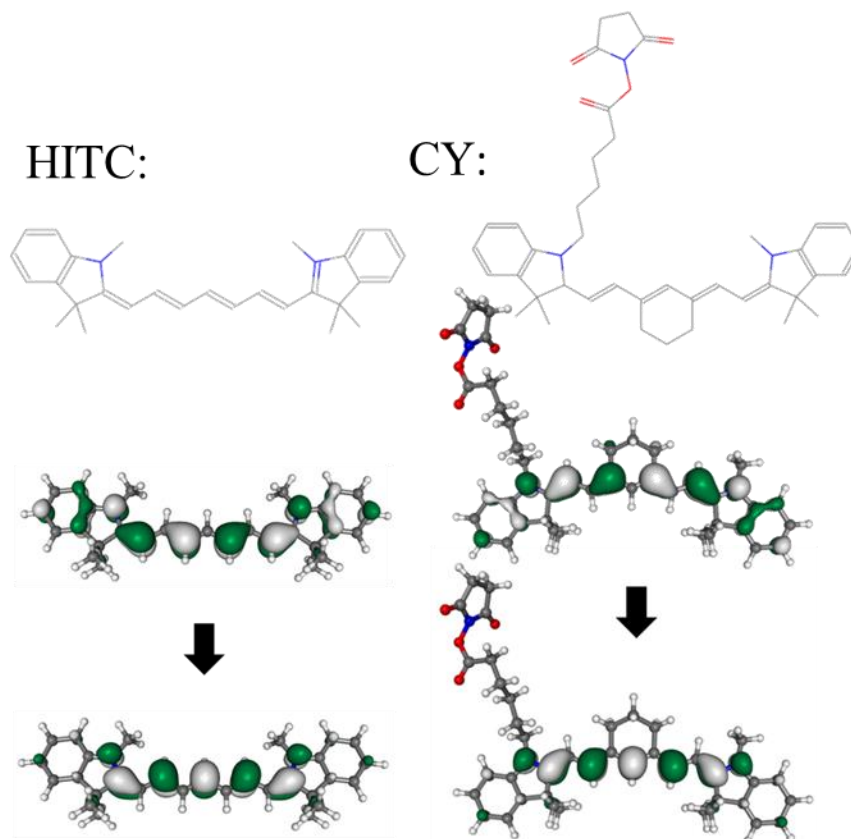


**Figure 6.2** CY and HITC molecular cation structures (top); the natural excited-state transition orbital pairs for HITC (left) and CY (right). The hole orbitals are shown on the top of the excited electron orbitals.

We explore the luminescence quantum yield (QY) dependence on the concentration to understand the photophysical behavior of these luminophores. The measured QY and absorption of CY and HITCI in dichloromethane solutions are shown in Figure 5.3(b) as a function of luminophore concentration.

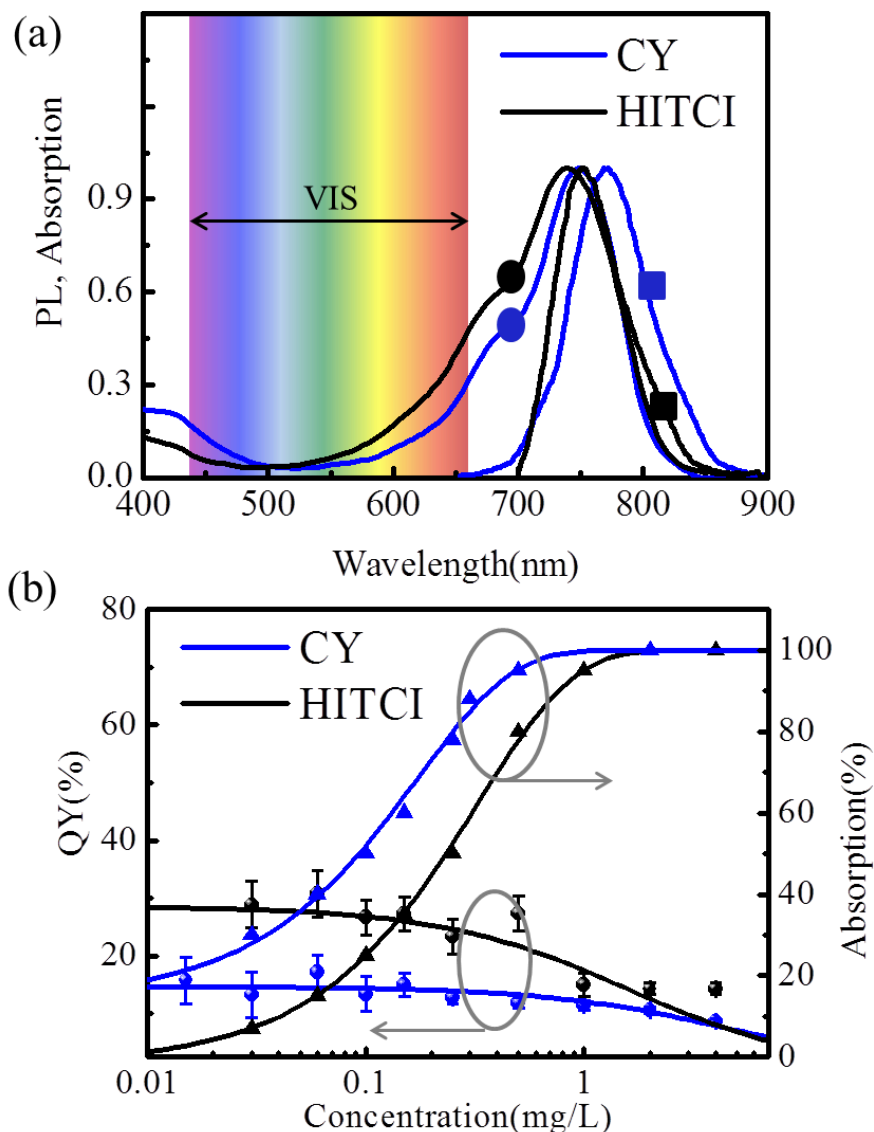


**Figure 6.3** (a) Normalized absorption (circle symbols) and emission (square symbols) spectra of the NIR-absorbing luminophores CY (blue line) and HITCI (black line) films. (b) Measured quantum yield (QY) and absorption of CY (blue line) and HITCI (black line) solutions in dichloromethane as a function of concentration; solid lines are fits to model for the QY<sup>[72]</sup> and the Beer-Lambert law for the absorption.

We fit the QY data of Figure 6.3(b) to a model with a concentration dependent non-radiative rate<sup>[72]</sup> and calculate the relationships between intrinsic non-radiative rate for

isolated clusters  $k_{nR0}$ , rate for luminescence  $k_R$ , and concentration quenching scaling constant  $\alpha$ .<sup>[72]</sup> For CY,  $k_{nR0}/k_R=5.8\pm0.2$ ,  $\alpha/k_R=1.4\pm0.1$  ml/mg, while for HITCI,  $k_{nR0}/k_R=2.5\pm0.2$ ,  $\alpha/k_R=2.2\pm0.1$  ml/mg. For both CY and HITCI, the non-radiative rate ( $k_{nR0}$ ) is much larger than the radiative rate ( $k_R$ ). The larger ratio  $\alpha/k_R$  for HITCI implies a slightly larger luminophore-luminophore interaction distance for HITCI; compared to the metal halide nanoclusters these concentration dependent terms are nearly an order of magnitude larger and thus require very dilute concentrations to suppress detrimental interactions.<sup>[72]</sup> The critical concentrations for CY and HITCI, defined here as the concentration where the QY is half of the maximum, are 5mg/L and 1mg/L, respectively. In Figure 6.1(b) we show the transparent LSC waveguide incorporating the CY luminophore. The measured intensity dependence of the assembled CY LSC is shown in Figure 6.4(a) which is largely dependent on the intensity dependence of the edge-mounted Si cells.

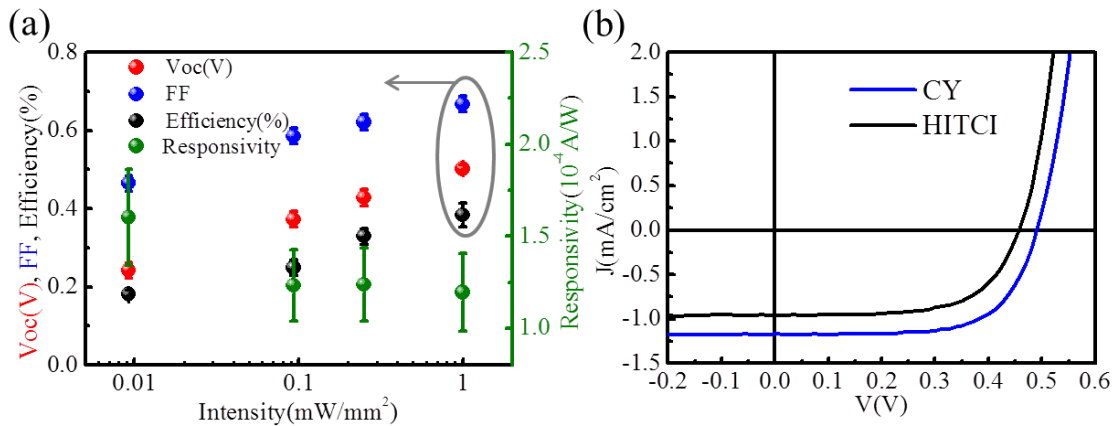


**Figure 6.4** (a) Light intensity dependence of the  $V_{oc}$ ,  $FF$ , power efficiency and responsivity of the CY TLSC device. (b) Current density as a function of voltage for the fully assembled TLSC systems with two of the luminophores.

The spectrally resolved external quantum efficiency (EQE) of the overall LSC system of different plate sizes are shown in Figure 6.5(a), which exhibit a peak at around 760 nm, matching the absorption spectrum and the calculated EQE in Figure 6.5(b).

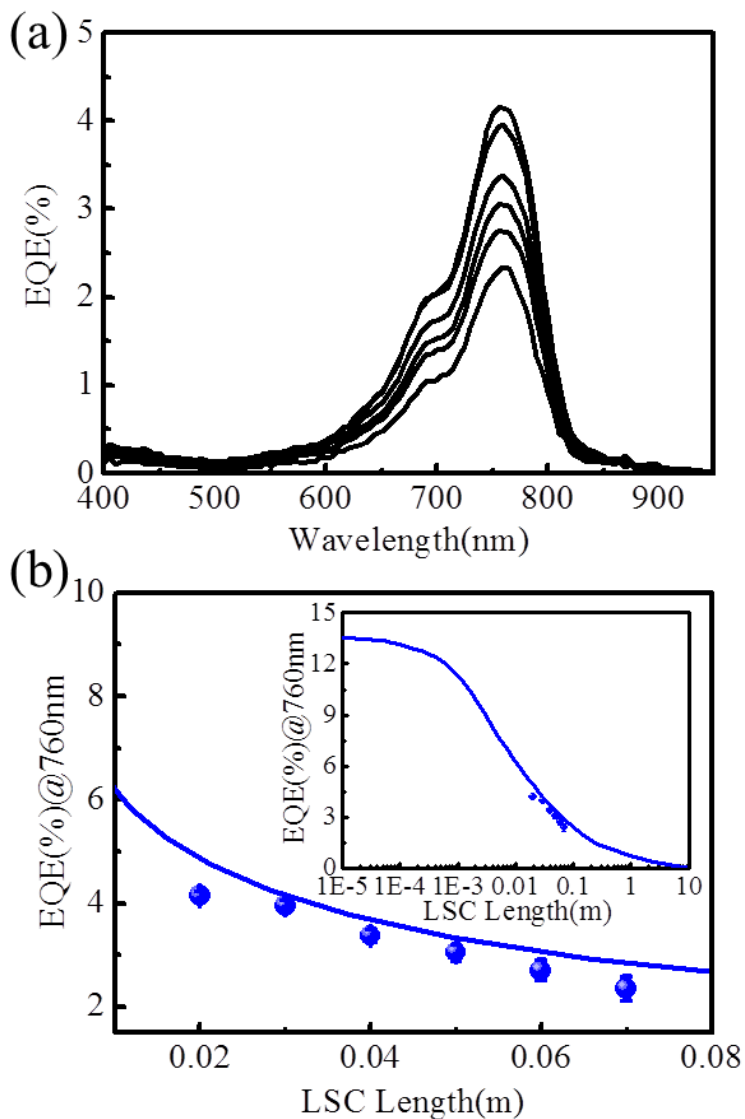


**Figure 6.5** (a) External quantum efficiency (EQE) of the CY TLSC system as a function of wavelength measured from 0.02m to 0.07m, with 1cm increments. (b) Calculated EQE as a function of CY LSC length in the range of 0.02m to 0.08m. Measured EQE (circle symbols) are also shown here. (inset) Calculated and measured EQE as a function of CY LSC length over a larger plate range.

Shown in Figure 6.4(b) are the current voltage characteristics of the 2cm  $\times$  2cm  $\times$  0.1cm CY and HITCI LSC systems for two edge mounted Si solar PVs (see Experimental section for details). The measured short circuit current density ( $J_{sc}$ ) of the overall system for CY under  $1.0 \pm 0.1$  sun was  $1.2 \pm 0.1 \text{ mAcm}^{-2}$ , with an open circuit voltage ( $V_{oc}$ ) of  $0.50 \pm 0.01 \text{ V}$  and a fill factor of  $0.66 \pm 0.02$  leading to an efficiency  $0.4 \pm 0.03\%$  for the CY luminophore. The calculated short circuit current density from integrating the product of the EQE and the AM1.5G solar spectrum, is  $1.0 \pm 0.1 \text{ mAcm}^{-2}$ , which is within error of the measured photocurrents. The corresponding average visible transmittance and color rendering index<sup>[83]</sup> for the CY LSC system is  $86\% \pm 1\%$  and 94, respectively, compared to  $90\% \pm 1\%$  and 100 for the glass substrate alone and is slightly better in aesthetic quality compared to the UV-only TLSCs.<sup>[72]</sup>

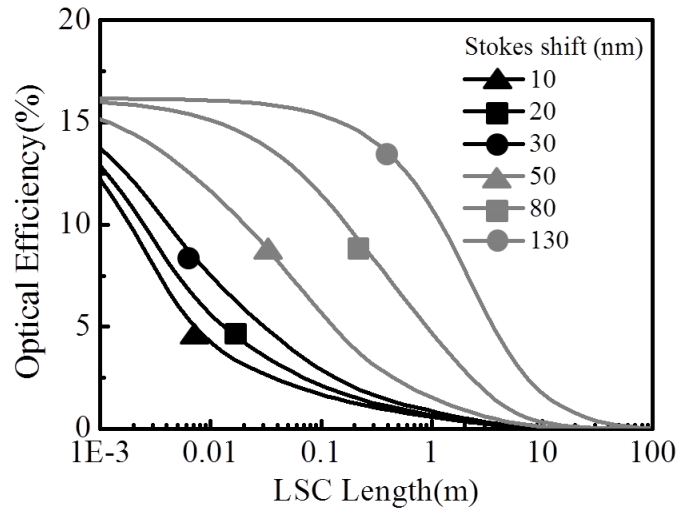


**Figure 6.6** Calculation of the CY TLSC optical efficiency as a function of LSC length with a function of simulated Stokes shift. Stokes shift are 10nm (black, triangle), 20nm (black, square), 30nm (black, sphere), 50nm (gray, triangle), 80nm (gray, square), 130nm (gray, sphere). For reference, CY and HITCI have Stokes shifts of 20nm, and 30nm, respectively.

In Figure 6.6 we show area-scaling calculations of optical efficiency of CY LSC with modeled Stokes shift as a function of LSC length. When the Stokes shift ( $S$ ) is below 30nm, the critical plate length, defined here as the LSC length where the optical efficiency is half of the maximum, is around 1-2 cm while increasing the  $S$  can significantly increase the critical plate length to  $> 1$  m for  $S > 100$  nm.

To explore the potential for modifying the two luminophores, the electronic structures of isolated HITC and CY molecular cations were optimized using density functional theory (DFT)<sup>[129]</sup> with the CAM-B3LYP functional<sup>[126]</sup> and 6-31G\* basis set. The excitation energies, oscillator strengths, and natural transition orbitals<sup>[130]</sup> were then calculated at the time-dependent (TD-) DFT level of theory<sup>[131, 132]</sup> in the Tamm-Dancoff approximation<sup>[133]</sup> using the same functional and basis set.

## 6.4. Discussion

### 6.4.1 Luminophore photophysics

The individual non-radiative rates for luminophore are larger than the radiative rates, leading to moderately-low quantum yields. This is true for many of the demonstrated NIR fluorophores and there continues to be significant effort to improve QY in this spectral range both for medical applications and light emitting diodes.<sup>[112, 113, 116]</sup> Here, the quantum yield decreases with increasing concentration due to excited state (non-radiative) quenching caused by particle-particle interactions at higher concentrations – these interactions persist even into dilute solutions likely through long-range dipole-dipole interactions such as Förster energy transfer due to the significant absorption-emission overlap. Accordingly, we design our concentrators using thicker layers of dilute concentrations to maintain both high quantum yield and high absorption efficiency,

following the Beer Lambert law. Utilizing this criterion we start with a design concentration of 5mg/L for high quantum yield as well as a reasonable thickness, a molar absorption coefficient of  $1.45 \times 10^8 \text{ Lmol}^{-1}\text{m}^{-1}$  for CY at 760nm, leading to blend thicknesses around 1mm for near complete NIR absorption. By utilizing thicker layers of dilute concentrations this also aids in reducing reabsorption losses discussed below.

#### **6.4.2 LSC design**

The efficiency of the transparent LSCs is governed by: the solar spectrum absorption efficiency, luminophore photoluminescence efficiency, waveguide (trapping) efficiency, transport (re-absorption) efficiency and solar cell quantum efficiency.<sup>[96]</sup> The optical efficiency consists of waveguiding efficiency, transport efficiency, and luminescence efficiency. The EQE consists of the optical efficiency and the quantum efficiency of the PV at the emission wavelength. Due to the monochromatic emission nature of the LSC, only single junction PVs can be attached around each individual LSC, which ultimately limits the overall system efficiency without LSC stacking to that below the PV efficiency directly. Reabsorption losses are critically dependent on the quantum yield of the luminophore, the Stokes shift of the dye emission-absorption, and the overall waveguide dimensions.<sup>[69]</sup> The reabsorption losses limit the performance of LSC fabricated in this work, due to the moderately low Stokes shift. For example, although HITCI exhibits a slightly higher quantum yield than CY, the CY device has enhanced LSC performance due to the larger Stoke shift. Indeed, it has long been recognized that LSC performance is often limited by reabsorption losses, particularly for dyes with modest  $S$  and larger plate sizes. The calculated optical efficiency in Figure 6.6 shows that an increase of Stokes shift from 30nm to 80nm can improve the critical length, from 3cm to 30cm, where an

LSC size of 30cm would be appropriate for many LSC applications. To fully maximize the large-area scaling of these devices, the design of high quantum yield molecules with a larger Stokes shift is favorable<sup>[68]</sup> such as with phosphorescent emitters.<sup>[12]</sup> However, when designing appropriate fluorescent and phosphorescent luminophores for NIR LSCs there is a balance in considering the ideal Stokes shift since we are limited to PVs that have high quantum efficiency at the luminophore emission peak, and also must consider maximizing the bandgap to minimize PV voltage losses. With Si PVs the maximum Stokes shift is limited to < 200nm with the expectation of harvesting a 200-300nm slice of the NIR spectrum. For GaAs this maximum  $S$  is even more restricted.

One approach to obtain better scalability is through the improvement of the quantum yield closer to 100% through optimization of luminophore-host interactions and molecular design. TDDFT shows that the lowest singlet transitions of HITC and CY are very bright, with oscillator strengths of 3.5 and 3.3, respectively. Natural transition orbital (NTO) analysis demonstrates that these bright excitations correspond to  $\pi \rightarrow \pi^*$  transitions localized on the polymethine chain of both dyes. NTOs corresponding to the dominant excitation amplitude (>0.95) for each dye are presented in Figure 6.2. The predicted vertical excitation energies for these transitions are 2.56 and 2.52 eV for HITC and CY, respectively; the overestimation of the excitation energies is not surprising given that the range-corrected functional used here is known to overestimate the vertical excitation energies of cyanine dyes.<sup>[134]</sup> To determine a correction to our TDDFT vertical excitation energies, the highly accurate equation-of-motion coupled cluster singles and doubles (EOM-CCSD) level of theory<sup>[127]</sup> was applied to a similar but truncated cyanine dye. Comparison to the TDDFT-computed excitation energy of the same truncated

system suggests that TDDFT overestimates the vertical excitation energies of these dyes by approximately 0.69 eV. Taking this as a correction to the TDDFT vertical excitation energies of HITC and CY yields energies of 1.87 and 1.83 eV, respectively, which are in much better agreement with experiment. Thus we are confident in the assignment of these NIR absorptions to polymethine-localized  $\pi \rightarrow \pi^*$  transitions. (See Experimental Section for details of these EOM-CCSD calculations.) These calculations help us to understand molecular motif targets to manipulate bandgap, oscillator strength, radiative rates and potentially improve QY.

Our present work and the past work of other groups both point toward rational principles for the design of NIR cyanine emitters with larger Stokes shifts, and thus promising candidates to decrease in reabsorption losses. Modified cyanine dyes which exhibit efficient fluorescence with Stokes shifts of  $\sim 100$  nm have been reported.<sup>[135, 136]</sup> These molecules, which emit from intramolecular charge transfer excited states, absorb in the visible range and thus are not useful in the present application. However, their existence demonstrates that the engineering of cyanines with intramolecular charge transfer states may allow us to achieve NIR emitters with large Stokes shifts through substitutions in the central methine group with bridgehead amine groups (that could be applied to the molecules here). Another strategy is suggested by the increased Stokes shift of CY compared to HITC. The side chain or the central methine group of CY must be responsible for this increase, given that these are the only differences between the two luminophores. Considering the flexibility of the side chain, we hypothesize that it may interact with the polymethine chain electrostatically, reorienting to stabilize the redistribution of charge upon excitation in the same way that a solvent molecule would

respond to excitation of a solvated dye. Increasing the number and/or polarity of these side chains as well as central methine substitution are two rational strategies to engineer visibly-transparent NIR luminophores with larger Stokes shifts, and can be pursued in future work.

For materials with QY close to 100% each reabsorption event leads to another emission event, reducing transport losses even for small  $S$ . However, it should be noted that for each absorption-remission event this appears as additional scattering since radiative emission is typically isotropic and therefore would eventually lead to greater front/back-side losses for larger plate lengths. Provided high quantum yields can be achieved, multiple cascaded luminophores could also be utilized to increase the effective Stokes shift.<sup>[12, 63]</sup>

Another important approach to improve the scalability for low Stokes shift materials, is to embed highly-segmented solar cell micro-arrays as meshes throughout the LSC waveguide to essentially create a series of “micro-LSCs”,<sup>[14, 137]</sup> allowing for minimal reabsorption losses and additional contribution from the segmented PV. Considering this last approach, and combining these demonstrated NIR LSCs with the UV-TLSCs, efficiencies >1% are readily achievable, and efficiencies approaching 10% are possible with enhancements in QY, Stokes shifts, and micro-LSCs.

Combining current UV and NIR LSCs in series enables LSC system with efficiency potential much above 1%. Such demonstration could allow us to realize the full efficiency, and large-area potential.

### 6.4.3 TLSC lifetime measurements

Degradation can occur in fluorescent molecules under certain conditions due to oxygen exposure, photobleaching, triplet reaction (necessarily coupled with O<sub>2</sub>), and host degradation. Many of these effects are readily overcome, however, through material encapsulation, purification, triplet scavenging (e.g. incorporation of cycloheptatriene, cyclooctatetraene, nitrones, etc.), and advantageous host pairings. Indeed, LSC dye lifetimes incorporating small molecules have already been demonstrated with > 10 year lifetime with projections of > 20 year lifetime. Nonetheless, this is a critical parameter that must be characterized and each host, dye, and host-dye combination by monitoring absorbance and edge luminescence as a function of solar illumination, humidity, temperature and oxygen exposure should be screened.

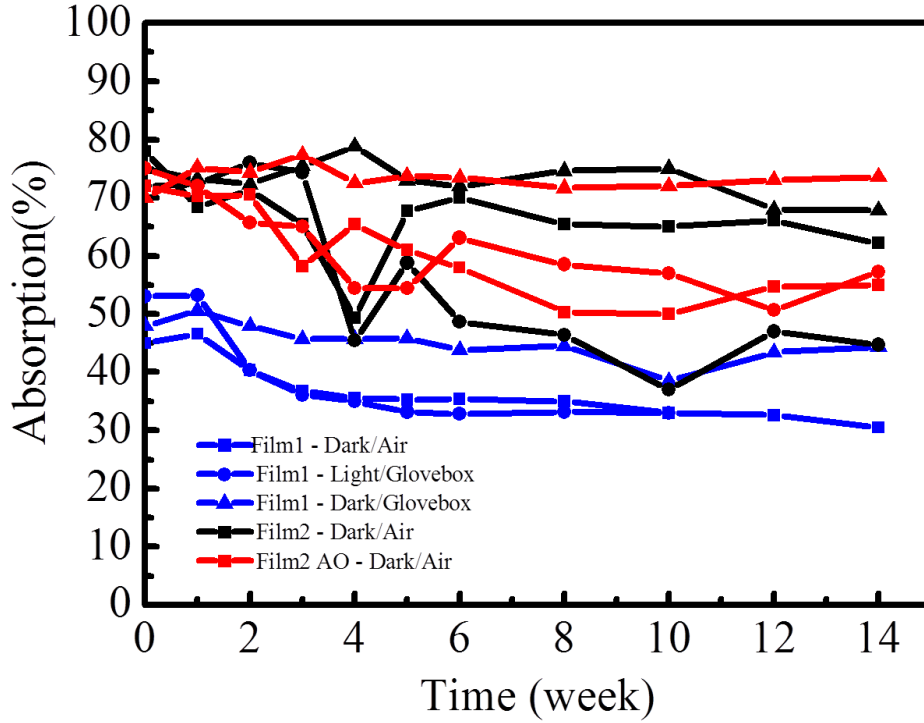


**Figure 6.7** Lifetime test: absorption of CY7 acid films under different conditions as a function of time. Film 1 is CY7 acid PMMA film and Film 2 is CY7 acid fluoroshield film. ‘AO’ refers to the addition of an antioxidant DACBO (1,4-Diazabicyclo[2.2.2]octane)

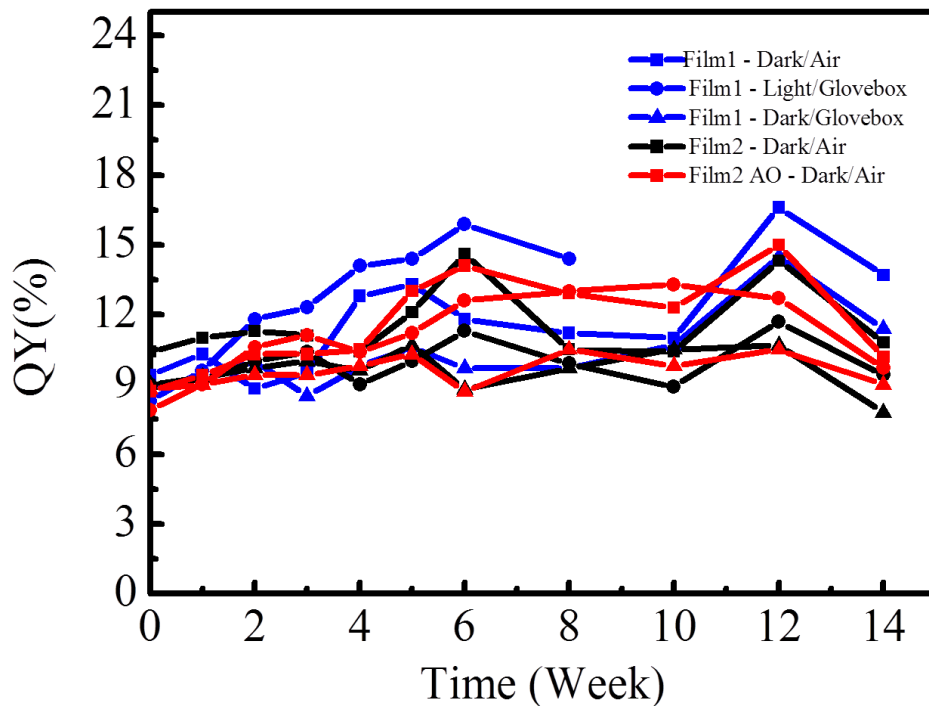


**Figure 6.8** Lifetime test: quantum yield of CY7 acid film under different conditions as a function of time. Films are same as shown in figure 6.7.

Preliminary lifetime tests show that transparent luminescent solar concentrators can keep high-level performance in long time (weeks to years). UV absorbing TLSCs can be kept at least 1 year while NIR TLSCs can be kept around months, if kept in dark in the room. Oxygen is detrimental for TLSCs lifetime while capsulation can help reduce the impact. Some lifetime test results are shown in Figure 6.7 and 6.8.

### 6.5 Demo

To demonstrate the potential of these TLSCs we fabricated modules with a plate length typical for a mobile electronic device that was capable of power small electronic devices. Glass substrates with a thickness of 0.5cm were sequentially cleaned with soap, deionized water, and acetone for 5 min in a sonicating bath. Substrates were then rinsed

in boiling isopropanol for 5 min and oxygen plasma treated for 30s. Luminophore-host mixtures were drop-cast onto the surface of the substrate and allowed to fully dry over 12 hrs. Then the sample was encapsulated with a second piece of glass.

The edge of the glass was cleaned by Solar Flux pen for solar panel (Kester 186). The PV was then glued using index-matching epoxy (AMS Technology). The demo was stored in an air and light free environment during the all the drying processes, but once encapsulated were safe to bring into air.

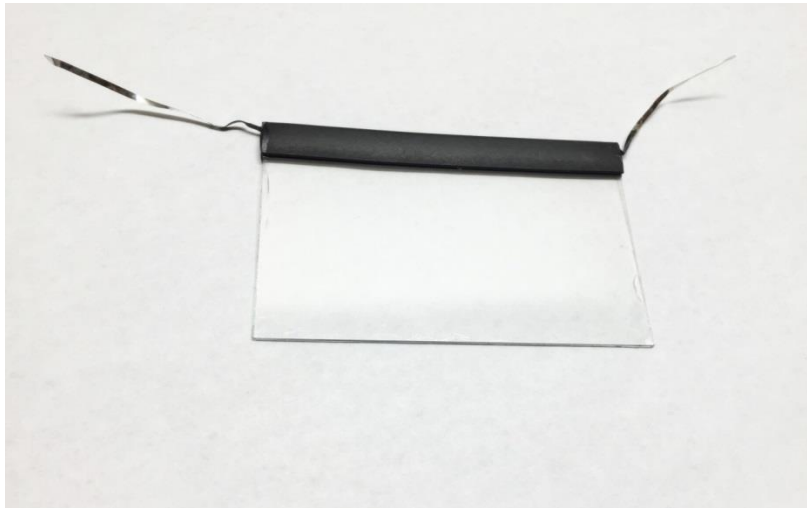


**Figure 6.9** Photograph of a NIR-absorbing TLSC demo.

## **6.6 Flexible transparent LSCs**

In addition to LSC devices developed directly on glass above, we have demonstrated flexible LSC architectures that can enable retrofittable integration. This is a key demonstration as it can open up many markets and applications.<sup>[14]</sup> We have already identified nearly ideal flexible substrate waveguide/hosts (see Figure 6.10) that can be coated with luminophore films or directly embedded with the luminophores through

extrusion techniques. Additionally, we identified and integrated high efficiency flexible thin film GaAs cells (24.5% 1-sun efficiency) to make these systems high performance and complete flexibility. One flexible GaAs cell is attached at the bottom of the waveguide with index-matching epoxy. The measured energy conversion efficiency reaches 0.8%, nearly double that of our previous glass/Si TLSC devices.

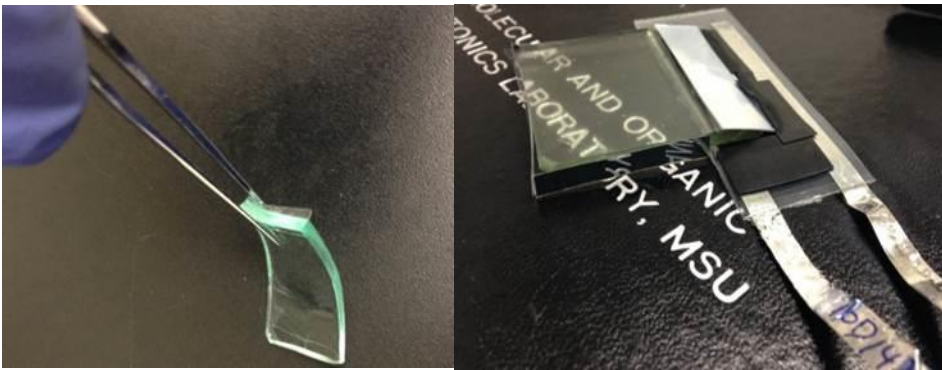


**Figure 6.10** Flexible transparent luminescent solar concentrators on flexible plastic substrates.

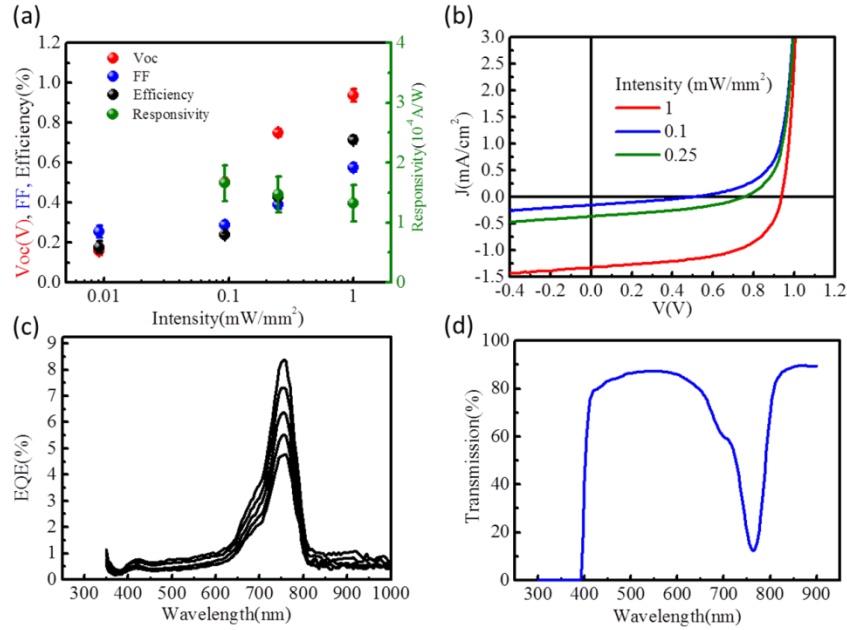


**Figure 6.11** (a) Performance metrics ( $V_{oc}$ , FF, efficiency and responsivity) of the TLSC system as a function of illumination intensity. (b)  $J$ - $V$  curve of the sample at different incident intensities. (c) EQE as a function of wavelength measured at distance of 5, 10, 15, 20, 25 mm from the GaAs cell. (d) Transmission of the overall system.

The measured energy conversion efficiency and EQE (external quantum yield) of the flexible TLSCs are shown in Figure 6.11 as a function of illumination intensity with the flexible GaAs cells (2 edge mounted cells). Note that the GaAs cells provide two distinct benefits: 1) higher voltage and overall efficiency (24% compared to 15% under 1 sun), and 2) greater mechanical flexibility over Si cells. The measured short circuit current density ( $J_{sc}$ ) of the overall system under  $1.0 \pm 0.1$  sun was  $1.3 \pm 0.1 \text{ mA}/\text{cm}^2$ , with an open circuit voltage ( $V_{oc}$ ) of  $0.93 \pm 0.03 \text{ V}$  and a fill factor of  $0.57 \pm 0.02$  leading to an efficiency of  $0.70 \pm 0.02\%$ . The peak EQE at 760nm can reach 8%, which is double that of the NIR TLSC we previously developed. The corresponding average visible transmittance and color rendering index for the TLSC system is  $86 \pm 1\%$  and 95, respectively.

## 6.7 Conclusion

We have designed and fabricated the first visibly-transparent luminescent solar concentrator devices which selectively harvest NIR photons based on fluorescent organic salts. These transparent TLSCs exhibit a non-tinted transparency of  $84\% \pm 1\%$  in the visible spectrum combined with an efficiency of  $0.8\% \pm 0.01\%$  and have the potential for efficiencies up to 10% due to the large fraction of photon flux in the near-infrared. We show through both experiments and modeling that the development of larger Stokes shift luminophores, optimization of luminophore-host interactions and fabrication of embedded segmented-PV configurations could further reduce reabsorption losses and increase the system efficiency over large areas. These transparent NIR LSCs provide a new route to transparent light-harvesting systems with tremendous potential for high defect tolerances and processability.

## Chapter 7

### Transparent Luminescent Solar Concentrators Cost

One of the advantages with transparent luminescent solar concentrators is the low cost compared with traditional expensive solar cells. In this chapter, calculations of manufacturing and module cost for TLSC systems are described and used to estimate the large scale potential for both types of TLSCs.

The evaluation of LSC system efficiencies for two of the representative LSC materials (UV Phosphor and NIR Luminophore) are shown in Figure 7.1 and 7.2. The impact of the massive Stokes shift is highlighted in the optical efficiency for the UV and NIR scaling. At moderate phosphor loading, the UV LSC can retain efficiencies beyond 10m, which is larger than most typical windows. In contrast for the NIR emitters (in the absence of enhanced Stokes shifts described in chapter 6), the efficiency begins to “roll-off” at only 1-10 cm, defining the ideal embedded solar cell spacing.

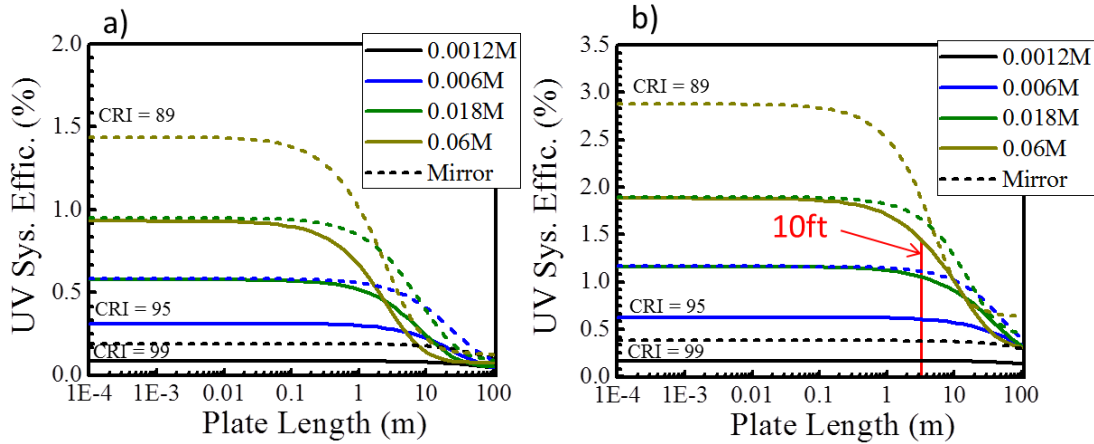


**Figure 7.1** Overall calculated LSC system efficiency for the UV only concentrator utilizing the spectral properties of Fig. 4, Si PVs, low-iron substrate with index 1.7, and quantum yields of a) 40% and b) 80% as a function of luminophore concentration embedded in a 5 mm thin host. Due to the massive Stoke shifts, the LSC performance remains high even for sheets as large as 10ft.

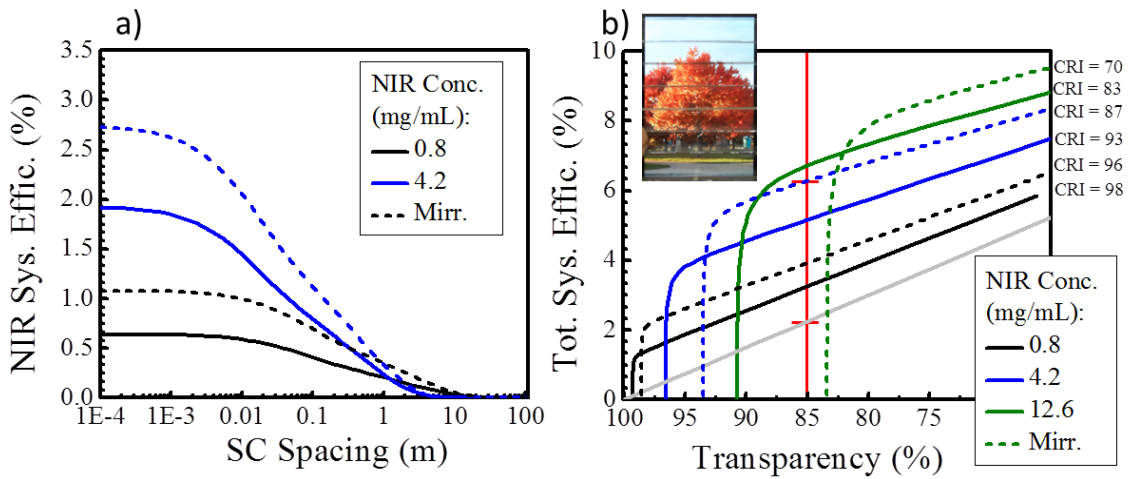


**Figure 7.2** Overall calculated LSC system efficiency for a) the NIR-only concentrator, and b) combined with spatially segmented 50 $\mu$ m Si solar cells utilizing the spectral properties, low-iron substrate with index 1.7, and quantum yields of a) 40% and b) 80% as a function of luminophore concentration embedded in a 50 $\mu$ m thin host. Note that with the transparent NIR luminophore embedded in the segmented PVs, the overall system efficiency can be more than triple that of the segmented PVs alone (grey line) for the same level of transparency and only utilizing a sliver of the NIR (675-800nm).

## 7.1 TLSC manufacturing cost

The manufacturing of LSCs reduces the number of coatings to one, resulting in highly simplified processing analogous to car-paint coating, with a final additional labor step required to assemble the solar cells around the LSC edge or within the LSC. We estimate the materials costs with small-scale commercial prices for reagents from commercial sources (Sigma, Dow, etc.), scaled by one-third to account for potential bulk material price reductions for both the luminophores and host chemicals. For labor and capital costs we assume similar practices to other thin-film coating technology estimates (e.g. CdTe and OPV) adjusted for the number of processing steps: LSCs for example have approximately 1/6 the steps required, therefore requiring lower capital to that of OPV (estimated at \$3.30/m<sup>2</sup>).<sup>[138]</sup> Hence a reasonable estimate for the capital cost is \$0.55/m<sup>2</sup>, which is in accord with the upper limit estimate of a capital investment of roughly \$50M for a typical new 10,000,000m<sup>2</sup>/yr low-e sputtering coating facility, which translates to \$5/m<sup>2</sup>. The direct labor costs are assumed to be for a semi-autonomous factory with three shifts per day (3 operators/shift) at 8hr/shift, and a wage rate of \$15/hr and an average yearly output of 0.5km<sup>2</sup> translates to \$0.84/m<sup>2</sup>. This is likely a conservative estimate, as compared to the magnitude estimates for thin-film production of 0.73-10 \$/m<sup>2</sup>.<sup>[66, 138]</sup> Here we assume that our production will be directly integrated (in-line) with existing glass-manufacturing facilities so that facility costs (rent, etc.) are negligible. Because of the room-temperature and low utility needs of the LSC fabrication, the utility costs estimated here (\$0.36/m<sup>2</sup>) are roughly 1/6 the cost for other vacuum-based production (\$2.18/m<sup>2</sup>). The final manufacturing cost (excluding materials) of \$2/m<sup>2</sup> is comparable to our estimate for automotive spray coating of \$3.49/m<sup>2</sup> (excluding paint costs). A

summary of the upper/lower manufacturing cost estimate for the LSCs is provided in Table 2.1. For comparison, the cost of typical BF33 (Schott) glass and low-iron glass (Saint Gobain - Diamant, Planilux) range from \$22/m<sup>2</sup> and 83/m<sup>2</sup>, respectively.<sup>[139]</sup> Because the LSCs designed here will be fabricated on glass that is already being installed as windows, this cost can be neglected in analyzing the incremental cost for transforming these surfaces into power producing surfaces, thereby eliminating the dominate cost for these systems (see Table 6.3).

Component	Cost (\$/m <sup>2</sup> )			
	UV		NIR	
	low	high	low	high
Capital Equip.	0.55	5.00	1.10	10.00
Labor	0.73	6.00	2.92	10.00
Facilities	0.00	3.63	0.00	3.63
Utilities	0.36	4.35	0.36	4.35
Maintenance	0.04	1.25	0.04	1.25
Warranty	0.35	2.11	0.35	2.11
Total	2.04	22.34	4.78	31.34

Material Costs		
UV dye	1.5	\$/gm
NIR dye	50	\$/gm
Host	0.2	\$/mL
Tabbing	0.5	\$/m
Epoxy	0.5	\$/m
Si PV	375	\$/m <sup>2</sup>
Glass	22-83	\$/m <sup>2</sup>
Framing	400	\$/m <sup>2</sup>

**Table 7.1** Estimated manufacturing (left) and materials costs (right) for the transparent LSCs by an inline coating process, integrated with a low e-coating facility. The glass and framing cost are included for reference

## 7.2 TLSC module cost

The cost of LSC systems strongly depends on the overall performance and system scale. The module cost, in \$/WP, can be estimated as:

$$\frac{\$}{W_p} = \frac{((\$ / gm)C_{dye} + (\$ / mL)t + (\$ / m^2)_{cap}}{\eta_{LSC}\eta_{orient}P_0} + \left(\frac{\$}{W_p}\right)_{PV} \frac{\eta_{LSC}\eta_{orient}}{\eta_{PV}} \frac{4t_0}{L} \quad (7.1)$$

where  $\eta_{LSC}$  is the overall system efficiency,  $P_0$  is the average solar power density accounting for the orientation dependent loss,  $\eta_{orient}$ ,  $PV$  is the 1-sun solar cell efficiency,  $G = L / 4t_0$  is the geometric gain, and  $L$  is the plate length. This model is an estimate for the modular cost of adding solar harvesting functionality to the window that is to be installed, not including BOS costs. The breakdown of the BOS systems can widely vary, but typically run in the range of \$1-2/WP with an approximate breakdown for a rooftop installation of \$1.0/WP Racking and Prep., \$0.3/WP Inverter, \$0.1-0.3/WP Installation, and \$0.2/WP Wiring and Transformer. <sup>[138]</sup> Since as much as 1/2 of the BOS cost can be for installation-framing-land, it is expected the effective BOS costs could be less than half of that for systems integrated elsewhere. That is, under certain plate dimensions and configurations, the module cost can be well under \$1/WP with an overall installed \$/WP with BOS to be < \$1/WP. The resulting module costs are shown in Figure 7.3 for both the UV and NIR focused LSCs. Importantly, the lowest cost/power (\$/WP) systems are the ones with the lowest optical losses (larger Stoke shift material, moderate concentrations), not necessarily the outright highest efficiency configurations. Both the optical performance and cost analysis highlight the extreme benefit of the massive Stoke-shift materials being developed. Despite the limited solar flux in the UV the module cost in \$/WP clearly can reach values approaching \$0.25/ WP (at the highest performance metrics), indicating the levelized energy cost would be primarily dictated by the remaining balance of systems costs. This indicates the payback period for adding such functionality would be minimal, particularly since the incremental cost in \$/m<sup>2</sup> could be lower than ubiquitous multilayer low-e coatings. Given a total LSC system cost of \$5/m<sup>2</sup> and a system efficiency of 1%, the payback time is around 3 yrs if electricity cost is fixed

at \$0.1/kW-hr. Despite lower overall system potentials, the low-cost potential makes these UV concentrators an excellent stepping stone for initiating the solar window market with high aesthetic-quality on route to implementation of higher efficiency UV and NIR LSCs.

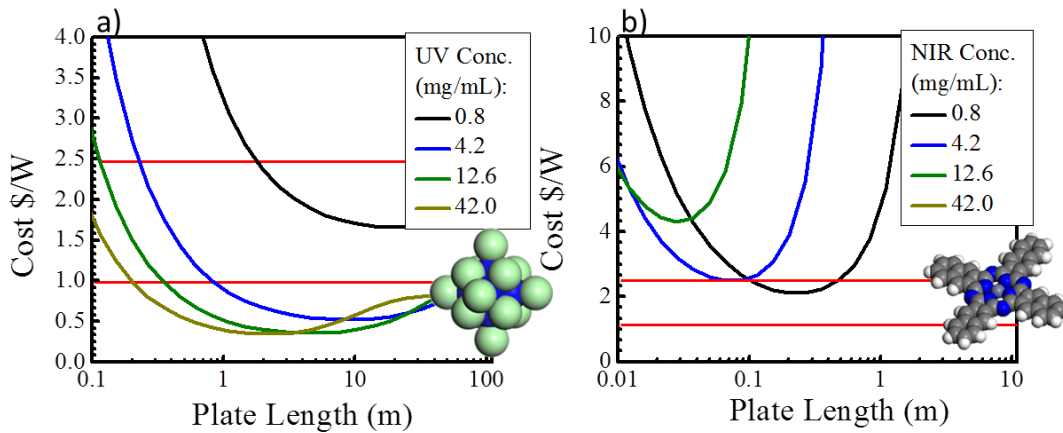


**Figure 7.3** Projection for the module cost in \$/WP of fabricating transparent LSCs on window surfaces a), b) for the UV luminophore and c), d) for the NIR CY luminophore using their respective spectral properties. Estimates are for a substrate index of  $n = 1.7$ , a commercially-available Si PV module efficiency of 18% under AM1.5G, and quantum yields of a), c) 0.4 and b), d) 0.8 and modest Stokes shift  $< 50\text{nm}$ .

## Chapter 8

### Conclusions and Future Outlook

#### 8.1 Future outlook

The aim of this work was to demonstrate transparent luminescent solar concentrators as a new pathway for widespread window deployment that can be scaled to commercial window products. Such a technology has the benefit of facile production, high defect tolerances, and exceptional scalability without many of drawbacks of scaling a transparent PV technology (resistive losses, partial shading losses, device yield, current matching, etc.). While the work presented so far has opened up an exciting new field and has demonstrated a key starting point for these new types of devices, there are a number of opportunities yet to be explored including:

##### 8.1.1. Singlet fission hosts for UV TLSCs

Singlet fission is a process that singlet excited state converts to two triplet states. The goal here is to find a singlet fission host material, capable of producing two triplets for one high energy singlet, and demonstrate energy transfer coupling to nanocluster emitters (Figure 8.1).

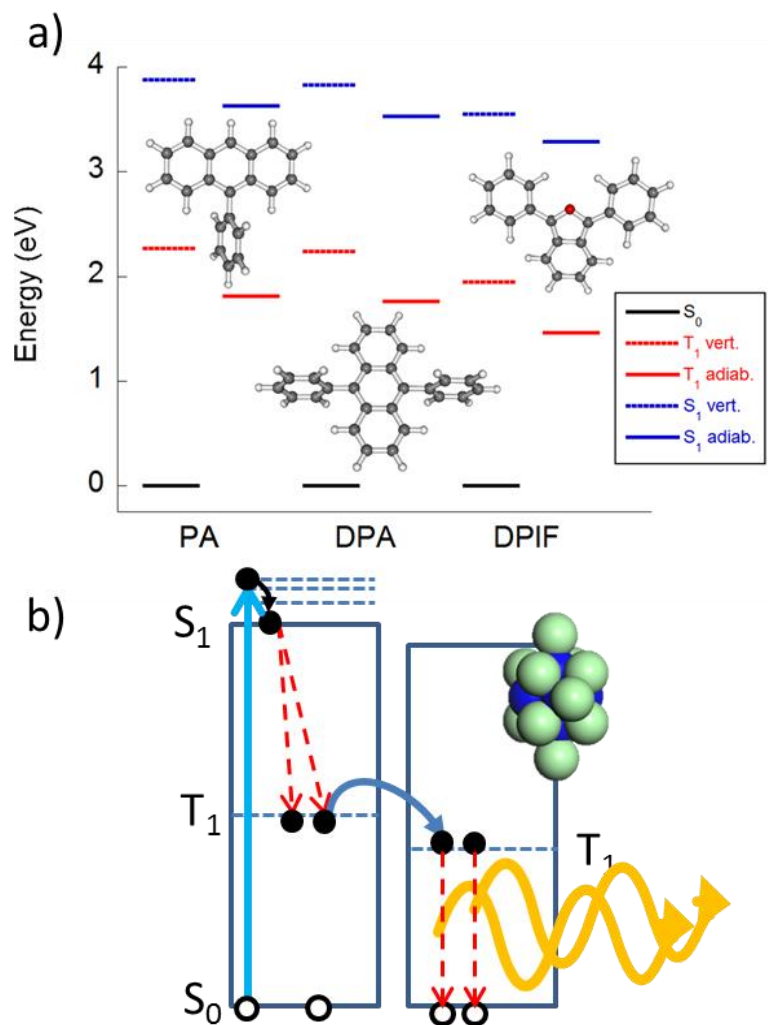


**Figure 8.1** (a) Vertical excitation energies of the lowest singlet ( $S_1$ ) and triplet ( $T_1$ ) excited states of three candidates for singlet fission. (b) Schematic of the singlet fission-energy transfer process

This would reduce the amount of required cluster and increase the limiting efficiency of the overall system by a factor of two by minimizing thermal losses in the Stoke shift from the UV to the NIR. The singlet fission material acts as both the “host” and absorber and the nanocluster acts as the phosphorescent emitter, rather than the primary absorber. Candidates for single fission hosts, including 9,10-diphenylanthracene, anthracene, diphenylisobenzofuran, phenanthrene, etc., should be characterized for singlet fission

yield and cluster coupling with the use of PL measurements. With a perfectly coupled system, the QY of the cluster can be increased to 200%.

### **8.1.2 Molecular design for NIR TLSCs**

Modified cyanine dyes which exhibit efficient fluorescence with Stokes shifts of ~100 nm have been reported.<sup>[135]</sup> These molecules, which emit from intramolecular charge transfer excited states, absorb in the visible range and thus are not useful in the present application. However, their existence demonstrates that the engineering of cyanines with intramolecular charge transfer states may allow us to achieve NIR emitters with large Stokes shifts through substitutions in the central methine group with bridgehead amine groups (that could be applied to the molecules here). Another strategy is suggested by the increased Stokes shift of CY compared to HITC. The side chain or the central methine group of CY must be responsible for this increase, given that these are the only differences between the two luminophores. Considering the flexibility of the side chain, we hypothesize that it may interact with the polymethine chain electrostatically, reorienting to stabilize the redistribution of charge upon excitation in the same way that a solvent molecule would respond to excitation of a solvated dye. Increasing the number and/or polarity of these side chains as well as central methine substitution are two rational strategies to engineer visibly-transparent NIR luminophores with larger Stokes shifts, and should be pursued in future work. Alternatively, nucleophilic substitutional attack at targeted Cl positions provides another pathway to break the symmetry of the molecular orbitals and enhance the Stokes shift as shown in Figures 8.2 and 8.3.

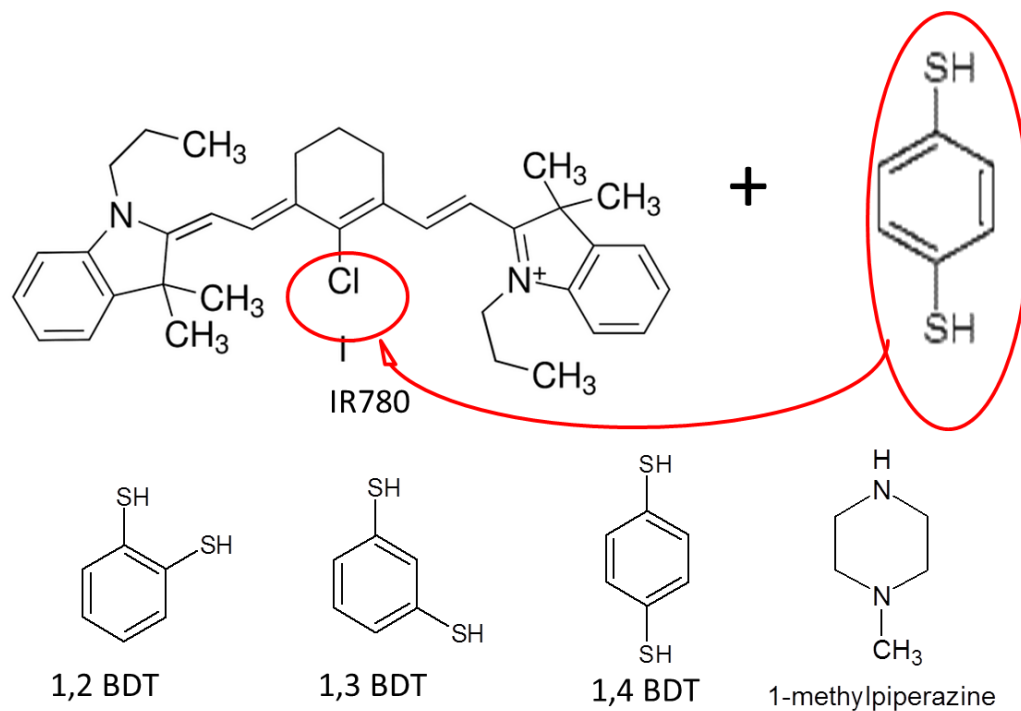


**Figure 8.2** IR 780 in dimethylformamide (DMF) reacted with 1,4 benzenedithiol

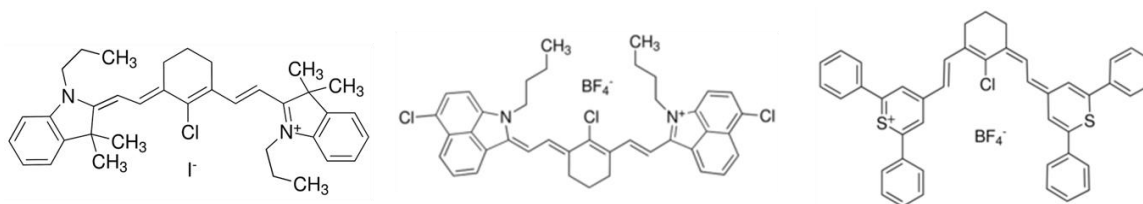


**Figure 8.3** Examples of candidates for molecular design for NIR TLSCs

Additional polymethine derivatives that are candidates for Stokes shift engineering are shown in Figure 8.3. Shown in Figure 8.4 are examples of these new compounds with their corresponding absorption.

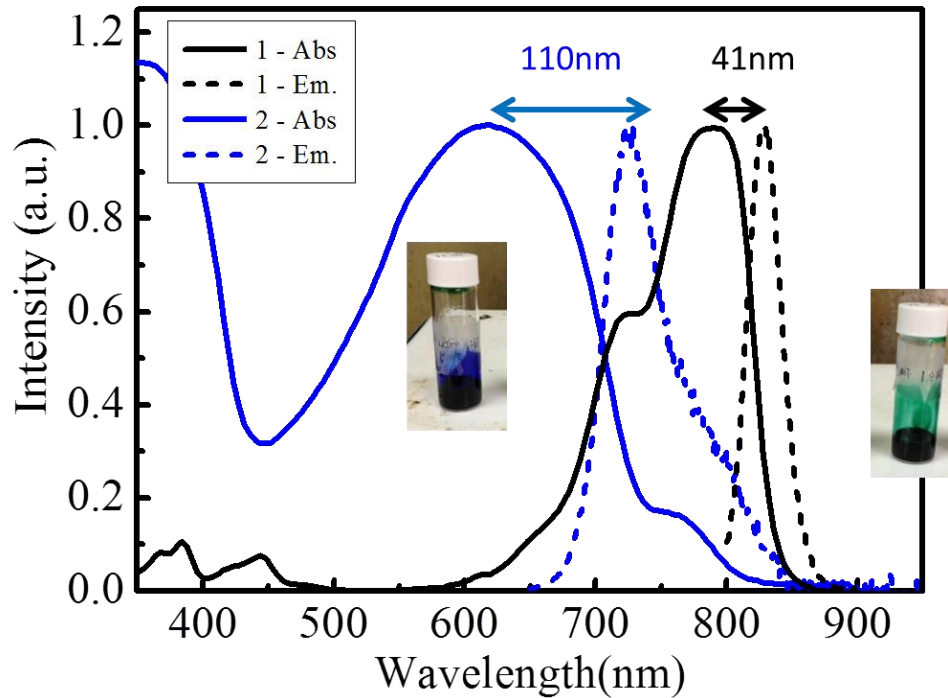


**Figure 8.4** New chemical variants with shifted absorption spectrum and modified Stokes shifts after reaction for 10min.

### 8.1.3 Micro LSC Arrays for NIR TLSCs:

There are two parallel approaches to the segmentation of the inorganic PVs for implantation into waveguides for the NIR-harvesting LSC: i) directly position ultrathin bifacial Si PVs (50-100  $\mu\text{m}$  thick, 1mm wide) that are commercially available, in a vertical orientation within 50  $\mu\text{m}$  slits in a PMMA substrates so that the PV faces are parallel to the edge of the waveguide. The spacing of the segmented PVs is defined by the reabsorption length of the NIR emitter. PV wiring can be explored in combinations of parallel and series connections to maximize output ii) import laser-pattern Si PVs into meshes that are nearly invisible that are then embedded in the plane of the LSC

waveguide. Laser-cut openings can then be encapsulated with the NIR harvester/emitter with the host acting as the waveguide. We have already demonstrated that such patterning is feasible without loss in performance analogous to the demonstration of “sliver” Si PVs. These spatially segmented PVs act to create “micro” LSCs for low-Stokes shift emitters that can eliminate reabsorption losses. Simultaneously these components add photocurrent from solar harvesting proportional to the absorption fraction  $(1 - \langle T \rangle)$ , where segmented PVs create neutral filtering tuned for overall transmission requirements (typically 80-85%).

#### **8.1.4 Transparent mirror design for photon management in TLSCs**

It has already been shown that incorporation of visibly transparent, selective NIR reflectors (based on distributed Bragg reflector designs) in transparent photovoltaics can substantially improve power conversion efficiencies by 50-100%. Similarly we see in our simulations that the incorporation of these coatings can improve the optical efficiency at low plate dimension by  $> 20\%$  while reducing the quantity of dye needed by half for a given optical density.

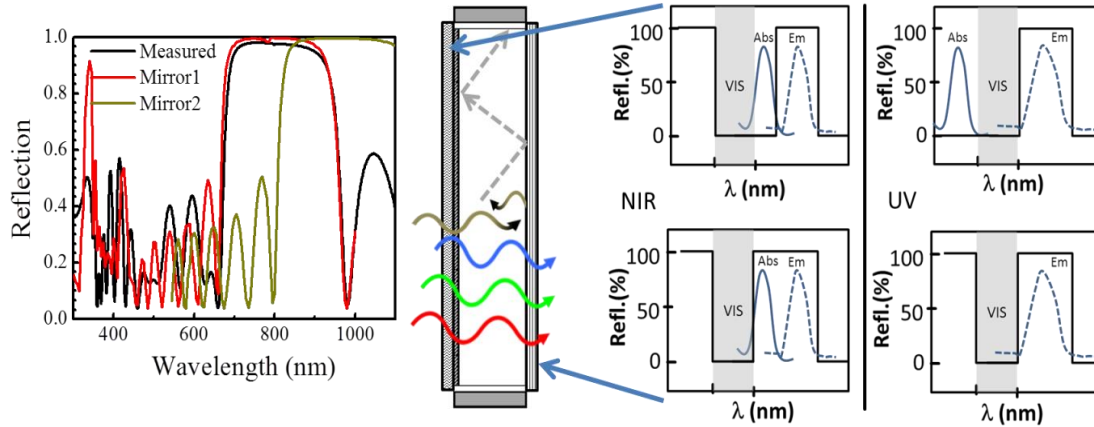


**Figure 8.5** (left) Measured and simulated reflection curves for two *transparent mirrors* designed to accept short-wave NIR and trap longer-wave NIR emission (shown schematically, middle). (right) Schematic for the ideal mirror configuration for the NIR and UV LSCs used to eliminate waveguiding losses.

For LSC sizes  $> 0.5\text{m}^2$  these mirrors are likely to be helpful in mitigating any surface and bulk scattering imperfections that could reduce system efficiencies. Moreover, these coating layers are very similar to low-e-coatings that are already ubiquitously deployed and can complement or replace nearly all of their functionality for heat rejection and optical insulation. Figure 8.5 shows the mirror design for the UV-only and NIR-only LSCs. For complete optimization these architectures can be simulated as a function of emission angle for simultaneously maximized performance and aesthetics.

## APPENDIX

## A1 Quantum yield for solutions and films

**Table A1** Quantum yield and absorption of organic luminescent materials in solutions

Compound	Solvent	Concentration (mg/ml)	Quantum Yield (%)	Absorption (%)
IR 140	Methanol	0,1	2.5	72
		0.01	6.1	11
	Ethanol		0.6	100
			3.3	65
			5.4	20
IR 140	DCM	0.01	3.5	100
		0.001	3.5	63
IR 140	Acetonitrile	0.01	1.8	100
		0.001	8.5	92
IR 144	Methanol	0.1	4.1	20
	Ethanol		1.8	90
			3.7	30
IR 144	DCM	0.01	1.3	100
		0.001	1.8	51
	Acetonitrile		4.5	70
			4	15
IR 780	Methanol	0.1	2.9	73
		0.01	5.5	11
IR 780	DCM	0.01	1.9	100
		0.005	2.5	100
		0.0025	3.5	99
		0.001	5.8	99
		0.0005	8.8	89
		0.00025	12	66
		0.0001	15.2	28
		0.00005	26.7	15
0.000025	31.6	10		
IR792	Acetonitrile	0.01	0.3	100
		0.001	2	72
		0.0001	3.5	7
	DCM	0.01	0.4	100

**Table A1 (cont'd)**

		0.001	1.7	96
		0.0001	6	27
IR820	Methanol	0.01	0	100
		0.001	0	85
		0.0001	0	30
	DCM	0.01	0	100
		0.001	0	45
		0.0001	0	8
ObPc	DCM	0.1	1.7	92
	DCM	0.01	3.2	23
	DCM	0.001	3.1	3
ObPc	TOL	0.1	3.2	94
	TOL	0.01	9.3	27
	TOL	0.01	11.4	3
ObPc	Chloroform	0.1	3.2	95
	Chloroform	0.01	6.3	27
	Chloroform	0.001	8.6	4
ZnNc	Toluene	0.01	1.8	100
		0.005	3.9	95
		0.0025	5.5	80
		1.00E-03	7.9	47
		5.00E-04	9.7	28
		2.50E-04	10.6	17
		1.00E-04	10.2	10
		5.00E-05	15	5
		2.50E-05	10	3
	Chlorobenzene	0.01	3.6	
		0.005	4.3	
		0.0025	5.9	
		1.00E-03	8.4	
		5.00E-04	15	
		2.50E-04	7	
		1.00E-04	3.06	

**Table A2** Quantum yield and absorption for luminescent materials in films

Compound	Solvent	Polymer	Concentration (mg/mL)	Layers	Quantum Yield (%)	Absorption (%)	
DTCP	Acetonitrile		0.02	1	3.5	30	
				2	5.4	18	
DTCI	DCM		0.02	1	6	35	
	Acetonitrile		0.02	1	24	5	
HITCI	DCM		0.02	1	10.5	28	
				0.01	1	17.8	15
				0.005	1	20	10
HITCP	Acetonitrile	Eukitt	0.002	1	27.9	5	
				2	25.2	15	
				3	21	14	
				0.01	1	22.8	15
				2	18.6	40	
				3	21.6	43	
				0.02	1	17.4	40
2	14.2	52					
HITCP	DCM		0.1	1	23.7	44	
				2	14	80	
				0.05	1	38.6	36
				2	21	46	
				0.03	1	49	28
2	21	45					
IR780	DCM		0.1	1	5.75	30	
				2	5.8		
				0.01	1	1.7	5

## BIBLIOGRAPHY

## BIBLIOGRAPHY

- [1] S. R. Forrest, *Nature* **2004**, 428, 911.
- [2] M. C. Barr, R. M. Howden, R. R. Lunt, V. Bulovic, K. K. Gleason, *Advanced Energy Materials* **2012**, 2, 1404.
- [3] M. Kaltenbrunner, M. S. White, E. D. Glowacki, T. Sekitani, T. Someya, N. S. Sariciftci, S. Bauer, *Nature Communications* **2012**, 3.
- [4] Y. S. Park, K. H. Choi, H. K. Kim, *Journal of Physics D-Applied Physics* **2009**, 42.
- [5] M. A. Green, K. Emery, Y. Hishikawa, W. Warta, E. D. Dunlop, *Progress in Photovoltaics* **2014**, 22, 701.
- [6] C. W. Tang, *Applied Physics Letters* 1986, 48, 183.
- [7] F. Vollmer, W. Rettig, *Journal of Photochemistry and Photobiology a-Chemistry* 1996, 95, 143.
- [8] I. Baumberg, O. Berezin, A. Drabkin, B. Gorelik, L. Kogan, M. Voskobojnik, M. Zaidman, *Polymer Degradation and Stability* 2001, 73, 403.
- [9] R. Kinderman, L. H. Slooff, A. R. Burgers, N. J. Bakker, A. Buchtemann, R. Danz, J. A. M. van Roosmalen, *Journal of Solar Energy Engineering-Transactions of the Asme* 2007, 129, 277.
- [10] L. R. Wilson, B. S. Richards, *Applied Optics* 2009, 48, 212.
- [11] J. S. Batchelder, A. H. Zewail, T. Cole, *Applied Optics* 1981, 20, 3733.
- [12] M. J. Currie, J. K. Mapel, T. D. Heidel, S. Goffri, M. A. Baldo, *Science* 2008, 321, 226.

- [13] J. M. Drake, M. L. Lesiecki, J. Sansregret, W. R. L. Thomas, *Applied Optics* 1982, 21, 2945.
- [14] J. Yoon, L. F. Li, A. V. Semichaevsky, J. H. Ryu, H. T. Johnson, R. G. Nuzzo, J. A. Rogers, *Nature Communications* 2011, 2, 343.
- [15] W. G. J. H. M. van Sark, K. W. J. Barnham, L. H. Slooff, A. J. Chatten, A. Buchtemann, A. Meyer, S. J. McCormack, R. Koole, D. J. Farrell, R. Bose, E. E. Bende, A. R. Burgers, T. Budel, J. Quilitz, M. Kennedy, T. Meyer, C. D. M. Donega, A. Meijerink, D. Vanmaekelbergh, *Opt Express* 2008, 16, 21773.
- [16] A. M. Hermann, *Solar Energy* 1982, 29, 323.
- [17] L. H. Slooff, R. Kinderman, A. R. Burgers, A. Buechtemann, R. Danz, T. B. Meyer, A. J. Chatten, D. Farrell, K. W. J. Barnham, J. A. M. van Roosmalen, *Photonics for Solar Energy Systems* 2006, 6197.
- [18] M. G. Debije, P. P. C. Verbunt, P. J. Nadkarni, S. Velate, K. Bhaumik, S. Nedumbamana, B. C. Rowan, B. S. Richards, T. L. Hoeks, *Applied Optics* 2011, 50, 163.
- [19] R. Reisfeld, M. Eyal, V. Chernyak, R. Zusman, *Solar Energy Materials* 1988, 17, 439.
- [20] A. F. Mansour, H. M. A. Killa, S. A. El-Wanees, M. Y. El-Sayed, *Polymer Testing* 2005, 24, 519.
- [21] W. E. Benjamin, D. R. Veit, M. J. Perkins, E. Bain, K. Scharnhorst, S. McDowall, D. L. Patrick, J. D. Gilbertson, *Chemistry of Materials* 2014, 26, 1291.
- [22] M. A. ElShahawy, A. F. Mansour, *Journal of Materials Science-Materials in Electronics* 1996, 7, 171.
- [23] R. F. Kubin, A. N. Fletcher, *Journal of Luminescence* 1982, 27, 455.
- [24] A. F. Mansour, *Polymer Testing* 1998, 17, 333.
- [25] A. Sanguineti, M. Sassi, R. Turrisi, R. Ruffo, G. Vaccaro, F. Meinardi, L. Beverina, *Chemical Communications* 2013, 49, 1618.

- [26] C. Botta, P. Betti, M. Pasini, *Journal of Materials Chemistry A* 2013, 1, 510.
- [27] A. P. Green, K. T. Butler, A. R. Buckley, *Applied Physics Letters* 2013, 102.
- [28] Y. Kawamura, H. Sasabe, C. Adachi, *Japanese Journal of Applied Physics Part 1- Regular Papers Short Notes & Review Papers* 2004, 43, 7729.
- [29] G. Weber, F. W. J. Teale, *Transactions of the Faraday Society* 1957, 53, 646.
- [30] W. Holzer, A. Penzkofer, T. Tsuboi, *Chemical Physics* 2005, 308, 93.
- [31] O. I. Micic, C. J. Curtis, K. M. Jones, J. R. Sprague, A. J. Nozik, *Journal of Physical Chemistry* 1994, 98, 4966.
- [32] D. J. Norris, M. G. Bawendi, *Physical Review B* 1996, 53, 16338.
- [33] A. J. Chatten, K. W. J. Barnham, B. F. Buxton, N. J. Ekins-Daukes, M. A. Malik, *Solar Energy Materials and Solar Cells* 2003, 75, 363.
- [34] S. J. Gallagher, B. Norton, P. C. Eames, *Solar Energy* 2007, 81, 813.
- [35] X. Y. Wang, J. Y. Zhang, A. Nazzal, M. Xiao, *Applied Physics Letters* 2003, 83, 162.
- [36] S. M. Reda, *Acta Materialia* 2008, 56, 259.
- [37] A. Schuler, M. Python, M. V. del Olmo, E. de Chambrier, *Solar Energy* 2007, 81, 1159.
- [38] I. Coropceanu, M. G. Bawendi, *Nano Letters* 2014, 14, 4097.
- [39] C. S. Erickson, L. R. Bradshaw, S. McDowall, J. D. Gilbertson, D. R. Gamelin, D. L. Patrick, *Acs Nano* 2014, 8, 3461.

- [40] Z. Krumer, S. J. Pera, R. J. A. van Dijk-Moes, Y. M. Zhao, A. F. P. de Brouwer, E. Groeneveld, W. G. J. H. M. van Sark, R. E. I. Schropp, C. D. Donega, *Solar Energy Materials and Solar Cells* 2013, 111, 57.
- [41] G. V. Shcherbatyuk, R. H. Inman, C. Wang, R. Winston, S. Ghosh, *Applied Physics Letters* 2010, 96.
- [42] S. Kim, B. Fisher, H. J. Eisler, M. Bawendi, *Journal of the American Chemical Society* 2003, 125, 11466.
- [43] R. G. Xie, X. H. Zhong, T. Basche, *Advanced Materials* 2005, 17, 2741.
- [44] P. T. K. Chin, C. D. M. Donega, S. S. Bavel, S. C. J. Meskers, N. A. J. M. Sommerdijk, R. A. J. Janssen, *Journal of the American Chemical Society* 2007, 129, 14880.
- [45] Y. P. Du, B. Xu, T. Fu, M. Cai, F. Li, Y. Zhang, Q. B. Wang, *Journal of the American Chemical Society* 2010, 132, 1470.
- [46] K. E. Knowles, T. B. Kilburn, D. G. Alzate, S. McDowall, D. R. Gamelin, *Chemical Communications* 2015, 51, 9129.
- [47] L. R. Bradshaw, K. E. Knowles, S. McDowall, D. R. Gamelin, *Nano Letters* 2015, 15, 1315.
- [48] J. A. Levitt, W. H. Weber, *Applied Optics* 1977, 16, 2684.
- [49] R. Reisfeld, Y. Kalisky, *Chemical Physics Letters* 1981, 80, 178.
- [50] T. Jin, S. Inoue, K. Machida, G. Adachi, *Journal of the Electrochemical Society* 1997, 144, 4054.
- [51] T. Jin, S. Inoue, S. Tsutsumi, K. Machida, G. Adachi, *Chemistry Letters* 1997, 171.
- [52] L. N. Sun, J. B. Yu, H. J. Zhang, Q. G. Meng, E. Ma, C. Y. Peng, K. Y. Yang, *Microporous and Mesoporous Materials* 2007, 98, 156.

- [53] K. A. White, D. A. Chengelis, K. A. Gogick, J. Stehman, N. L. Rosi, S. Petoud, *Journal of the American Chemical Society* 2009, 131, 18069.
- [54] J. Zhang, P. D. Badger, S. J. Geib, S. Petoud, *Angewandte Chemie-International Edition* 2005, 44, 2508.
- [55] A. Sanguineti, A. Monguzzi, G. Vaccaro, F. Meinardi, E. Ronchi, M. Moret, U. Cosentino, G. Moro, R. Simonutti, M. Mauri, R. Tubino, L. Beverina, *Physical Chemistry Chemical Physics* 2012, 14, 6452.
- [56] H. Bengtson, 2011.
- [57] L. H. Slooff, E. E. Bende, A. R. Burgers, T. Budel, M. Pravettoni, R. P. Kenny, E. D. Dunlop, A. Buchtemann, *Physica Status Solidi-Rapid Research Letters* 2008, 2, 257.
- [58] F. Galluzzi, E. Scafe, *Solar Energy* 1984, 33, 501.
- [59] W. H. Weber, J. Lambe, *Applied Optics* 1976, 15, 2299.
- [60] A. Goetzberger, W. Greubel, *Applied Physics* 1977, 14, 123.
- [61] V. Wittwer, W. Stahl, A. Goetzberger, *Solar Energy Materials* 1984, 11, 187.
- [62] G. Smestad, H. Ries, R. Winston, E. Yablonovitch, *Solar Energy Materials* 1990, 21, 99.
- [63] J. C. Goldschmidt, M. Peters, A. Bosch, H. Helmers, F. Dimroth, S. W. Glunz, G. Willeke, *Solar Energy Materials and Solar Cells* 2009, 93, 176.
- [64] M. A. Faist, T. Kirchartz, W. Gong, R. S. Ashraf, I. McCulloch, J. C. de Mello, N. J. Ekins-Daukes, D. D. C. Bradley, J. Nelson, *Journal of the American Chemical Society* 2012, 134, 685.
- [65] J. Bomm, A. Buchtemann, A. J. Chatten, R. Bose, D. J. Farrell, N. L. A. Chan, Y. Xiao, L. H. Slooff, T. Meyer, A. Meyer, W. G. J. H. M. van Sark, R. Koole, *Solar Energy Materials and Solar Cells* 2011, 95, 2087.

- [66] G. Smestad, C. Bignozzi, R. Argazzi, *Solar Energy Materials and Solar Cells* 1994, 33, 253.
- [67] L. Desmet, A. J. M. Ras, D. K. G. de Boer, M. G. Debije, *Optics Letters* 2012, 37, 3087.
- [68] T. X. Wang, J. Zhang, W. Ma, Y. H. Luo, L. J. Wang, Z. J. Hu, W. X. Wu, X. Wang, G. Zou, Q. J. Zhang, *Solar Energy* 2011, 85, 2571.
- [69] M. G. Debije, P. P. C. Verbunt, *Advanced Energy Materials* 2012, 2, 12.
- [70] Wikipedia.
- [71] L. R. Wilson, Ph.D. Thesis, Heriot-Watt University, May 2010.
- [72] Y. Zhao, R. R. Lunt, *Advanced Energy Materials* 2013, 3, 1143.
- [73] S. T. Bailey, G. E. Lokey, M. S. Hanes, J. D. M. Shearer, J. B. McLafferty, G. T. Beaumont, T. T. Baseler, J. M. Layhue, D. R. Broussard, Y. Z. Zhang, B. P. Wittmershaus, *Solar Energy Materials and Solar Cells* 2007, 91, 67.
- [74] R. W. Olson, R. F. Loring, M. D. Fayer, *Applied Optics* 1981, 20, 2934.
- [75] N. C. Giebink, G. P. Wiederrecht, M. R. Wasielewski, *Nature Photonics* 2011, 5, 695.
- [76] A. L. Bhatnagar, W, *Fundamentals of solar astronomy*, 2005.
- [77] D. H. W. Li, J. C. Lam, C. C. S. Lau, T. W. Huan, *Renewable Energy* 2004, 29, 921.
- [78] A. Kerrouche, D. A. Hardy, D. Ross, B. S. Richards, *Solar Energy Materials and Solar Cells* 2014, 122, 99.
- [79] S. W. Leow, C. Corrado, M. Osborn, S. A. Carter, *High and Low Concentrator Systems for Solar Electric Applications Viii* 2013, 8821.

- [80] J. W. E. Wiegman, E. van der Kolk, *Solar Energy Materials and Solar Cells* 2012, 103, 41.
- [81] G. Kocher-Oberlehner, M. Bardosova, M. Pemble, B. S. Richards, *Solar Energy Materials and Solar Cells* 2012, 104, 53.
- [82] F. Meinardi, A. Colombo, K. A. Velizhanin, R. Simonutti, M. Lorenzon, L. Beverina, R. Viswanatha, V. I. Klimov, S. Brovelli, *Nature Photonics* 2014, 8, 392.
- [83] R. R. Lunt, *Applied Physics Letters* 2012, 101, 043902.
- [84] N. Takada, T. Tsutsui, S. Saito, *Applied Physics Letters* 1993, 63, 2032.
- [85] J. Zheng, C. W. Zhang, R. M. Dickson, *Physical Review Letters* 2004, 93.
- [86] M. Reers, T. W. Smith, L. B. Chen, *Biochemistry* 1991, 30, 4480.
- [87] X. H. Zhong, Y. Y. Feng, W. Knoll, M. Y. Han, *Journal of the American Chemical Society* 2003, 125, 13559.
- [88] J. A. Misewich, R. Martel, P. Avouris, J. C. Tsang, S. Heinze, J. Tersoff, *Science* 2003, 300, 783.
- [89] R. R. Lunt, T. P. Osedach, P. R. Brown, J. A. Rowehl, V. Bulovic, *Advanced Materials* 2011, 23, 5712.
- [90] D. G. Goebel, *Applied Optics* 1967, 6, 125.
- [91] J. A. Jacquez, H. F. Kuppenheim, *Journal of the Optical Society of America* 1955, 45, 460.
- [92] K. Suzuki, A. Kobayashi, S. Kaneko, K. Takehira, T. Yoshihara, H. Ishida, Y. Shiina, S. Oishic, S. Tobita, *Physical Chemistry Chemical Physics* 2009, 11, 9850.
- [93] L. Porres, A. Holland, L. O. Palsson, A. P. Monkman, C. Kemp, A. Beeby, *Journal of Fluorescence* 2006, 16, 267.

- [94] R. Rottgers, S. Gehnke, *Applied Optics* 2012, 51, 1336.
- [95] V. Shrotriya, G. Li, Y. Yao, T. Moriarty, K. Emery, Y. Yang, *Advanced Functional Materials* 2006, 16, 2016.
- [96] J. S. Batchelder, A. H. Zewail, T. Cole, *Applied Optics* 1979, 18, 3090.
- [97] W. C. Dorman, R. E. Mccarley, *Inorganic Chemistry* 1974, 13, 491.
- [98] D. J. Osborn, G. L. Baker, R. N. Ghosh, *Journal of Sol-Gel Science and Technology* 2005, 36, 5.
- [99] M. Newsham, *PhD Thesis*, Michigan State University, **1988**.
- [100] J. Kalinowski, *Organic Light-Emitting Diodes: Principles, Characteristics, and Processes.*, CRC Press, 2005.
- [101] J. R. Lakowicz, *Principles of fluorescence spectroscopy*, Springer, 2006.
- [102] R. V. Ziolkowski, K.; Kamat.P.V., *Langmuir* 1997, 13 3124.
- [103] Y. Amao, K. Asai, I. Okura, *Journal of Porphyrins and Phthalocyanines* 2000, 4, 292.
- [104] H. Lin, D. Q. Chen, Y. L. Yu, Z. F. Shan, P. Huang, A. P. Yang, Y. S. Wang, *Journal of Alloys and Compounds* 2011, 509, 3363.
- [105] X. A. Y. Huang, X. A. H. Ji, Q. Y. A. Zhang, *Journal of the American Ceramic Society* 2011, 94, 833.
- [106] C. Strumpel, M. McCann, G. Beaucarne, V. Arkhipov, A. Slaoui, V. Svrcek, C. del Canizo, I. Tobias, *Solar Energy Materials and Solar Cells* 2007, 91, 238.
- [107] B. C. Rowan, B. S. Richards, *Proceedings of the 23rd European Photovoltaic Solar Energy Conference and Exhibition, Valencia, 2008*, 700.

- [108] O. Moudam, B. C. Rowan, M. Alamiry, P. Richardson, B. S. Richards, A. C. Jones, N. Robertson, *Chemical Communications* 2009, 6649.
- [109] M. A. Green, K. Emery, Y. Hishikawa, W. Warta, E. D. Dunlop, *Progress in Photovoltaics* 2012, 20, 12.
- [110] G. Calzaferri, R. Meallet-Renault, D. Bruhwiler, R. Pansu, I. Dolamic, T. Dienel, P. Adler, H. R. Li, A. Kunzmann, *Chemphyschem* 2011, 12, 580.
- [111] N. C. Giebink, G. P. Wiederrecht, M. R. Wasielewski, *Nature Photonics* 2011, 5, 694.
- [112] V. J. Pansare, S. Hejazi, W. J. Faenza, R. K. Prud'homme, *Chemistry of Materials* 2012, 24, 812.
- [113] J. O. Escobedo, O. Rusin, S. Lim, R. M. Strongin, *Current Opinion in Chemical Biology* 2010, 14, 64.
- [114] G. M. Fischer, M. Isomaki-Kron Dahl, I. Gottker-Schnetmann, E. Daltrozzo, A. Zumbusch, *Chemistry-a European Journal* 2009, 15, 4857.
- [115] R. Weissleder, *Nature Biotechnology* 2001, 19, 316.
- [116] J. C. Ostrowski, K. Susumu, M. R. Robinson, M. J. Therien, G. C. Bazan, *Advanced Materials* 2003, 15, 1296.
- [117] K. Barnham, J. L. Marques, J. Hassard, P. O'Brien, *Applied Physics Letters* 2000, 76, 1197.
- [118] M. H. V. Werts, J. W. Hofstraat, F. A. J. Geurts, J. W. Verhoeven, *Chemical Physics Letters* 1997, 276, 196.
- [119] V. Sholin, J. D. Olson, S. A. Carter, *Journal of Applied Physics* 2007, 101.
- [120] M. W. Schmidt, K. K. Baldrige, J. A. Boatz, S. T. Elbert, M. S. Gordon, J. H. Jensen, S. Koseki, N. Matsunaga, K. A. Nguyen, S. J. Su, T. L. Windus, M. Dupuis, J. A. Montgomery, *Journal of Computational Chemistry* 1993, 14, 1347.

[121] M. S. Gordon, M. W. Schmidt, in *Theory and Applications of Computational Chemistry: the First Forty Years*, (Eds: C. E. Dykstra, G. Frenking, K. S. Kim, G. E. Scuseria), Elsevier, Amsterdam 2005, 1167.

[122] Y. Shao, L. F. Molnar, Y. Jung, J. Kussmann, C. Ochsenfeld, S. T. Brown, A. T. B. Gilbert, L. V. Slipchenko, S. V. Levchenko, D. P. O'Neill, R. A. DiStasio, R. C. Lochan, T. Wang, G. J. O. Beran, N. A. Besley, J. M. Herbert, C. Y. Lin, T. Van Voorhis, S. H. Chien, A. Sodt, R. P. Steele, V. A. Rassolov, P. E. Maslen, P. P. Korambath, R. D. Adamson, B. Austin, J. Baker, E. F. C. Byrd, H. Dachsel, R. J. Doerksen, A. Dreuw, B. D. Dunietz, A. D. Dutoi, T. R. Furlani, S. R. Gwaltney, A. Heyden, S. Hirata, C. P. Hsu, G. Kedziora, R. Z. Khalliulin, P. Klunzinger, A. M. Lee, M. S. Lee, W. Liang, I. Lotan, N. Nair, B. Peters, E. I. Proynov, P. A. Pieniazek, Y. M. Rhee, J. Ritchie, E. Rosta, C. D. Sherrill, A. C. Simmonett, J. E. Subotnik, H. L. Woodcock, W. Zhang, A. T. Bell, A. K. Chakraborty, D. M. Chipman, F. J. Keil, A. Warshel, W. J. Hehre, H. F. Schaefer, J. Kong, A. I. Krylov, P. M. W. Gill, M. Head-Gordon, *Physical Chemistry Chemical Physics* 2006, 8, 3172.

[123] P. Piecuch, S. A. Kucharski, K. Kowalski, M. Musial, *Computer Physics Communications* 2002, 149, 71.

[124] K. Kowalski, P. Piecuch, *Journal of Chemical Physics* 2004, 120, 1715.

[125] M. Wloch, J. R. Gour, K. Kowalski, P. Piecuch, *Journal of Chemical Physics* 2005, 122.

[126] T. Yanai, D. P. Tew, N. C. Handy, *Chemical Physics Letters* 2004, 393, 51.

[127] J. F. Stanton, R. J. Bartlett, *Journal of Chemical Physics* 1993, 98, 7029.

[128] T. H. Dunning, *Journal of Chemical Physics* 1989, 90, 1007.

[129] W. Kohn, L. J. Sham, *Physical Review* 1965, 140, 1133.

[130] R. L. Martin, *Journal of Chemical Physics* 2003, 118, 4775.

[131] E. K. U. Gross, W. Kohn, *Physical Review Letters* 1985, 55, 2850.

[132] M. E. Casida, C. Jamorski, K. C. Casida, D. R. Salahub, *Journal of Chemical Physics* 1998, 108, 4439.

[133] S. Hirata, M. Head-Gordon, *Chemical Physics Letters* 1999, 314, 291.

[134] D. Jacquemin, E. A. Perpete, G. Scalmani, M. J. Frisch, R. Kobayashi, C. Adamo, *Journal of Chemical Physics* 2007, 126.

[135] X. J. Peng, F. L. Song, E. Lu, Y. N. Wang, W. Zhou, J. L. Fan, Y. L. Gao, *Journal of the American Chemical Society* 2005, 127, 4170.

[136] C. A. Berolino, G. Caputo, C. Barolo, G. Viscardi, S. Coluccia, *J. Fluoresc.* 2006, 16, 221.

[137] X. Sheng, L. Shen, T. Kim, L. F. Li, X. R. Wang, R. Dowdy, P. Froeter, K. Shigeta, X. L. Li, R. G. Nuzzo, N. C. Giebink, J. A. Rogers, *Advanced Energy Materials* 2013, 3, 991.

[138] J. Kalowekamo, E. Baker, *Solar Energy* **2009**, 83, 1224.

|